Targeting Epsins by nanotherapy regulates lipid metabolism and promotes ABCG1-mediated cholesterol efflux to fortify atheroma regression

Kui Cui[1]†, Xinlei Gao[2]†, Beibei Wang[1]†, Hao Wu[1], Yunzhou Dong[1], Yuling Xiao[3], Xingya Jiang[3], Marina V. Malovichko[4], Kathryn Li[1], Dan Shan[1], Qianman Peng[1], Yaowei Lu[1], Bo Zhu[1], Rongbin Zheng[2], Scott Wong[1], Douglas B. Cowan[1], MacRae Linton[5], Sanjay Srivastava[4], Jinjun Shi[3], Kaifu Chen[2*], Hong Chen[1*]

1. Vascular Biology Program, Boston Children's Hospital and Department of Surgery, Harvard Medical School; Boston, MA, 02115, USA.
2. Department of Cardiology, Boston Children's Hospital, Harvard Medical School; Boston, MA, 02115, USA.
3. Center for Nanomedicine and Department of Anesthesiology, Brigham and Women's Hospital, Harvard Medical School; Boston, MA, 02115, USA.
4. Division of Environmental Medicine, University of Louisville; Louisville, KY, 40292, USA.
5. Atherosclerosis Research Unit, Cardiovascular Medicine, Department of Medicine, Vanderbilt University Medical Center; Nashville, TN, 37232, USA.

Short title: Epsins regulate lipid metabolism and transport

†These authors contributed equally to this work.

*Corresponding authors. Email: hong.chen@childrens.harvard.edu

kaifu.chen@childrens.harvard.edu

25 **Nonstandard Abbreviations and Acronyms**

26

AAV8	adeno-associated virus-8
ABCG1	ATP Binding Cassette Subfamily G Member 1
ACAT	acyl-CoA cholesterol acyltransferase
AMI	acute myocardial infarction
BCA	brachiocephalic artery
CAD	coronary artery disease
CEC	cholesterol efflux capacity
DKO	double knockout
ENTH	epsin N-terminal homology
GEM	gel beads-in-emulsion
GO	gene ontology
GSEA	gene set enrichment analysis
HDL	high density lipoprotein
ICAM-1	intercellular adhesion molecule-1
IF	immunofluorescence staining
IP	immunoprecipitation
LXR	liver X receptor
M-CSF	macrophage colony stimulating factor
NP	nanoparticle
ORO	oil red O
oxLDL	oxidized low-density lipoprotein
PCSK9	proprotein convertase subtilisin/kexin type 9 serine protease
RCT	reverse cholesterol transport
scRNA-seq	single-cell RNA sequencing
siRNA	small interfering RNA
SR-A	scavenger receptor-A
S2PNP-siEpsin1/2	S2P-conjugated Epsins 1 and 2 siRNA nanoparticle
S2PNP-siCtrl	S2P-conjugated Control nanoparticle
TG	thioglycolate
UIM	ubiquitin-interacting motif
VCAM-1	vascular cell adhesion molecule-1
VSMCs	vascular smooth muscle cells
WB	western blot
WD	western diet

27

ABSTRACT

BACKGROUND: Excess cholesterol accumulation in lesional macrophages elicits complex responses in atherosclerosis. Epsins, a family of endocytic adaptors, fuel the progression of atherosclerosis; however, the underlying mechanism and therapeutic potential of targeting Epsins remains unknown. In this study, we determined the role of Epsins in macrophage-mediated metabolic regulation. We then developed an innovative method to therapeutically-target macrophage Epsins with specially-designed S2P-conjugated lipid nanoparticles (NPs), which encapsulate small interfering RNAs to suppress Epsins.

METHODS: We used single cell RNA sequencing (scRNA-seq) with our newly developed algorithm MEBOCOST to study cell-cell communications mediated by metabolites from sender cells and sensor proteins on receiver cells. Biomedical, cellular and molecular approaches were utilized to investigate the role of macrophage Epsins in regulating lipid metabolism and transport. We performed this study using myeloid-specific Epsin double knockout (LysM-DKO) mice and mice with a genetic reduction of ABCG1 (LysM-DKO-ABCG1$^{fl/+}$). The NPs targeting lesional macrophages were developed to encapsulate interfering RNAs to treat atherosclerosis.

RESULTS: We revealed that Epsins regulate lipid metabolism and transport in atherosclerotic macrophages. Inhibiting Epsins by nanotherapy halts inflammation and accelerates atheroma resolution. Harnessing lesional macrophage-specific NP delivery of Epsin siRNAs, we showed that silencing of macrophage Epsins markedly diminished atherosclerotic plaque size and promoted plaque regression. Mechanistically, we demonstrated that Epsins bound to CD36 to facilitate lipid uptake by enhancing CD36 endocytosis and recycling. Conversely, Epsins promoted ABCG1 degradation via lysosomes and hampered ABCG1-mediated cholesterol efflux and reverse cholesterol transport. In a LysM-DKO-ABCG1$^{fl/+}$ mouse model, enhanced cholesterol efflux and reverse transport due to Epsin deficiency was suppressed by the reduction of ABCG1.

CONCLUSIONS: Our findings suggest that targeting Epsins in lesional macrophages may offer therapeutic benefits for advanced atherosclerosis by reducing CD36-mediated lipid uptake and increasing ABCG1-mediated cholesterol efflux.

Key Words: Epsin, nanoparticle, lipid metabolism, atherosclerosis, CD36, ABCG1

Novelty and Significance

WHAT IS KNOWN?

- Epsin endocytic adaptor proteins are upregulated in human and mouse atherosclerotic lesions
- Lesional macrophages internalize lipids primarily through scavenger receptor-mediated endocytosis such as CD36 and SR-A
- Macrophage-mediated cholesterol efflux and reverse cholesterol transport is crucial to atheroma resolution

WHAT NEW INFORMATION DOES THIS ARTICLE CONTRIBUTE?

- ScRNA-seq combined with the newly-developed algorithm MEBOCOST reveals that Epsins are involved in macrophage-mediated lipid metabolic regulation
- Macrophage epsins promote lipid uptake by targeting CD36 endocytosis and membrane recycling via the Epsin ENTH domain
- Epsins bind ubiquitinated ABCG1—resulting in the endocytosis and lysosomal degradation of this cholesterol transporter, which reduces cholesterol efflux.
- Macrophage-specific, nanoparticle-mediated RNAi delivery exhibits a therapeutic benefit for the treatment of atherosclerosis
- Atherosclerotic plaque regression using this nanoparticle delivery platform represents a clinically-relevant approach for the treatment of advance atherosclerosis

BRIEF SUMMARY

Despite the development of new cholesterol-lowering therapies, including the recently approved PCSK9 small interfering RNA (siRNA) antagonists, patients still face a tremendous risk of developing major acute cardiovascular events resulting from chronic inflammation in the plaque. We employed a novel nanomedicine platform containing a stabilin-2 targeting peptide (S2P) to

83 deliver Epsin-specific siRNAs to lesional macrophages. We discovered that inhibition of these
84 adaptor proteins in lesional macrophages significantly diminished plaque size and necrotic core
85 area, increased fibrous cap thickness, and promoted plaque regression.

86

87 **INTRODUCTION**

88 Atherosclerosis is a complex and chronic condition that results in a buildup of arterial fatty
89 deposits, called plaques that are the root cause of coronary heart disease, ischemic stroke, and
90 peripheral artery disease [1,2]. Despite effective lipid-lowering therapies including new drugs of
91 antibody and siRNA drugs targeting PCSK9, atherosclerosis is still the leading cause of mortality
92 worldwide. Atherosclerotic lesion formation involves interactions between oxidized low-density
93 lipoprotein (oxLDL) and prominent constituents of the arterial wall including monocyte-derived
94 macrophages, immune cells and vascular smooth muscle cells [3,4]. Mounting evidence indicates that
95 factors with the potential to promote macrophage egress from plaques (*e.g.,* regulatory T cells)
96 play a critical role in regulating macrophage pro-resolving functions during atherosclerosis
97 regression [5]. Furthermore, the pro-inflammatory effects of oxLDL lead to endothelial activation
98 and macrophage recruitment [6]. Invading macrophages in the sub-endothelium ingest modified
99 LDL and are transformed into lipid-laden foam cells [1,3]. This escalates arterial inflammation—a
100 prime contributor to the transition from a stable to vulnerable atheroma [7-10]. Accordingly, patients
101 that receive a therapeutic cocktail aimed at alleviating dyslipidemia and hypertension still develop
102 deleterious cardiovascular diseases [2,11]. This accentuates the urgent need for next-generation
103 therapies geared toward eradicating inflammation in the arterial wall.

104 Epsins are a family of highly-conserved endocytic adaptor proteins that associate with the
105 plasma membrane through interactions between their N-terminal homology (ENTH) domain and

106 membrane PI (4,5) P2 [12-14], where it recognizes and recruits ubiquitinated cell surface receptors to
107 clathrin-coated pits for internalization via its ubiquitin-interacting motif (UIM) and clathrin/AP-2
108 binding sites, respectively [15-18]. Epsins 1 and 2 are ubiquitously expressed, redundant in function,
109 and essential for embryonic survival [19]. The embryonic lethality of Epsin 1 and 2 double knockout
110 mice (DKO) prompted us to generate conditional Epsin1$^{fl/fl}$; Epsin2$^{-/-}$ mice. Combining DKO
111 strains with specific Cre deleter mouse strains creates tissue and cell type-specific DKO mice [19,20].
112 Despite their multifaceted functions, our previous work demonstrates that Epsins possess a vast
113 degree of specificity and selectivity in choosing their binding partners. Therefore, the actions of
114 Epsins are cell context-dependent [19-26]. Notably, we demonstrate that myeloid-specific Epsin loss
115 downregulates inflammation and impedes atheroma formation in an atherogenic mouse model by
116 stabilizing macrophage LRP-1 [26]. However, this model failed to address the role of epsins in
117 hindering atheroma regression and promoting plaque rapture and consequent debilitating episodes.

118 Lesional macrophages internalize lipids primarily through scavenger receptor-mediated
119 endocytosis [27], which is also responsible for foam cell formation [28-32]. Mice lacking both Scavenger
120 Receptor-A (SR-A) and CD36 revealed that CD36 is the major oxLDL receptor required for foam
121 cell formation [29-32]. Our previous studies revealed that Epsins 1 and 2 are upregulated in lesional
122 macrophages [26]. Epsin-deficient (DKO) macrophages exhibited a striking reduction in foam cell
123 formation [26]. As robust lipid uptake by macrophages is one of major responsible factors that drive
124 foam cell formation, we posit a central role for Epsins in regulating lipid uptake in macrophages;
125 however, how Epsins facilitate lipid uptake and whether this occurs through scavenger receptor-
126 mediated uptake of modified LDL during foam cell formation remains unknown.

127 Reverse cholesterol transport (RCT) is responsible for removing excess cholesterol from
128 peripheral tissues to the liver, where it is reused or removed from the body [33]. A critical part of

129 RCT is cholesterol efflux, where accumulated cholesterol removed from macrophages in the
130 subintima is mediated by ATP-binding membrane cassette transporters (ABCA1 and ABCG1)
131 and other molecules [34-36]. Among the regulators of RCT, ABCG1 plays a prominent role in
132 macrophage cholesterol and phospholipid transport to maintain cellular lipid homeostasis by
133 using high density lipoprotein (HDL) as a cholesterol acceptor [37]. HDL is thought to facilitate
134 macrophage re-programming to be less inflammatory through an ATF-3-dependent pathway [38].
135 Several clinical trials and more recent work suggest that increased HDL-cholesterol
136 concentrations fail to improve cardiovascular disease outcomes [39-41]; yet, new data indicate that
137 rather than the steady-state HDL-cholesterol (HDL-C) levels [42], the ability of HDL particles to
138 transport cholesterol from atherosclerotic plaques to the liver is more important [43,44].
139 Consequently, a shift in focus from increasing HDL-cholesterol concentrations to raising RCT
140 function by increasing cholesterol efflux capacity (CEC), the HDL-ABCG1-mediated cholesterol
141 efflux from macrophages, has become a prospective therapy for coronary artery disease (CAD),
142 especially in severe acute myocardial infarction (AMI) patients [45-48]. As lack of effective
143 cholesterol efflux in macrophages hinders the reversal of foam cells to healthy macrophages, we
144 envisioned a major role for macrophage Epsins in regulating cholesterol efflux. Given the
145 importance of cholesterol efflux and RCT in atheroma resolution and the aforementioned risk
146 reduction in AMI patients [34-36], it is crucial to determine whether Epsins inhibit cholesterol efflux
147 and RCT to promote atherosclerotic plaque progression and impede its regression.

148 In this study, we harnessed innovative single-cell bioinformatics technology and therapeutic
149 nanotechnology to better understand atherosclerosis. This allowed us to determine the detrimental
150 role of epsins in prohibiting atheroma regression and promoting plaque rupture using a preclinical
151 atherosclerosis regression model. Mechanistically, we utilized scRNA-seq analysis of

152 macrophages and newly-developed bioinformatic techniques to identify new targets involved in
153 lipid metabolism during atherosclerosis. Based on these new targets, we generated a myeloid-
154 specific-deficient ABCG1 murine model to uncover how epsins regulate lipid metabolism to
155 propel atherosclerosis. Specifically, we show that Epsins facilitate CD36-mediated lipid uptake
156 and inhibit ABCG1-mediated cholesterol efflux, which is an entirely new phenomenon in the field
157 of lipid metabolism. We also employed a novel macrophage-specific nanoparticle delivery system
158 to investigate the therapeutic treatment of atherosclerosis. Lastly, using an early-stage progression
159 model, an advanced-stage progression model, and a regression model of atherosclerosis we
160 established the therapeutic benefit of treating this disease with a nanoparticle delivery system.
161 This rigorous and comprehensive mechanistic study on lipid metabolism, and clinically-relevant
162 nanoparticle-mediated RNAi therapies represents a potential breakthrough for treating this
163 devastating disease.
164

165 **METHODS**

166 Detailed Methods and materials are available in the Supplemental Materials. Antibodies,
167 primers, and reagents are listed in Supplemental Table S1.

168 **Animal models**

169 In this study, all animal procedures were performed in compliance with institutional guidelines
170 and mouse protocols were approved by the Institutional Animal Care and Use Committee (IACUC)
171 of Boston Children's Hospital, MA, USA. Both male and female mice were used. C57BL/6 mice
172 (stock #00664), ApoE$^{-/-}$ mice (stock #008525), LysM-Cre deleter mice (stock #004781), and
173 ABCG1^{flox} mice (C57BL/6-Abcg1^{tm1Ched}/J, stock #027954) were purchased from Jackson Research
174 Laboratory. As double knockout of Epsins 1 and 2 in mice lead to embryonic lethality, we

175 generated Epsin1$^{fl/fl}$;Epsin2$^{-/-}$ mice. These mice were subsequently combined with LysM-Cre
176 deleter mouse strains to create myeloid-specific Epsins deficient (LysM-DKO) mice and bred them
177 to the C57BL/6 background [26]. As proper controls, we also generated wild type C57BL/6 mice
178 bearing LysM Cre. These mice only have one copy of LysM Cre as homozygous LysM Cre mice
179 are susceptible to atherosclerosis. Furthermore, these mice were crossed to the ApoE$^{-/-}$ (C57BL/6)
180 background to obtain ApoE$^{-/-}$/WT and ApoE$^{-/-}$/LysM-DKO mice [26]. We used macrophages from
181 WT and LysM-DKO on either normal background or ApoE$^{-/-}$ background. We have not seen
182 significant differences in the results with these backgrounds. ***For simplicity, we referred to the***
183 ***macrophages from WT or ApoE$^{-/-}$/WT as WT macrophages and macrophage from LysM-DKO***
184 ***and AopE$^{-/-}$/LysM-DKO as DKO macrophages.*** We used these mice (male and female) and
185 primary macrophages (peritoneal and bone marrow derived) isolated from them for this study.

186 In addition, to generate myeloid-specific ABCG1-KO mice, we crossed the LysM-cre^{+} mice
187 with ABCG1$^{fl/fl}$ mice. We then bred the obtained LysM-cre^{+}; ABCG1$^{fl/fl}$ mice with ApoE$^{-/-}$ mice
188 and backcrossed them on to the C57BL/6 background.

189 To induce atherosclerosis, mice were fed Western diet (WD, Protein 17% kcal, Fat 40% kcal,
190 Carbohydrate 43% kcal; D12079B, Research Diets, New Brunswick, USA) starting at the age of
191 6-8 weeks for 8-20 weeks. Mice were sacrificed at different time points based on the experimental
192 design and peritoneal macrophages, blood, heart, aorta and bone marrow monocytes were
193 harvested. For control mice, in addition to ApoE$^{-/-}$;Epsin1$^{+/+}$;Epsin2$^{+/+}$ mice, we also used ApoE^{-}
194 $^{/-}$;Epsin1$^{+/+}$;Epsin2$^{+/+}$ mice with a single copy of LysM-cre, and ApoE$^{-/-}$;Epsin1$^{fl/fl}$;Epsin2$^{-/-}$
195 littermates lacking the single copy of LysM-cre. To simplify the terminology, we refer to these
196 control mice as ApoE$^{-/-}$, as results were not different in any of the analyses we performed. For the
197 study of atheroma resolution, WT mice (both male and female) at the age of 8 weeks were

198 intravenously injected with $2x10^{11}$ genomes of PCSK9 adeno-associated virus (rAAV8-D377Y-
199 mPCSK9 purchased from Boston Children's Hospital Viral Core Facility) followed by 17 weeks
200 of WD feeding. For each experimental model and time point, 6-10 mice were analyzed and both
201 male and female mice were used in separate groups.

202 **Aortic single-cell preparation and single-cell RNA (scRNA) sequencing**

203 WT and DKO mice were euthanized by CO2 inhalation. The aortas were isolated after
204 perfusion with 30 mL of PBS through left ventricular and quickly transferred to cold DMEM
205 medium. Aortas from the two groups were cut into about small pieces and digested with an enzyme
206 solution (5mg/mL collagenase type I, 5mg/mL collagenase type IV, and 5mg/mL liberase) for
207 90min at 37 °C on a shaker. The digested cell suspension was filtered through a 40 μm strainer
208 and washed twice with PBS. The cells were resuspended and ready for sequencing in PBS with
209 0.04% bovine serum albumin, and their viability was over 90%.

210 Single-cell RNA-Seq library construction was performed using the protocol provided by 10X
211 Genomics. In brief, the single-cell suspensions from both groups, reagents, gel beads and
212 partitioning oil were loaded to 10X Chromium Chip G to generate single-cell Gel Beads-in-
213 emulsion (GEMs, Single cell 3' Reagent Kits v3.1, 10X Genomics). scRNA was barcoded through
214 reverse transcription in individual GEMs followed by a post GEM-RT cleanup and cDNA
215 amplification. Then, a 3'-gene expression library construction was performed. Finally, the library
216 was sent for sequencing.

217 **ScRNA-seq data analysis and metabolite-sensor communication inference**

218 The raw scRNA-seq data were processed using Cell Ranger (version 6.1.2) (10x Genomics).
219 The reads were mapped to the prebuilt mouse mm10 genome. The resulted gene expression matrix
220 in individual single cells was processed by the R package Seurat (version 4.1.0) [49]. Low-quality

221 cells with number of expressed genes less than 200 or larger than 5000 or with percentage of
222 mitochondria reads greater than 10% were dropped out. Rarely expressed genes which were
223 detected in less than 3 cells were removed. Mitochondria genes and ribosomal protein coding genes
224 were removed from the expression matrix before normalization. The high-quality data after these
225 filtering steps was then used at additional processing steps including log normalization, data
226 scaling, principal component analysis (PCA), cell clustering, and UMAP visualization. The cell
227 clusters were visualized by the DimPlot function. Differentially expressed genes among cell
228 clusters were identified by FindAllMarkers function using the default Wilcoxon test method, with
229 minimal percentage of expressed cells as 25% and minimal log2 fold change as 0.25. Next, marker
230 genes in each cell clusters were used to annotate cell types based on known marker genes in
231 PanglaoDB database [50] and literatures. The marker gene expressions were visualized by DotPlot
232 and VlnPlot function. Trajectory analysis was conducted by Monocle3 [51,52]. The metabolite-sensor
233 cell-cell communication was analyzed by MEBOCOST [53]. The data was analyzed following the
234 tutorial on the MEBOCOST website (https://github.com/zhengrongbin/MEBOCOST). scRNA-
235 seq expression data was used to estimate metabolite abundance and calculate communication score
236 for each condition. Next, results of two conditions were combined to compare the communications.
237 The differences in communication scores between two conditions were calculated. The prediction
238 of sender-metabolite-sensor-receiver communication events were visualized by barplot, flow plot
239 and circle plot. The metabolite abundance and sensor expression levels were exhibited by violin
240 plot. Index of dispersion (IOD) was calculated using communication scores across conditions as
241 described in the MEBOCOST paper[53]. The top 100 most variable communications were selected
242 for further investigation. All the data for scRNA-seq are available in Data files (S1-S2).

243 **Human samples**

244 Human healthy control (n=3) and diseased aortic arch samples (n=3) from atherosclerosis
245 patients were purchased from Maine Medical Center Biobank. The medical information of the
246 atherosclerotic patient samples is in Data file S9. The paraffin sections were de-paraffinized and
247 performed antigen retrieval to unmask the antigenic epitope with 10mM Sodium Citrate, pH 6.0,
248 with 0.5% Tween 20 at 90°C for 10 minutes. Immunofluorescence staining of the slides was
249 performed with the standard protocol described below.

250 **Synthesis of DSPE-PEG-S2P, preparation and characterization of S2PNP-siRNA**

251 To construct the lesional macrophage-targeted siRNA NPs, S2P peptide-conjugated DSPE-
252 PEG (DSPE-PEG-S2P) was first synthesized via a thiol-maleimide Michael addition click reaction
253 between S2P peptide (CRTLTVRKC, GLS Biochem Systems Inc.) and DSPE-PEG-Mal [PEG
254 molecular weight, 3.4 kDa; Nanocs Inc.], as reported previously [54]. Then, a robust self-assembly
255 method was used to prepare the targeted polymer-lipid hybrid NPs for siRNA delivery [54,55]. In brief,
256 G0-C14 and PLGA were dissolved separately in anhydrous dimethylformamide (DMF) to form a
257 homogeneous solution at the concentration of 2.5 mg/mL and 5 mg/ml, respectively. DSPE-PEG-
258 OCH3 (DSPE-mPEG) and DSPE-PEG-S2P were dissolved in HyPure water (GE Healthcare Life
259 Sciences, catalog no. SH30538) at the concentration of 0.1 mg/mL. 1 nmol Epsin1 siRNA and 1
260 nmol Epsin2 siRNA were gently mixed with 100 μL of the G0-C14 solution. The mixture of
261 siRNA and G0-C14 was incubated at room temperature for 15 min to ensure the full electrostatic
262 complexation. Next, 500 μL of PLGA polymers were added and mixed gently. The resultant
263 solution was subsequently added dropwise into 10 mL of HyPure water containing 1 mg lipid-
264 PEGs (i.e., 50% DSPE-PEG-S2P and 50% DSPE-mPEG hybrids for the S2P-targeted siRNA NPs,
265 or 100% DSPE-mPEG for the non-targeted siRNA NPs) under magnetic stirring (1,000 rpm) for
266 30 min. The siRNA NPs were purified by an ultrafiltration device (EMD Millipore, MWCO 100

267 kDa) to remove the organic solvent and free excess compounds via centrifugation at 4 °C. After
268 washing 3 times with HyPure water, the siRNA NPs were collected and finally resuspended in pH
269 7.4 PBS buffer. The NPs were used freshly or stored at -80 °C for further use. The physicochemical
270 properties (particle size and surface charge) of S2PNP-siEpsin1/2 were characterized by dynamic
271 light scattering (DLS, Brookhaven Instruments Corporation). The S2PNP-siEpsin1/2 was ~89 nm
272 in size as measured by DLS, and their surface charge was determined to be ~ -5.3 mV.

273 **Statistical analysis**

274 Statistical analysis was processed using GraphPad Prism 8.4. Data are shown as mean ±
275 standard deviation (mean ± SD). Normality was determinedusing D'Agostino-Pearson normality
276 testing for experiments with n ≥ 8 and Kolmogorov-Smirnovnormality testing for experiments
277 with n < 8. Data were analyzed by the unpaired Student's t-test or Mann-Whitney U test where
278 appropriate for two groups. Data for multiple groups were analyzed with ANOVA with Bonferroni
279 test or Dunn'smultiple comparison test where appropriate. P value less than 0.05 was considered
280 significant.

281

282 **RESULTS**

283 **Single-cell RNA-seq revealed that macrophage Epsins regulate cholesterol metabolism and**
284 **efflux pathways**

285 For an unbiased analysis of all pathways regulated by Epsins in macrophages, we performed
286 single-cell RNA sequencing (scRNA-seq) analysis of aortic tissue isolated from wild type (WT)
287 and macrophage-specific DKO mice. We identified a diverse range of cell types, including
288 vascular smooth muscle cells (VSMCs), fibroblasts, endothelial cells, macrophages, and other cells
289 (Figure 1A). Known cell markers facilitated the annotation of cell types, such as the Tagln and

290 Acta2 for VSMCs, Pecam1 and Cdh5 for endothelial cells, Cd14 and Cd68 for macrophages[50,56,57]
291 (Figure S1A). Macrophage populations were further subclustered to investigate their
292 heterogeneity among subpopulations (Figure 1B). Multiple well-known macrophage
293 subpopulations were recaptured, including M1 and M2 macrophages. Markers reported in the
294 literature were used to annotate the subtypes(*e.g.,* Mrc1 (Cd206) and Cd163 for M2
295 macrophages)[58] (Figure S1B and S1C). The composition of the aortic cell population showed
296 striking differences between WT and DKO aortic cells (Figure S2).
297 The molecular mechanisms underlying Epsin-mediated regulation of foam cell formation and
298 promotion of lipid uptake by macrophages are poorly understood. We therefore employed the
299 algorithm MEBOCOST, which is the first algorithm developed to detect cell communications
300 mediated by metabolites and their sensor proteins such as receptors and transporters (metabolite-
301 sensor cell communications) [53]. The results showed that macrophage subpopulations and VSMCs
302 were the top cell types ranked by the number of metabolite-sensor cell communications from the
303 largest to the smallest (Figure 1C). Furthermore, the numbers of metabolite-sensor cell
304 communications in these cell populations increased in DKO compared to WT (Figure 1C).
305 Macrophage subpopulations were found to not only send metabolites to other cell types, but also
306 receive metabolites from other cell types. They could send and receive metabolites in an autocrine
307 manner as well (Figure 1D). The communications between a pair of cell populations can be
308 mediated by multiple metabolite-sensor pairs. The overall changes in communication were
309 estimated by the median differences of communication scores between any two cell groups. We
310 observed widespread changes of cell-cell communications in DKO when compared to WT, with
311 both strengthened and weakened communications (Figure 1D). To gain a deeper insight into the
312 changed metabolite-sensor cell communications related to macrophages, we inspected individual

313 sender cell types of metabolites and receiver cell types of sensor proteins. First, we observed a
314 decrease of cholesterol-Cd36 cell communications from macrophages, especially in macrophage
315 cluster 2 (c2), to other cell types in DKO compared to WT (Figure 1E); second, cholesterol-Cd36
316 cell communications from macrophage c2 to macrophage c1 were reduced by the DKO (Figure
317 1F). As for the specificity of metabolite and sensor abundance in different cell types, we observed
318 that cholesterol and its derivative, 25-hydroxycholesterol, were highly-enriched in macrophage
319 populations; Cd36, the receptor of cholesterol, was also highly expressed in macrophage
320 populations (Figure 1G). The cell communications through cholesterol and Cd36 in macrophages
321 was supported by their abundance in these cells. Finally, the most variable communications in
322 macrophages mediated by cholesterol appeared to be mostly decreased rather than increased
323 (Figure 1H).

324 We subsequently performed bulk RNA-seq analysis of macrophages and revealed that loss of
325 Epsins 1 and 2 significantly altered the expression of 2208 genes (Figure S3). These include 1138
326 downregulated and 1070 upregulated genes (Figure S3A). Notably, the differential genes are
327 associated with cholesterol efflux and metabolism, suggesting that Epsins play a role in regulating
328 lipid cholesterol metabolism and efflux pathways (Figure S3B). Consistently, Gene Set
329 Enrichment Analysis (GSEA) showed that genes related to fatty acid metabolism tended to be
330 markedly downregulated in DKO macrophages (Figure S3C). In contrast, genes associated with
331 cholesterol transport and efflux (Figure S3D), and negative regulation of macrophage foam cell
332 formation (Figure S3E), tended to be upregulated by Epsin deficiency.

333 We next compared our DKO macrophage RNA-seq data with a public RNA-seq data from
334 wild type and CD36 knockout (CD36KO) macrophages in the public database [59]. We observed a
335 significant overlap of differential genes induced by the Epsin-DKO and CD36KO mouse

336 macrophages. There were 169 genes significantly upregulated by both Epsin-DKO and CD36KO
337 (4-fold enrichment compared to the 41 genes expected by random chance, Fisher's exact test P
338 value 9.73 x 10^{-25}) (Figure S3F left panels); 29 genes (6-fold enrichment, Fisher's exact test P value
339 6.15 x 10^{-9}) were downregulated by both Epsin-DKO and CD36KO (Figure S3F right panels). GO
340 analysis revealed multiple pathways regulated by both Epsin or CD36 deficiency. These include
341 the downregulation of inflammation pathways, lipid biosynthetic processes, triglyceride metabolic
342 processes, and upregulation of the small GTPase-mediated signal transduction pathway (Figure
343 S3G). The results indicated that Epsins and CD36 may have superimposing roles in regulating
344 molecular pathways involved in lipid metabolism and inflammation.
345
346 **Epsin promotes CD36-mediated lipid uptake by promoting CD36 endocytosis and recycling**
347 Based on the bioinformatic results, we hypothesized that Epsins regulate CD36 internalization
348 and thus lipid uptake. We performed qRT-PCR, western blot (WB) and flow cytometry to check
349 the RNA, total protein, and surface protein levels of CD36. Interestingly, RNA (Figure 2A) and
350 total protein (Figure 2B) expression of CD36 remained unchanged between WT and DKO
351 macrophages; however, the surface protein level of CD36 significantly decreased with the
352 treatment of oxLDL in clathrin-dependent manner in WT, but not in DKO macrophages (Figure
353 2C and S4A-C). Immunofluorescence staining (IF) revealed oxLDL-induced CD36 trafficking to
354 early endosomes. We observed colocalization of CD36 with EEA1 (early endosome antigen 1,
355 Figure 2D) and Rab11 (recycling endosome marker, Figure 2E) in WT macrophages treated with
356 oxLDL, which was not observed in DKO macrophages.
357 To further study the role of Epsins in regulating macrophage lipid uptake, we stained oxLDL-
358 treated WT and DKO macrophages with BODIPY and Oil Red O (ORO). Deficiency of Epsins

359 impaired oxLDL uptake and foam cell formation (Figure 2F and S5A-B) and reduced cholesterol
360 and triglyceride levels (Figure 2G) in DKO macrophages. Flow cytometry confirmed that
361 macrophage lipid uptake was reduced in DKO macrophages using DiI-oxLDL treatment (Figure
362 2H and S4B). Together, these results indicate that Epsins are crucial for CD36-mediated lipid
363 uptake and cholesterol metabolism.
364
365 **Epsin ENTH domain is required for CD36-mediated lipid uptake and foam cell formation**
366 Next, we investigated how Epsins and CD36 interact to cause the disparity in CD36 surface
367 and total protein levels using immunoprecipitation (IP) and WB. We determined that CD36 binds
368 Epsin1 in WT, but not in DKO macrophages (Figure 3A). This indicated that Epsin1 and CD36
369 interact endogenously. We then determined which Epsin regions were responsible for this
370 interaction. We created Flag-tagged mammalian Epsin1 wild type full length and ENTH or UIM
371 deleted constructs (FLAG-Epsin1^{WT}, FLAG-Epsin1$^{\Delta ENTH}$ or FLAG-Epsin1$^{\Delta UIM}$) (Figure 3B). We
372 transfected these constructs to HEK 293T cells and performed co-IP with CD36. The interaction
373 between Epsin1 and CD36 was dependent on the ENTH domain as the binding between
374 Epsin1$^{\Delta ENTH}$ and CD36 was dramatically reduced in FLAG-Epsin1$^{\Delta ENTH}$-expressing cells (Figure
375 3B). As expected, we did not detect ubiquitinated CD36 in response to oxLDL treatment in the
376 presence of the proteasome inhibitor MG132 (Figure 3C). In addition, we transfected the Epsin
377 full length and deletion Epsin constructs into WT and DKO macrophages treated with oxLDL. The
378 transfection of full-length Epsin restored lipid uptake in DKO macrophages, which was not
379 observed in cells expressing FLAG-Epsin1$^{\Delta ENTH}$ (Figure 3D, 3E and S6).
380

381 **RNA-seq analyses of WT, Epsin-DKO and ABCG1-KO macrophages reveal that Epsins and**
382 **ABCG1 reciprocally regulate inflammation and lipid metabolism pathways**

383 Emerging evidence supports raising RCT function by increasing HDL-cholesterol efflux
384 capacity (CEC) to treat recurrent heart attacks. We have generated myeloid-specific ABCG1-
385 knock out (ABCG1-KO) mice. Given the intimate relationship of HDL with ABCG1 in regulating
386 cholesterol efflux, and the involvement of Epsins in cholesterol efflux regulation, we performed
387 RNA-seq analysis of WT, ABCG1-KO and Epsin-DKO macrophages. The loss of ABCG1 in
388 macrophages significantly altered the expression of 1733 genes, including 986 downregulated and
389 747 upregulated genes (Figure S7A-S7C). GSEA indicated that genes associated with the
390 inflammatory response (Figure 4A) and macrophage activation (Figure 4B) are upregulated by
391 ABCG1-KO in macrophages. In contrast, genes negatively regulating macrophage-derived foam
392 cell formation are downregulated by ABCG1-KO (Figure 4C). We then performed GO enrichment
393 analysis for genes up- and down-regulated in ABCG1-KO relative to WT macrophages. Positive
394 regulation of cytokine production, tumor necrosis factor production and acute inflammatory
395 response were upregulated by ABCG1-KO in macrophages (Figure 4D). Negative regulation of
396 lipid storage and cholesterol biosynthetic processes were down regulated in ABCG1-KO compared
397 to WT macrophages (Figure 4D). Interestingly, GSEA analyses showed that genes associated with
398 cell immune responses (Figure S7D), regulation of leukocyte migration (Figure S7E) and
399 leukocyte proliferation (Figure S7F) are markedly upregulated by ABCG1 deficiency in
400 macrophages. In contrast, these genes are downregulated in DKO macrophages (Figure S7D-S7F),
401 These results suggest that Epsins and ABCG1 reciprocally regulate inflammation pathways.
402 Examination of individual gene expression confirmed common target genes reversely regulated
403 by Epsins and ABCG1. For instance, Itgb3 prevents the differentiation of macrophages and

404 monocytes into foam cells [60] and it was up and down regulated by DKO and ABCG1-KO,
405 respectively (Figure 4E). In addition, GO enrichment analysis revealed pathways conversely
406 regulated by ABCG1-KO and DKO in macrophages (Figure 4F). Therefore, our RNA-seq analyses
407 from ABCG1-KO and Epsin-DKO further supports our findings that Epsins and ABCG1 play
408 opposing roles in regulating cholesterol efflux, inflammatory responses, and foam cell formation.
409

410 **Epsin loss augments macrophage cholesterol efflux *in vitro* and RCT *in vivo***

411 RNA-seq analysis of WT, DKO and ABCG1-KO macrophages indicated that the loss of Epsins
412 affects cholesterol efflux. At the same time, we wanted to determine if Epsins inhibit cholesterol
413 efflux and RCT to ameliorate atherosclerosis. WT and DKO macrophages were pre-treated with a
414 liver X receptor (LXR) agonist (T0901317) and incubated with [^{3}H]-cholesterol and ac-LDL. We
415 found that *in vitro* cholesterol efflux to HDL, but not ApoA-1, was markedly enhanced in DKO
416 versus WT macrophages (Figure 5A and 5B). Consistently, *in vivo* RCT (Figure 5C) was elevated
417 in mice injected with [^{3}H]-cholesterol-loaded DKO macrophages compared to WT macrophages.
418 Our results showed that [^{3}H]-radioactivity in liver, plasma, feces, and intestinal contents all showed
419 significant increases in mice injected with DKO macrophages, but not those injected with WT
420 macrophages (Figure 5D-5I and S8). These findings suggest that Epsin-deficient macrophages
421 have higher cholesterol efflux and RCT.
422

423 **Epsin-UIM domain binds ABCG1 to promote degradation via the lysosome**

424 To investigate the molecular mechanisms underlying Epsin-mediated ABCG1 regulation, we
425 tested whether Epsins interact with ABCG1 and governed its turnover in macrophages. We first
426 assessed protein levels of surface receptors such as ABCG1, ABCA1, SR-A1, and LDLR in

427 macrophages involved in the progression of atherosclerosis. WB results showed that ABCG1, but
428 not ABCA1, SR-A1 and LDLR, were upregulated in primary macrophages from DKO mice when
429 compared to WT mice (Figure 6A). The mRNA levels of ABCG1 in both WT and DKO
430 macrophages remain unchanged (Figure S9). Because ABCG1 is known to mediate cholesterol
431 efflux to HDL [48], we hypothesized that Epsins bind ABCG1 under atherosclerotic conditions and
432 promote ABCG1 ubiquitin-dependent degradation to inhibit cholesterol efflux in macrophages and
433 facilitate the development of atherosclerosis. When the isolated peritoneal macrophages from
434 DKO and WT mice were pretreated with a LXR activator followed by a cell surface biotinylation
435 assay, we observed significantly elevated levels of biotinylated ABCG1 in DKO macrophages
436 (Figure 6B). We also performed flow cytometry and observed that only WT macrophages showed
437 a decreased surface level of ABCG1 with the oxLDL treatment in a clathrin-dependent way (Figure
438 6C and S10A-C). Therefore, decreased total and surface levels of ABCG1 in WT macrophages
439 implies that Epsins promote ABCG1 degradation.

440 We next determined how Epsins cause increases in total and surface protein levels of ABCG1
441 in macrophages from DKO mice. When peritoneal- or bone marrow-derived macrophages from
442 WT and DKO mice were lysed and processed for IP with anti-Epsin1 antibodies, we observed
443 ABCG1 in WT macrophages, but not in DKO macrophages (Figure 6D). This suggested that
444 Epsins bind to ABCG1. Accordingly, we showed that Epsin interacted with ABCG1 through the
445 Epsin UIM domain, which was confirmed by transfection of Flag-tagged mammalian Epsin wild
446 type full length, ENTH or UIM deletion constructs as well as ABCG1 plasmid to HEK 293T cells
447 (Figure 6E). We showed that ABCG1 is ubiquitinated in response to oxLDL, allowing Epsins to
448 interact with ABCG1 through their UIM, which promotes ABCG1 lysosomal degradation (Figure

449 6F). In addition, we observed oxLDL-induced ABCG1 trafficking to early endosomes (Figure 6G)
450 and lysosomes (Figure 6H) in WT macrophages, but not DKO cells.

451 To confirm that elevated cholesterol efflux and RCT were a result of increased total and surface
452 levels of ABCG1 in ApoE$^{-/-}$/LysM-DKO macrophages, we created ApoE$^{-/-}$/LysM-DKO-ABCG1$^{fl/+}$
453 mice by crossing the ApoE$^{-/-}$/LysM-DKO mouse strain with ABCG1 (flox/+) heterozygous mice
454 to generate a novel mouse model (ApoE$^{-/-}$/LysM-DKO/ABCG1$^{myeloid\text{-}het}$) with genetically-reduced
455 ABCG1 levels in Epsin-deficient macrophages (Figure 5J). We observed reduced gene (Figure
456 5K) and protein (Figure 5L) expression of ABCG1 in ApoE$^{-/-}$/LysM-DKO-ABCG1$^{fl/+}$
457 macrophages. The LysM-DKO-ABCG1$^{fl/+}$ macrophages showed less cholesterol efflux to HDL
458 and RCT compared to ApoE$^{-/-}$/LysM-DKO macrophages (Figure 5A, 5B and 5D-5I). These studies
459 demonstrated that Epsin deficiency in macrophages specifically enhanced ABCG1-mediated
460 cholesterol efflux to HDL and RCT, which is inversely related to the risk of atherosclerotic
461 cardiovascular disease[34]. In accordance, immunostaining of human patient aortic arch (Figure
462 S11A) and mouse aortic root (Figure S11B) sections revealed that ABCG1 expression is inversely
463 associated with atherosclerotic plaque severity, *i.e.,* there is considerable reduction in ABCG1
464 expression in more severe atheroma compared to that in less severe atherosclerotic plaques in both
465 human and mouse atheromas.

466

467 **S2PNP-siEpsin1/2 hinders progression of early and advanced stages of atherosclerosis**

468 Since we found that Epsins facilitate CD36-mediated lipid uptake and promote ABCG1
469 degradation to inhibit ABCG1-mediated cholesterol efflux, we sought to determine whether
470 targeting Epsins could prevent the progression of atherosclerosis. We used a targeted NP platform

471 [54] modified with a lesional macrophage-specific targeting peptide (S2P) for systemic delivery of
472 Epsins 1 and 2 siRNA combinations (S2PNP-siEpsin1/2) (Figure S12A).

473 Isolated macrophages from WT mice were treated with S2PNP-siControl (S2PNP-siCtrl) or
474 S2PNP-siEpsin1/2. Then, RNA and protein were isolated to check the *in vitro* silencing efficacy
475 of the NPs (Figure S12B and S12C). To assess the effect of NPs on *in vitro* peritoneal macrophage
476 lipid loading, cells isolated from ApoE$^{-/-}$ mice were treated with S2PNP-siCtrl or S2PNP-
477 siEpsin1/2 for 24h followed by treatment with oxLDL or plasma isolated from ApoE$^{-/-}$ mice fed a
478 WD for 8 weeks. The treatment of oxLDL or plasma demonstrated decreased lipid uptake by
479 S2PNP-siEpsin1/2-treated macrophages compared to S2PNP-siCtrl treated cells (Figure S13A and
480 S13B).

481 ApoE$^{-/-}$ mice fed a WD for 8 weeks (early stage, Figure S14) or 17 weeks (advanced stage,
482 Figure 7) were divided into three groups including baseline (before NP injection), S2PNP-siCtrl,
483 and S2PNP-siEpsin1/2. The baseline group was sacrificed before the injection of NPs.

484 S2PNP-siCtrl or S2PNP-siEpsin1/2 was intravenously injected twice a week for 3 weeks
485 (Figure S14A and 7A). Digested lesions from S2PNP-siCtrl or S2PNP-siEpsin1/2 treated mice
486 were used for WB to check *in vivo* silencing of Epsins 1 and 2 (Figure S14B). Additionally, the
487 administration of S2PNP-siEpsin1/2 resulted in not only a decrease in lesional macrophage
488 accumulation, but also a significant reduction of Epsins 1 and 2 expressions within the
489 atherosclerotic plaques as showed by diminished CD68 and Epsins 1 and 2 staining in the aortic
490 root sections (Figure S14C and S14D). *En face* ORO staining in aortas, aortic roots, and
491 brachiocephalic artery (BCA) sections (Figure S14E, 7B and 7C) showed reduced lesion size,
492 lesion number, and retarded progression of both early (11 weeks on WD) and advanced (20 weeks

493 on WD) stages atherosclerosis in ApoE$^{-/-}$ mice treated with S2PNP-siEpsin1/2 opposed to the
494 S2PNP-siCtrl group.

495 Inhibiting the transition of atheroma from stable lesion to vulnerable plaque is paramount in
496 preventing heart attacks and strokes. We observed elevated smooth muscle cell contents and
497 reduced macrophage accumulation (Figure 7D), increased elastic fibers and collagen content
498 (Figure S15), and reduced necrotic core area (Figure 7E) within the atherosclerotic lesions in
499 S2PNP-siEpsin1/2 treated mice compared to S2PNP-siCtrl group. In addition, we observed no
500 changes in plasma total cholesterol, triglycerides, or HDL and non-HDL cholesterol levels
501 between S2PNP-siCtrl and S2PNP-siEpsin1/2 treated mice (Figure S16). These features suggest
502 that the administration of lesion macrophage-specific targeting NPs containing Epsin1/2 siRNA
503 can stabilize the atherosclerotic plaques without affecting the plasma cholesterol levels.

504

505 **S2PNP-siEpsin1/2 promotes atheroma resolution by diminishing inflammation and**
506 **enhancing lesion stability**

507 Given the critical role of macrophage cholesterol efflux and RCT in atheroma resolution, we
508 also wanted to assess the therapeutic effects of S2PNP-siEpsin1/2 on atheroma resolution. We
509 established another mouse model by injecting proprotein convertase subtilisin kexin type 9-adeno-
510 associated virus-8 (AAV8-PCSK9D377Y) into C57BL/6 mice. This generated an atherosclerosis
511 mouse model harboring a gain-of-function PCSK9 mutant [61]. This model mimics LDLR null mice
512 [26] and requires no genetic modification [61]. Another advantage of this mouse line is that a single
513 AAV injection is sufficient to generate atherosclerotic mice by WD feeding compared to long-
514 term crossbreeding with ApoE$^{-/-}$ or LDLR$^{-/-}$ mice.

515 To test if S2PNP-siEpsin1/2 treatment can promote atheroma resolution, PCSK9-AAV8 mice
516 fed a WD for 16 weeks followed by 4 weeks of a normal diet with S2PNP-siCtrl or S2PNP-
517 siEpsin1/2 treatment (Figure 8A). The latter group showed a significant reduction of lesion size
518 and rapid lesion regression as evidenced in the IF and ORO staining of the whole aorta, aortic root
519 and BCA sections (Figure 8B, 8C, 8D and S17A). Van Gieson's trichrome staining of BCA
520 sections showed increased collagen content and elastic fibers in the S2PNP-siEpsin1/2 group
521 compared to S2PNP-siCtrl or baseline group (Figure S17B). In addition, the IF co-staining of
522 CD68 and α-SMA showed reduced macrophage accumulation in the fibrous cap, reduced size of
523 atheromatous cores, and increased smooth muscle cell content within the atheroma cap in the
524 S2PNP-siEpsin1/2 group (Figure 8C).

525 Adhesion molecules play a crucial role in attaching monocytes to activated endothelial cells
526 (EC) as well as recruiting monocytes to the sub-endothelial layer. Co-staining of CD31 with
527 vascular cell adhesion molecule-1 (VCAM-1), intercellular adhesion molecule-1 (ICAM-1), P-
528 selectin or E-selectin (Figure 8E-8I) was performed using aortic root sections. Administration of
529 S2PNP-siEpsin1/2 significantly suppressed these adhesion molecules when compared to S2PNP-
530 siCtrl group. In addition, the expression of the macrophage egressing gene CCR7 was significant
531 increased, while the retention genes Sema3a and Netrin1 were decreased in DKO macrophages
532 (Figure S17C). This is consistent with our RNA-seq analysis that showed the deficiency of
533 macrophage Epsins facilitates immune cell migration. Furthermore, macrophages treated with
534 S2PNP-siEpsin1/2 showed decreased expression of pro-inflammatory genes (iNOS, IL-6, IL-1β,
535 and TNF-α) and increased expression of anti-inflammatory markers (IL-10 and Arg1) compared
536 to the S2P-siCtrl group (Figure 8J). These decreased pro-inflammatory cytokines lead to reduced
537 ICAM-1, VCAM-1, P- and E-selectins expression in ECs (Figure 8E-8H), hindering recruitment

538 of additional macrophages to the lesion. Taken together, these results indicate that specific
539 silencing of Epsins in lesional macrophages may offer therapeutic benefits in preventing or treating
540 advanced atherosclerosis.
541

542 **DISCUSSION**

543 In this study, we discovered that Epsins 1 and 2 govern cholesterol transport (Figure S18) in
544 atherosclerotic macrophages by regulating CD36-mediated lipid uptake (Figure 1-3 and S1-S6)
545 and ABCG1-dependent cholesterol efflux (Figure 4-6 and S7-S11). Importantly, we
546 demonstrated that targeting lesional macrophage Epsins using a newly developed
547 nanotechnology-based siRNA-mediated therapy halts inflammation, impedes early and late
548 atherogenesis (Figure 7 and S12-S16), and accelerates atheroma resolution (Figure 8 and S17).
549 By silencing lesional macrophage Epsins, we observed a reduction in necrotic core area in
550 atherosclerotic lesions and marked attenuation in inflammation (Figure 7 and Figure 8). Together,
551 our studies point toward a promising new strategy for the treatment of atherosclerosis.

552 The advent of next generation therapies targeting PCSK9, including monoclonal anti-PCSK9
553 antibodies and PCSK9 siRNA, is considered to be game-changing [62-64]; however, these and other
554 therapies largely ignore the rampant inflammation that occurs in atherosclerotic arteries. Arterial
555 inflammation is a prime contributor to the transition from a stable to vulnerable atheroma [7-10].
556 While anti-inflammatory medicines such as anti-Interleukin-1β antibodies potently diminish the
557 risk of recurrent myocardial infarction, these treatments may come with some severe side effects
558 [65,66]. In addition, the inability to reduce lipid ingestion while concomitantly reinforce cholesterol
559 efflux in lesional macrophages has impeded the battle against atherosclerosis. Our mechanistic
560 studies show that Epsins bind to CD36 to facilitate lipid uptake by enhancing CD36 endocytosis

561 and recycling. Conversely, Epsins promote ABCG1 degradation via lysosomes and hamper
562 ABCG1-mediated cholesterol efflux and reverse cholesterol transport. Excitingly, by harnessing
563 the latest development in nanomedicine and developing S2P-NPs carrying Epsin1/2 siRNAs
564 (S2PNP-siEpsin1/2), we show a reduction in plaque formation in both early and advanced
565 atherosclerosis (Figure S14 and 7). Furthermore, in a pre-clinical atheroma resolution model, this
566 potent approach reduced lesional macrophage accumulation, decreased pro-inflammatory
567 cytokine and adhesion molecule expression, and accelerated plaque regression (Figure 8). Taken
568 together, our study uncovers a novel and critical role for Epsin in regulating lipid metabolism and
569 cholesterol efflux as well as offers a potential new nanotherapy for treating atherosclerosis by
570 targeting Epsins in macrophages.

571 As we show that silencing of lesional macrophage Epsins reduces necrotic core size, we
572 reasoned that inhibiting Epsins may reinforce efferocytosis in macrophages, analogous to our
573 observations in DKO macrophages [26] given that efferocytosis plays a central role in regulating
574 necrotic core formation [67-69]. Despite the fact that S2P-NPs have been shown to only negligibly
575 target the endothelium [54], whether S2PNP-siEpsin1/2 prohibits endothelial Epsins to
576 synergistically curb atherosclerosis may require further investigation as deletion of endothelial
577 Epsins also reduces inflammation and atherogenesis [24,25]. Interestingly, we did not observe
578 significant changes of the lipid profiles in the plasma from S2PNP-siCtrl and S2PNP-siEpsin1/2
579 treated ApoE$^{-/-}$ mice, suggesting either a minor liver targeting by S2PNP-siEpsin1/2 or that S2PNP-
580 siEpsin1/2-mediated silencing of Epsins in liver could be inconsequential. Nevertheless, whether
581 S2PNP-siEpsin1/2 targets liver epsins warrants further investigation.

582 While autophagy can eliminate excess lipid droplet-associated cholesterol esters taken up by
583 macrophages [70-73], this process is attenuated during atheroma progression, leading to defective

584 lipolysis, impaired efferocytosis, and escalated inflammation, which increases the likelihood of
585 vulnerable lesion rupture [70-76]. A recent report suggests that macrophage SR-B1 modulates
586 autophagy through the VPS34 complex and PPARα transcription of Tfeb in atherosclerosis [77]. SR-
587 B1 is a multifunctional membrane receptor, which is not only responsible for selective uptake of
588 HDL- derived cholesteryl esters into cells, but also for transferring HDL-cholesterol efflux from
589 peripheral tissues to back to liver [78]. Given that Epsins are implicated in autophagy function in
590 *Drosophila* [79], the question of whether these proteins suppress autophagic activity by binding to
591 SR-B1 and inhibiting SR-B1-regulated function in macrophages remains unanswered.

592 Our studies also revealed that LXR-activated macrophage surface expression of ABCG1 was
593 significantly reduced with oxLDL treatment in WT, but not in DKO macrophages owing to their
594 internalization and degradation mediated by the Epsins (Figure 6). It is thought that basal
595 macrophage ABCG1 is largely located at an intracellular location [80] and then redistributed to the
596 cell surface following LXR activation [81]. Our immunostaining and biotinylation studies (Figure 6)
597 are consistent with these observations. More importantly, staining of ABCG1, in both human
598 patient aortic arch and mouse aortic root sections, exhibits a reduction in ABCG1 expression in
599 severe atherosclerotic lesions (Figure S11), suggesting a pivotal role of loss of Epsins in
600 maintaining the abundance of ABCG1 and limiting plaque buildup. Recent clinical trials suggest
601 that enhanced cholesterol efflux capacity (CEC) considerably reduces the risk of repeat heart
602 attacks and severe acute myocardial infarction (MI) [39-41]. In addition, cholesterol efflux capacity
603 has minimal links to various risk factors and metabolic issues in contrast to HDL cholesterol level
604 [45]. Our results show that targeting Epsins augments cholesterol efflux (Figure 5 and S16) and
605 consequently, may potentially enhance CEC, suggesting that inhibiting Epsins represents a
606 promising new strategy for treating patients suffering from recurrent MI and severe CAD.

607 In conclusion, our results provide a powerful proof-of-concept for the therapeutic potential of
608 Epsin siRNA-containing NPs to precisely target lesional macrophages to abolish inflammation and
609 resolve atheroma. By illustrating that targeting Epsins expression in macrophages restricts lipid
610 ingestion in foam cells and concomitantly enhances cholesterol efflux, we believe this study
611 provides a foundation for the renewed quest seeking innovative therapies that precisely resolve
612 lesional inflammation in advanced atherosclerosis.

613

614 **ACKNOWLEDGMENTS:** We thank researchers for providing their GEO database information
615 online. We thank the Flow Cytometry Core at Boston Children's Hospital for the use of the LSRII,
616 the Viral Core at Boston Children's Hospital for providing viral stocks, and the Biopolymers
617 Facility at Harvard Medical School for quality control analysis of RNA samples.

618 **SOURCES OF FUNDING:** This work was supported by R01HL146134 (H.C., S.S., M.F.L.) and
619 American Heart Association Established Investigator Award and Transformational Project Award
620 (H.C.), and in part by NIH grants R01HL137229, R01HL141853, R01HL156362, R01HL158097,
621 R01HL162367, (H.C.), AHA 17SDG33410868 (H.W.), R01GM125632 (K.F.C.), and P01
622 HL116263 (M.F.L.).

623 **AUTHOR CONTRIBUTIONS:** K.C. J.S., K.F.C. and H.C. conceived and designed the study.
624 K.C. primarily contributed to the identification of the in vitro molecular mechanism. K. C. and
625 B.W. primarily contributed to the in vivo data in atherosclerosis analysis. X.G., K.C. R.Z., and
626 K.F.C. conducted the RNA-seq data analysis and interpretation. H.W. and Y. D worked on part of
627 the molecular mechanism investigation and provided biochemistry insights. Y.X. and X.J.
628 synthesized, characterized the nanoparticles. M.M. performed the cholesterol and triglyceride
629 analysis. Y.L. and B.Z. provided technical support in RNA-seq experiment. K.C., D.S. and Q.P.

analyzed the data and provided comments. S.W. provided technical support with mouse genotyping and colony maintenance. K.C. and H.C. wrote the manuscript. K.C., D.B.C., K.L., S.S., M.F.L., J.S., K.F.C., and H.C. edited the manuscript. All the authors reviewed and provided feedback on the manuscript.

DISCLOSURES: All authors declare that they have no competing interests.

635 **REFERRENCES**

636 1. Libby P. Inflammation in atherosclerosis. *Arterioscler Thromb Vasc Biol*. 2012;32:2045-2051. doi:
637 10.1161/ATVBAHA.108.179705
638 2. Weber C, Noels H. Atherosclerosis: current pathogenesis and therapeutic options. *Nat Med*. 2011;17:1410-
639 1422. doi: 10.1038/nm.2538
640 3. Glass CK, Witztum JL. Atherosclerosis. the road ahead. *Cell*. 2001;104:503-516. doi: 10.1016/s0092-
641 8674(01)00238-0
642 4. Wang Y, Nanda V, Direnzo D, Ye J, Xiao S, Kojima Y, Howe KL, Jarr KU, Flores AM, Tsantilas P, et al.
643 Clonally expanding smooth muscle cells promote atherosclerosis by escaping efferocytosis and activating
644 the complement cascade. *Proc Natl Acad Sci U S A*. 2020;117:15818-15826. doi:
645 10.1073/pnas.2006348117
646 5. Sharma M, Schlegel MP, Afonso MS, Brown EJ, Rahman K, Weinstock A, Sansbury BE, Corr EM, van
647 Solingen C, Koelwyn GJ, et al. Regulatory T Cells License Macrophage Pro-Resolving Functions During
648 Atherosclerosis Regression. *Circ Res*. 2020;127:335-353. doi: 10.1161/CIRCRESAHA.119.316461
649 6. Steinberg D. The LDL modification hypothesis of atherogenesis: an update. *J Lipid Res*. 2009;50
650 Suppl:S376-381. doi: 10.1194/jlr.R800087-JLR200
651 7. Hansson GK, Libby P, Tabas I. Inflammation and plaque vulnerability. *J Intern Med*. 2015;278:483-493.
652 doi: 10.1111/joim.12406
653 8. Doring Y. Not growth but death: GM-CSF/IL-23 axis drives atherosclerotic plaque vulnerability by
654 enhancing macrophage and DC apoptosis. *Circ Res*. 2015;116:222-224. doi:
655 10.1161/CIRCRESAHA.114.305674
656 9. Alsheikh-Ali AA, Kitsios GD, Balk EM, Lau J, Ip S. The vulnerable atherosclerotic plaque: scope of the
657 literature. *Ann Intern Med*. 2010;153:387-395. doi: 10.7326/0003-4819-153-6-201009210-00272
658 10. Virmani R, Burke AP, Farb A, Kolodgie FD. Pathology of the vulnerable plaque. *J Am Coll Cardiol*.
659 2006;47:C13-18. doi: 10.1016/j.jacc.2005.10.065
660 11. Charo IF, Taub R. Anti-inflammatory therapeutics for the treatment of atherosclerosis. *Nat Rev Drug*
661 *Discov*. 2011;10:365-376. doi: 10.1038/nrd3444
662 12. De Camilli P, Chen H, Hyman J, Panepucci E, Bateman A, Brunger AT. The ENTH domain. *FEBS Lett*.
663 2002;513:11-18. doi: 10.1016/s0014-5793(01)03306-3
664 13. Itoh T, Koshiba S, Kigawa T, Kikuchi A, Yokoyama S, Takenawa T. Role of the ENTH domain in
665 phosphatidylinositol-4,5-bisphosphate binding and endocytosis. *Science*. 2001;291:1047-1051. doi:
666 10.1126/science.291.5506.1047
667 14. Rosenthal JA, Chen H, Slepnev VI, Pellegrini L, Salcini AE, Di Fiore PP, De Camilli P. The epsins define
668 a family of proteins that interact with components of the clathrin coat and contain a new protein module. *J*
669 *Biol Chem*. 1999;274:33959-33965. doi: 10.1074/jbc.274.48.33959
670 15. Cui K, Dong Y, Wang B, Cowan DB, Chan SL, Shyy J, Chen H. Endocytic Adaptors in Cardiovascular
671 Disease. *Front Cell Dev Biol*. 2020;8:624159. doi: 10.3389/fcell.2020.624159
672 16. Chen H, De Camilli P. The association of epsin with ubiquitinated cargo along the endocytic pathway is
673 negatively regulated by its interaction with clathrin. *Proc Natl Acad Sci U S A*. 2005;102:2766-2771. doi:
674 10.1073/pnas.0409719102
675 17. Shih SC, Katzmann DJ, Schnell JD, Sutanto M, Emr SD, Hicke L. Epsins and Vps27p/Hrs contain
676 ubiquitin-binding domains that function in receptor endocytosis. *Nat Cell Biol*. 2002;4:389-393. doi:
677 10.1038/ncb790
678 18. Polo S, Sigismund S, Faretta M, Guidi M, Capua MR, Bossi G, Chen H, De Camilli P, Di Fiore PP. A
679 single motif responsible for ubiquitin recognition and monoubiquitination in endocytic proteins. *Nature*.
680 2002;416:451-455. doi: 10.1038/416451a
681 19. Chen H, Ko G, Zatti A, Di Giacomo G, Liu L, Raiteri E, Perucco E, Collesi C, Min W, Zeiss C, et al.
682 Embryonic arrest at midgestation and disruption of Notch signaling produced by the absence of both epsin
683 1 and epsin 2 in mice. *Proc Natl Acad Sci U S A*. 2009;106:13838-13843. doi: 10.1073/pnas.0907008106
684 20. Tessneer KL, Pasula S, Cai X, Dong Y, McManus J, Liu X, Yu L, Hahn S, Chang B, Chen Y, et al. Genetic
685 reduction of vascular endothelial growth factor receptor 2 rescues aberrant angiogenesis caused by epsin
686 deficiency. *Arterioscler Thromb Vasc Biol*. 2014;34:331-337. doi: 10.1161/ATVBAHA.113.302586

21. Chang B, Tessneer KL, McManus J, Liu X, Hahn S, Pasula S, Wu H, Song H, Chen Y, Cai X, et al. Epsin is required for Dishevelled stability and Wnt signalling activation in colon cancer development. *Nat Commun*. 2015;6:6380. doi: 10.1038/ncomms7380
22. Liu X, Pasula S, Song H, Tessneer KL, Dong Y, Hahn S, Yago T, Brophy ML, Chang B, Cai X, et al. Temporal and spatial regulation of epsin abundance and VEGFR3 signaling are required for lymphatic valve formation and function. *Sci Signal*. 2014;7:ra97. doi: 10.1126/scisignal.2005413
23. Pasula S, Cai X, Dong Y, Messa M, McManus J, Chang B, Liu X, Zhu H, Mansat RS, Yoon SJ, et al. Endothelial epsin deficiency decreases tumor growth by enhancing VEGF signaling. *J Clin Invest*. 2012;122:4424-4438. doi: 10.1172/JCI64537
24. Dong Y, Wang B, Cui K, Cai X, Bhattacharjee S, Wong S, Cowan DB, Chen H. Epsins Negatively Regulate Aortic Endothelial Cell Function by Augmenting Inflammatory Signaling. *Cells*. 2021;10. doi: 10.3390/cells10081918
25. Dong Y, Lee Y, Cui K, He M, Wang B, Bhattacharjee S, Zhu B, Yago T, Zhang K, Deng L, et al. Epsin-mediated degradation of IP3R1 fuels atherosclerosis. *Nat Commun*. 2020;11:3984. doi: 10.1038/s41467-020-17848-4
26. Brophy ML, Dong Y, Tao H, Yancey PG, Song K, Zhang K, Wen A, Wu H, Lee Y, Malovichko MV, et al. Myeloid-Specific Deletion of Epsins 1 and 2 Reduces Atherosclerosis by Preventing LRP-1 Downregulation. *Circ Res*. 2019;124:e6-e19. doi: 10.1161/CIRCRESAHA.118.313028
27. Moore KJ, Freeman MW. Scavenger receptors in atherosclerosis: beyond lipid uptake. *Arterioscler Thromb Vasc Biol*. 2006;26:1702-1711. doi: 10.1161/01.ATV.0000229218.97976.43
28. Ouimet M, Ediriweera H, Afonso MS, Ramkhelawon B, Singaravelu R, Liao X, Bandler RC, Rahman K, Fisher EA, Rayner KJ, et al. microRNA-33 Regulates Macrophage Autophagy in Atherosclerosis. *Arterioscler Thromb Vasc Biol*. 2017;37:1058-1067. doi: 10.1161/ATVBAHA.116.308916
29. Kunjathoor VV, Febbraio M, Podrez EA, Moore KJ, Andersson L, Koehn S, Rhee JS, Silverstein R, Hoff HF, Freeman MW. Scavenger receptors class A-I/II and CD36 are the principal receptors responsible for the uptake of modified low density lipoprotein leading to lipid loading in macrophages. *J Biol Chem*. 2002;277:49982-49988. doi: 10.1074/jbc.M209649200
30. Podrez EA, Febbraio M, Sheibani N, Schmitt D, Silverstein RL, Hajjar DP, Cohen PA, Frazier WA, Hoff HF, Hazen SL. Macrophage scavenger receptor CD36 is the major receptor for LDL modified by monocyte-generated reactive nitrogen species. *J Clin Invest*. 2000;105:1095-1108. doi: 10.1172/JCI8574
31. Febbraio M, Podrez EA, Smith JD, Hajjar DP, Hazen SL, Hoff HF, Sharma K, Silverstein RL. Targeted disruption of the class B scavenger receptor CD36 protects against atherosclerotic lesion development in mice. *J Clin Invest*. 2000;105:1049-1056. doi: 10.1172/JCI9259
32. Nozaki S, Kashiwagi H, Yamashita S, Nakagawa T, Kostner B, Tomiyama Y, Nakata A, Ishigami M, Miyagawa J, Kameda-Takemura K, et al. Reduced uptake of oxidized low density lipoproteins in monocyte-derived macrophages from CD36-deficient subjects. *J Clin Invest*. 1995;96:1859-1865. doi: 10.1172/JCI118231
33. Ohashi R, Mu H, Wang X, Yao Q, Chen C. Reverse cholesterol transport and cholesterol efflux in atherosclerosis. *QJM*. 2005;98:845-856. doi: 10.1093/qjmed/hci136
34. Kennedy MA, Barrera GC, Nakamura K, Baldan A, Tarr P, Fishbein MC, Frank J, Francone OL, Edwards PA. ABCG1 has a critical role in mediating cholesterol efflux to HDL and preventing cellular lipid accumulation. *Cell Metab*. 2005;1:121-131. doi: 10.1016/j.cmet.2005.01.002
35. Westerterp M, Tsuchiya K, Tattersall IW, Fotakis P, Bochem AE, Molusky MM, Ntonga V, Abramowicz S, Parks JS, Welch CL, et al. Deficiency of ATP-Binding Cassette Transporters A1 and G1 in Endothelial Cells Accelerates Atherosclerosis in Mice. *Arterioscler Thromb Vasc Biol*. 2016;36:1328-1337. doi: 10.1161/ATVBAHA.115.306670
36. Yvan-Charvet L, Ranalletta M, Wang N, Han S, Terasaka N, Li R, Welch C, Tall AR. Combined deficiency of ABCA1 and ABCG1 promotes foam cell accumulation and accelerates atherosclerosis in mice. *J Clin Invest*. 2007;117:3900-3908. doi: 10.1172/JCI33372
37. Sag D, Cekic C, Wu R, Linden J, Hedrick CC. The cholesterol transporter ABCG1 links cholesterol homeostasis and tumour immunity. *Nat Commun*. 2015;6:6354. doi: 10.1038/ncomms7354
38. Moore KJ, Fisher EA. High-density lipoproteins put out the fire. *Cell Metab*. 2014;19:175-176. doi: 10.1016/j.cmet.2014.01.009
39. Nicholls SJ, Puri R, Ballantyne CM, Jukema JW, Kastelein JJP, Koenig W, Wright RS, Kallend D, Wijngaard P, Borgman M, et al. Effect of Infusion of High-Density Lipoprotein Mimetic Containing Recombinant Apolipoprotein A-I Milano on Coronary Disease in Patients With an Acute Coronary

743 Syndrome in the MILANO-PILOT Trial: A Randomized Clinical Trial. *JAMA Cardiol*. 2018;3:806-814.
744 doi: 10.1001/jamacardio.2018.2112
745 40. Tardif JC, Gregoire J, L'Allier PL, Ibrahim R, Lesperance J, Heinonen TM, Kouz S, Berry C, Basser R,
746 Lavoie MA, et al. Effects of reconstituted high-density lipoprotein infusions on coronary atherosclerosis: a
747 randomized controlled trial. *JAMA*. 2007;297:1675-1682. doi: 10.1001/jama.297.15.jpc70004
748 41. Keene D, Price C, Shun-Shin MJ, Francis DP. Effect on cardiovascular risk of high density lipoprotein
749 targeted drug treatments niacin, fibrates, and CETP inhibitors: meta-analysis of randomised controlled
750 trials including 117,411 patients. *BMJ*. 2014;349:g4379. doi: 10.1136/bmj.g4379
751 42. Hewing B, Moore KJ, Fisher EA. HDL and cardiovascular risk: time to call the plumber? *Circ Res*.
752 2012;111:1117-1120. doi: 10.1161/CIRCRESAHA.112.280958
753 43. Khera AV, Cuchel M, de la Llera-Moya M, Rodrigues A, Burke MF, Jafri K, French BC, Phillips JA,
754 Mucksavage ML, Wilensky RL, et al. Cholesterol efflux capacity, high-density lipoprotein function, and
755 atherosclerosis. *N Engl J Med*. 2011;364:127-135. doi: 10.1056/NEJMoa1001689
756 44. Josefs T, Basu D, Vaisar T, Arets B, Kanter JE, Huggins LA, Hu Y, Liu J, Clouet-Foraison N, Heinecke
757 JW, et al. Atherosclerosis Regression and Cholesterol Efflux in Hypertriglyceridemic Mice. *Circ Res*.
758 2021;128:690-705. doi: 10.1161/CIRCRESAHA.120.317458
759 45. Rohatgi A, Khera A, Berry JD, Givens EG, Ayers CR, Wedin KE, Neeland IJ, Yuhanna IS, Rader DR, de
760 Lemos JA, et al. HDL cholesterol efflux capacity and incident cardiovascular events. *N Engl J Med*.
761 2014;371:2383-2393. doi: 10.1056/NEJMoa1409065
762 46. Silvain J, Kerneis M, Guerin M, Montalescot G. Modulation of cholesterol efflux capacity in patients with
763 myocardial infarction. *Curr Opin Cardiol*. 2019;34:714-720. doi: 10.1097/HCO.0000000000000677
764 47. Capodanno D, Mehran R, Gibson CM, Angiolillo DJ. CSL112, a reconstituted, infusible, plasma-derived
765 apolipoprotein A-I: safety and tolerability profiles and implications for management in patients with
766 myocardial infarction. *Expert Opin Investig Drugs*. 2018;27:997-1005. doi:
767 10.1080/13543784.2018.1543399
768 48. Ouimet M, Barrett TJ, Fisher EA. HDL and Reverse Cholesterol Transport. *Circ Res*. 2019;124:1505-1518.
769 doi: 10.1161/CIRCRESAHA.119.312617
770 49. Hao Y, Hao S, Andersen-Nissen E, Mauck WM, 3rd, Zheng S, Butler A, Lee MJ, Wilk AJ, Darby C, Zager
771 M, et al. Integrated analysis of multimodal single-cell data. *Cell*. 2021;184:3573-3587 e3529. doi:
772 10.1016/j.cell.2021.04.048
773 50. Franzen O, Gan LM, Bjorkegren JLM. PanglaoDB: a web server for exploration of mouse and human
774 single-cell RNA sequencing data. *Database (Oxford)*. 2019;2019. doi: 10.1093/database/baz046
775 51. Trapnell C, Cacchiarelli D, Grimsby J, Pokharel P, Li S, Morse M, Lennon NJ, Livak KJ, Mikkelsen TS,
776 Rinn JL. The dynamics and regulators of cell fate decisions are revealed by pseudotemporal ordering of
777 single cells. *Nat Biotechnol*. 2014;32:381-386. doi: 10.1038/nbt.2859
778 52. Cao J, Spielmann M, Qiu X, Huang X, Ibrahim DM, Hill AJ, Zhang F, Mundlos S, Christiansen L,
779 Steemers FJ, et al. The single-cell transcriptional landscape of mammalian organogenesis. *Nature*.
780 2019;566:496-502. doi: 10.1038/s41586-019-0969-x
781 53. Zheng R, Zhang Y, Tsuji T, Zhang L, Tseng Y-H, Chen K. MEBOCOST: Metabolic Cell-Cell
782 Communication Modeling by Single Cell Transcriptome. *bioRxiv*. 2022.
783 54. Tao W, Yurdagul A, Jr., Kong N, Li W, Wang X, Doran AC, Feng C, Wang J, Islam MA, Farokhzad OC,
784 et al. siRNA nanoparticles targeting CaMKIIgamma in lesional macrophages improve atherosclerotic
785 plaque stability in mice. *Sci Transl Med*. 2020;12. doi: 10.1126/scitranslmed.aay1063
786 55. Zhu X, Xu Y, Solis LM, Tao W, Wang L, Behrens C, Xu X, Zhao L, Liu D, Wu J, et al. Long-circulating
787 siRNA nanoparticles for validating Prohibitin1-targeted non-small cell lung cancer treatment. *Proc Natl*
788 *Acad Sci U S A*. 2015;112:7779-7784. doi: 10.1073/pnas.1505629112
789 56. Tombor LS, John D, Glaser SF, Luxan G, Forte E, Furtado M, Rosenthal N, Baumgarten N, Schulz MH,
790 Wittig J, et al. Single cell sequencing reveals endothelial plasticity with transient mesenchymal activation
791 after myocardial infarction. *Nat Commun*. 2021;12:681. doi: 10.1038/s41467-021-20905-1
792 57. Dobnikar L, Taylor AL, Chappell J, Oldach P, Harman JL, Oerton E, Dzierzak E, Bennett MR, Spivakov
793 M, Jorgensen HF. Disease-relevant transcriptional signatures identified in individual smooth muscle cells
794 from healthy mouse vessels. *Nat Commun*. 2018;9:4567. doi: 10.1038/s41467-018-06891-x
795 58. Atri C, Guerfali FZ, Laouini D. Role of Human Macrophage Polarization in Inflammation during Infectious
796 Diseases. *Int J Mol Sci*. 2018;19. doi: 10.3390/ijms19061801

797 59. Chen Y, Yang M, Huang W, Chen W, Zhao Y, Schulte ML, Volberding P, Gerbec Z, Zimmermann MT,
798 Zeighami A, et al. Mitochondrial Metabolic Reprogramming by CD36 Signaling Drives Macrophage
799 Inflammatory Responses. *Circ Res*. 2019;125:1087-1102. doi: 10.1161/CIRCRESAHA.119.315833
800 60. Antonov AS, Kolodgie FD, Munn DH, Gerrity RG. Regulation of macrophage foam cell formation by
801 alphaVbeta3 integrin: potential role in human atherosclerosis. *Am J Pathol*. 2004;165:247-258. doi:
802 10.1016/s0002-9440(10)63293-2
803 61. Oppi S, Luscher TF, Stein S. Mouse Models for Atherosclerosis Research-Which Is My Line? *Front*
804 *Cardiovasc Med*. 2019;6:46. doi: 10.3389/fcvm.2019.00046
805 62. Fitzgerald K, White S, Borodovsky A, Bettencourt BR, Strahs A, Clausen V, Wijngaard P, Horton JD,
806 Taubel J, Brooks A, et al. A Highly Durable RNAi Therapeutic Inhibitor of PCSK9. *N Engl J Med*.
807 2017;376:41-51. doi: 10.1056/NEJMoa1609243
808 63. German CA, Shapiro MD. Small Interfering RNA Therapeutic Inclisiran: A New Approach to Targeting
809 PCSK9. *BioDrugs*. 2020;34:1-9. doi: 10.1007/s40259-019-00399-6
810 64. Feingold KR. Cholesterol Lowering Drugs. In: Feingold KR, Anawalt B, Boyce A, Chrousos G, de Herder
811 WW, Dhatariya K, Dungan K, Hershman JM, Hofland J, Kalra S, et al., eds. *Endotext*. South Dartmouth
812 (MA); 2000.
813 65. Ridker PM, Everett BM, Thuren T, MacFadyen JG, Chang WH, Ballantyne C, Fonseca F, Nicolau J,
814 Koenig W, Anker SD, et al. Antiinflammatory Therapy with Canakinumab for Atherosclerotic Disease. *N*
815 *Engl J Med*. 2017;377:1119-1131. doi: 10.1056/NEJMoa1707914
816 66. De Benedetti F, Gattorno M, Anton J, Ben-Chetrit E, Frenkel J, Hoffman HM, Kone-Paut I, Lachmann HJ,
817 Ozen S, Simon A, et al. Canakinumab for the Treatment of Autoinflammatory Recurrent Fever Syndromes.
818 *N Engl J Med*. 2018;378:1908-1919. doi: 10.1056/NEJMoa1706314
819 67. Kojima Y, Weissman IL, Leeper NJ. The Role of Efferocytosis in Atherosclerosis. *Circulation*.
820 2017;135:476-489. doi: 10.1161/CIRCULATIONAHA.116.025684
821 68. Thorp E, Cui D, Schrijvers DM, Kuriakose G, Tabas I. Mertk receptor mutation reduces efferocytosis
822 efficiency and promotes apoptotic cell accumulation and plaque necrosis in atherosclerotic lesions of apoe-
823 /- mice. *Arterioscler Thromb Vasc Biol*. 2008;28:1421-1428. doi: 10.1161/ATVBAHA.108.167197
824 69. Gerlach BD, Ampomah PB, Yurdagul A, Jr., Liu C, Lauring MC, Wang X, Kasikara C, Kong N, Shi J, Tao
825 W, et al. Efferocytosis induces macrophage proliferation to help resolve tissue injury. *Cell Metab*.
826 2021;33:2445-2463 e2448. doi: 10.1016/j.cmet.2021.10.015
827 70. Sergin I, Evans TD, Zhang X, Bhattacharya S, Stokes CJ, Song E, Ali S, Dehestani B, Holloway KB,
828 Micevych PS, et al. Exploiting macrophage autophagy-lysosomal biogenesis as a therapy for
829 atherosclerosis. *Nat Commun*. 2017;8:15750. doi: 10.1038/ncomms15750
830 71. Evans TD, Sergin I, Zhang X, Razani B. Target acquired: Selective autophagy in cardiometabolic disease.
831 *Sci Signal*. 2017;10. doi: 10.1126/scisignal.aag2298
832 72. Le Guezennec X, Brichkina A, Huang YF, Kostromina E, Han W, Bulavin DV. Wip1-dependent regulation
833 of autophagy, obesity, and atherosclerosis. *Cell Metab*. 2012;16:68-80. doi: 10.1016/j.cmet.2012.06.003
834 73. Ouimet M, Franklin V, Mak E, Liao X, Tabas I, Marcel YL. Autophagy regulates cholesterol efflux from
835 macrophage foam cells via lysosomal acid lipase. *Cell Metab*. 2011;13:655-667. doi:
836 10.1016/j.cmet.2011.03.023
837 74. Razani B, Feng C, Coleman T, Emanuel R, Wen H, Hwang S, Ting JP, Virgin HW, Kastan MB,
838 Semenkovich CF. Autophagy links inflammasomes to atherosclerotic progression. *Cell Metab*.
839 2012;15:534-544. doi: 10.1016/j.cmet.2012.02.011
840 75. Butcher MJ, Herre M, Ley K, Galkina E. Flow cytometry analysis of immune cells within murine aortas. *J*
841 *Vis Exp*. 2011. doi: 10.3791/2848
842 76. Purcell-Huynh DA, Farese RV, Jr., Johnson DF, Flynn LM, Pierotti V, Newland DL, Linton MF, Sanan
843 DA, Young SG. Transgenic mice expressing high levels of human apolipoprotein B develop severe
844 atherosclerotic lesions in response to a high-fat diet. *J Clin Invest*. 1995;95:2246-2257. doi:
845 10.1172/JCI117915
846 77. Tao H, Yancey PG, Blakemore JL, Zhang Y, Ding L, Jerome WG, Brown JD, Vickers KC, Linton MF.
847 Macrophage SR-BI modulates autophagy via VPS34 complex and PPARalpha transcription of Tfeb in
848 atherosclerosis. *J Clin Invest*. 2021;131. doi: 10.1172/JCI94229
849 78. Van Eck M, Bos IS, Hildebrand RB, Van Rij BT, Van Berkel TJ. Dual role for scavenger receptor class B,
850 type I on bone marrow-derived cells in atherosclerotic lesion development. *Am J Pathol*. 2004;165:785-
851 794. doi: 10.1016/S0002-9440(10)63341-X

79. Csikos G, Lippai M, Lukacsovich T, Juhasz G, Henn L, Erdelyi M, Maroy P, Sass M. A novel role for the Drosophila epsin (lqf): involvement in autophagy. *Autophagy*. 2009;5:636-648. doi: 10.4161/auto.5.5.8168
80. Tarling EJ, Edwards PA. ATP binding cassette transporter G1 (ABCG1) is an intracellular sterol transporter. *Proc Natl Acad Sci U S A*. 2011;108:19719-19724. doi: 10.1073/pnas.1113021108
81. Wang N, Ranalletta M, Matsuura F, Peng F, Tall AR. LXR-induced redistribution of ABCG1 to plasma membrane in macrophages enhances cholesterol mass efflux to HDL. *Arterioscler Thromb Vasc Biol*. 2006;26:1310-1316. doi: 10.1161/01.ATV.0000218998.75963.02
82. Cui K, Podolnikova NP, Bailey W, Szmuc E, Podrez EA, Byzova TV, Yakubenko VP. Inhibition of integrin alphaDbeta2-mediated macrophage adhesion to end product of docosahexaenoic acid (DHA) oxidation prevents macrophage accumulation during inflammation. *J Biol Chem*. 2019;294:14370-14382. doi: 10.1074/jbc.RA119.009590
83. Dobin A, Davis CA, Schlesinger F, Drenkow J, Zaleski C, Jha S, Batut P, Chaisson M, Gingeras TR. STAR: ultrafast universal RNA-seq aligner. *Bioinformatics*. 2013;29:15-21. doi: 10.1093/bioinformatics/bts635
84. Kim D, Pertea G, Trapnell C, Pimentel H, Kelley R, Salzberg SL. TopHat2: accurate alignment of transcriptomes in the presence of insertions, deletions and gene fusions. *Genome Biol*. 2013;14:R36. doi: 10.1186/gb-2013-14-4-r36
85. Anders S, Pyl PT, Huber W. HTSeq--a Python framework to work with high-throughput sequencing data. *Bioinformatics*. 2015;31:166-169. doi: 10.1093/bioinformatics/btu638
86. Love MI, Huber W, Anders S. Moderated estimation of fold change and dispersion for RNA-seq data with DESeq2. *Genome Biol*. 2014;15:550. doi: 10.1186/s13059-014-0550-8
87. Johnson WE, Li C, Rabinovic A. Adjusting batch effects in microarray expression data using empirical Bayes methods. *Biostatistics*. 2007;8:118-127. doi: 10.1093/biostatistics/kxj037
88. Yu G, Wang LG, Han Y, He QY. clusterProfiler: an R package for comparing biological themes among gene clusters. *OMICS*. 2012;16:284-287. doi: 10.1089/omi.2011.0118
89. Edgar R, Domrachev M, Lash AE. Gene Expression Omnibus: NCBI gene expression and hybridization array data repository. *Nucleic Acids Res*. 2002;30:207-210. doi: 10.1093/nar/30.1.207
90. Chen H, Boutros PC. VennDiagram: a package for the generation of highly-customizable Venn and Euler diagrams in R. *BMC Bioinformatics*. 2011;12:35. doi: 10.1186/1471-2105-12-35
91. Spangenburg EE, Pratt SJP, Wohlers LM, Lovering RM. Use of BODIPY (493/503) to visualize intramuscular lipid droplets in skeletal muscle. *J Biomed Biotechnol*. 2011;2011:598358. doi: 10.1155/2011/598358
92. Robinet P, Wang Z, Hazen SL, Smith JD. A simple and sensitive enzymatic method for cholesterol quantification in macrophages and foam cells. *J Lipid Res*. 2010;51:3364-3369. doi: 10.1194/jlr.D007336
93. Sankaranarayanan S, Kellner-Weibel G, de la Llera-Moya M, Phillips MC, Asztalos BF, Bittman R, Rothblat GH. A sensitive assay for ABCA1-mediated cholesterol efflux using BODIPY-cholesterol. *J Lipid Res*. 2011;52:2332-2340. doi: 10.1194/jlr.D018051
94. Escola-Gil JC, Lee-Rueckert M, Santos D, Cedo L, Blanco-Vaca F, Julve J. Quantification of In Vitro Macrophage Cholesterol Efflux and In Vivo Macrophage-Specific Reverse Cholesterol Transport. *Methods Mol Biol*. 2015;1339:211-233. doi: 10.1007/978-1-4939-2929-0_15

FIGURES AND LEGENDS

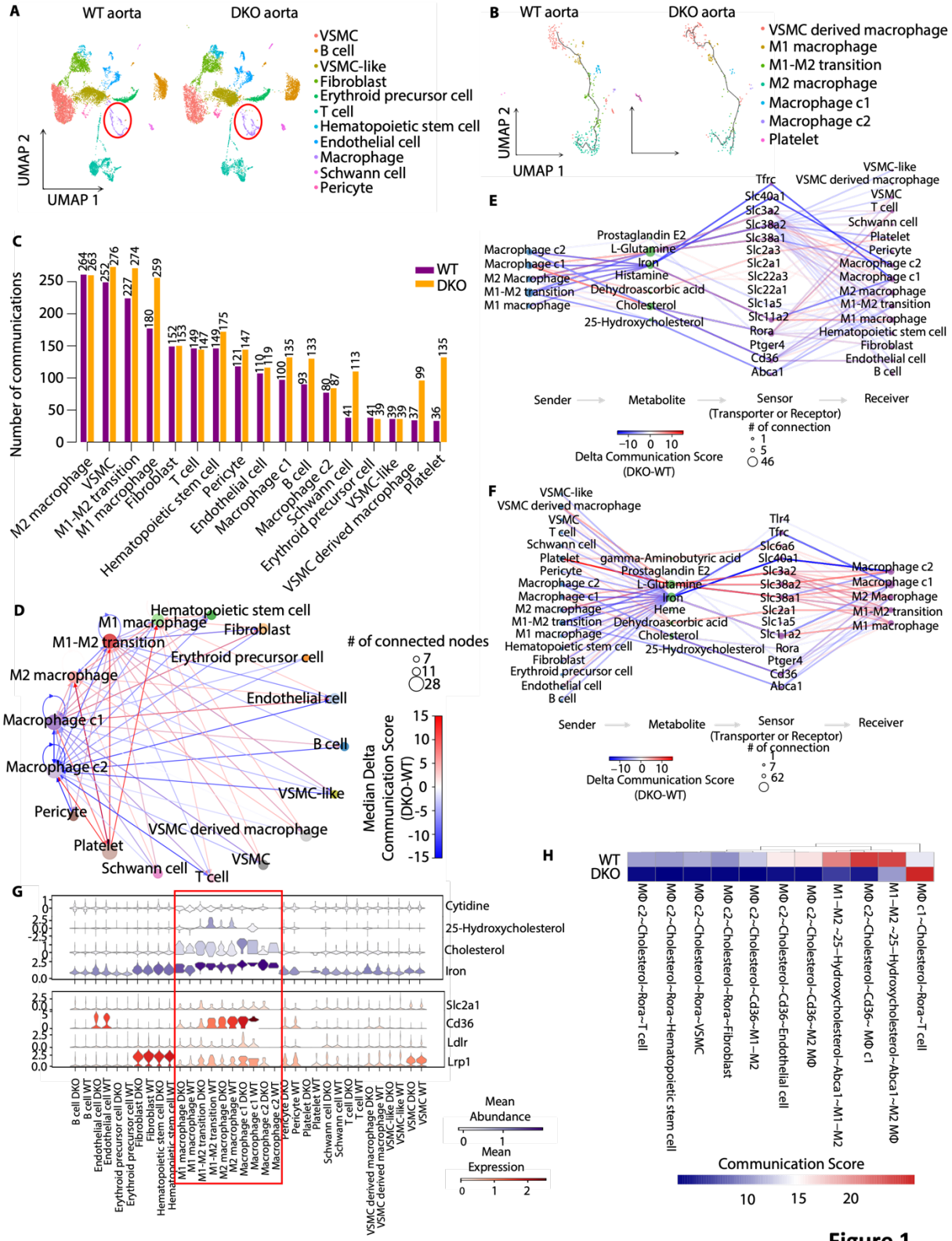

Figure 1

896 **Figure 1. scRNA-seq data revealed down-regulation of cholesterol-related cell-cell**
897 **communications mediated by metabolites and their sensor proteins in macrophage**
898 **subpopulations in DKO aorta compared to WT.** (**A**) UMAP plot of cell clusters in WT and
899 DKO aorta. Macrophage populations are indicated in the red circle. (**B**) UMAP of subclusters of
900 macrophage populations in (A). Trajectory inferred by Monocle3 was displayed. (**C**) A barplot
901 showing the number of communication events in cell groups in WT and DKO. (**D**) A circle plot
902 showing the differential communications between cell groups in DKO compared to WT. The
903 arrows indicate directions of communication from sender cells to receiver cells. The size of nodes
904 positively correlates with the number of connected nodes. Line colors indicate the difference in
905 communication scores of DKO compared to WT. (**E-F**) A flow plot of communications
906 comprising senders, metabolites, sensors, and receivers from macrophage subpopulations to all the
907 cell types (E); and from all cell types to macrophages (F). (**G**) Violin plots of the abundance of
908 representative metabolites and sensors across cell types in WT and DKO. Metabolite abundance
909 (upper), sensor abundance (below). (**H**) A heatmap showing the most variable communications
910 related to cholesterol metabolism in macrophages in the comparison of WT and DKO aorta.

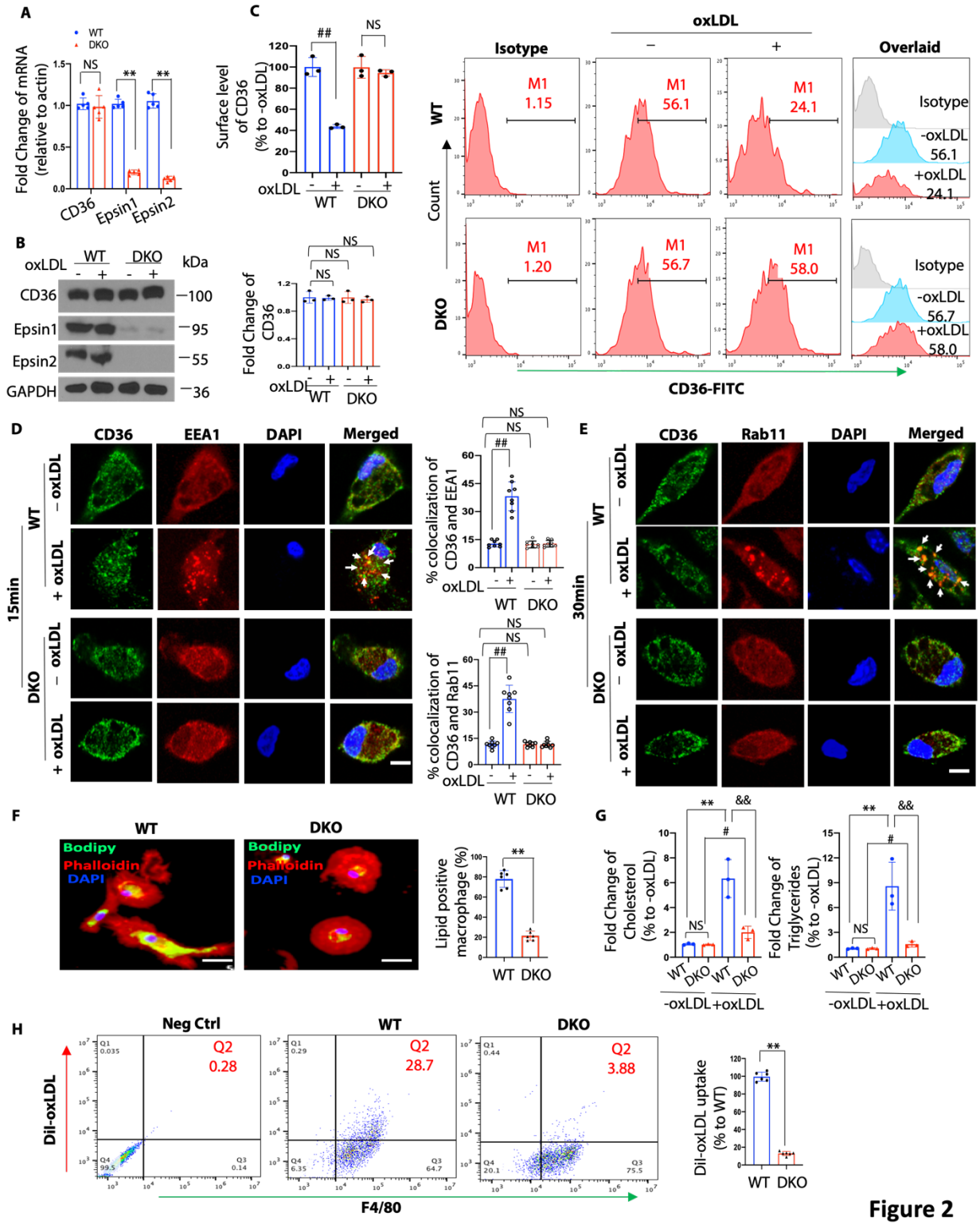
A
WT
DKO
Fold Change of mRNA (relative to actin)
NS
**
**
CD36
Epsin1
Epsin2
B
oxLDL
WT
DKO
kDa
CD36
Epsin1
Epsin2
GAPDH
100
95
55
36
C
##
NS
Surface level of CD36 (% to -oxLDL)
oxLDL
WT
DKO
NS
NS
NS
Fold Change of CD36
oxLDL
WT
DKO
oxLDL
Isotype
Overlaid
WT
DKO
Count
M1 1.15
M1 56.1
M1 24.1
M1 1.20
M1 56.7
M1 58.0
Isotype
-oxLDL 56.1
+oxLDL 24.1
Isotype
-oxLDL 56.7
+oxLDL 58.0
CD36-FITC
D
CD36
EEA1
DAPI
Merged
15min
WT
DKO
– oxLDL
+ oxLDL
% colocalization of CD36 and EEA1
% colocalization of CD36 and Rab11
NS
NS
##
oxLDL
WT
DKO
E
CD36
Rab11
DAPI
Merged
30min
WT
DKO
– oxLDL
+ oxLDL
F
WT
DKO
Bodipy
Phalloidin
DAPI
Lipid positive macrophage (%)
**
WT
DKO
G
Fold Change of Cholesterol (% to -oxLDL)
Fold Change of Triglycerides (% to -oxLDL)
**
&&
#
NS
WT
DKO
-oxLDL
+oxLDL
H
Neg Ctrl
WT
DKO
Dil-oxLDL
F4/80
Q2 0.28
Q2 28.7
Q2 3.88
Dil-oxLDL uptake (% to WT)
**
WT
DKO

Figure 2

913 **Figure 2. Epsin facilitates CD36-mediated lipid uptake by promoting CD36 endocytosis and**
914 **recycling.** (**A-C**) Bone marrow derived macrophages (BMDM) or thioglycolate induced
915 peritoneal macrophages from WT (n=5) and DKO (n=5) mice were incubated in lipid-deficient
916 medium for 24h and treated with or without 100μg/mL oxLDL for 1h at 37^0C. qRT-PCR analysis
917 of CD36 expression (A), western blot (WB) analysis for total protein level of CD36 (B) and flow
918 cytometry for surface level of CD36 (C). NS, no significant difference; **WT vs DKO group,
919 P<0.01; ##-oxLDL vs +oxLDL group, P<0.01. (**D-E**) Elicited WT and DKO macrophages were
920 incubated in lipid-deficient medium for 24h and treated with or without 100μg/mL oxLDL for
921 15min (D) or 30min (E) at 37^0C. Macrophages were co-stained with CD36 (green), the early
922 endosome marker EEA1 (red) or the recycling endosome marker Rab11 (Red) and DAPI (bule),
923 and imaged using confocal microscope. White arrows indicate the endocytic vesicles, scale
924 bar=5μm, ##-oxLDL vs +oxLDL group (n=8), P<0.01. (**F**) BODIPY staining of peritoneal
925 macrophages pre-incubated with 25μg/mL oxLDL for 24h in lipid-deficient medium, **WT vs
926 DKO group (n=6), P<0.01, scale bar=10μm. (**G**) Cholesterol and triglycerides levels in WT and
927 DKO macrophages treated with 25μg/mL oxLDL for 24h in lipid-deficient medium (n=3). **-
928 oxLDL (WT) vs +oxLDL (WT), P<0.01; #-oxLDL (DKO) vs +oxLDL (DKO), P<0.05; && +oxLDL
929 (WT) vs +oxLDL (DKO), P<0.01. (**H**) Macrophages isolated from WT and DKO mice were
930 incubated in lipid-deficient medium for 24h followed by the treatment with DiI-oxLDL for 2h at
931 37^0C to assess the lipoprotein uptake by flow cytometry, **WT vs DKO group (n=6), P<0.01.
932 Data from A-H are presented as mean ± SD and were analyzed using either unpaired Student's t-
933 test (two groups) or one-way ANOVA (multiple comparisons).

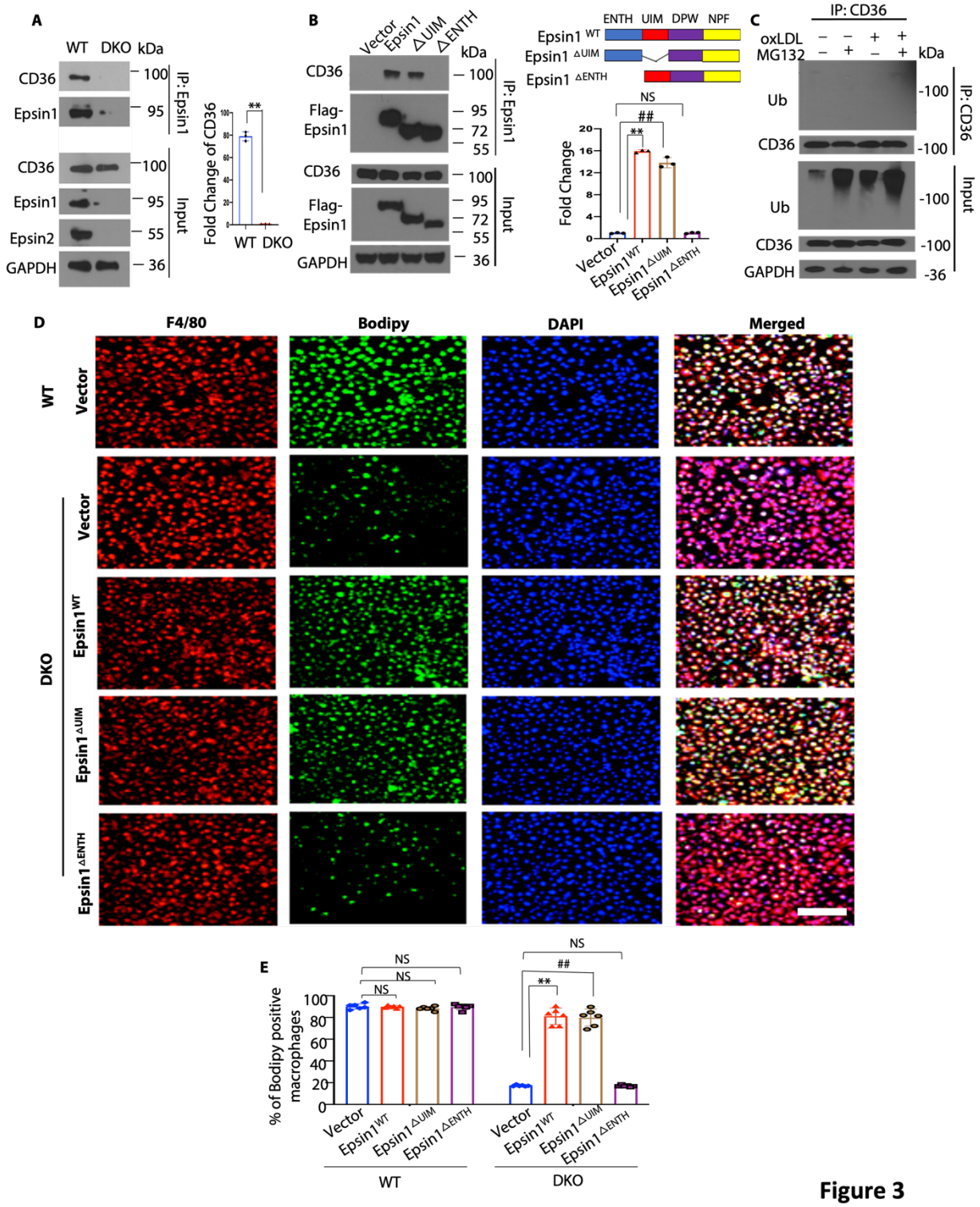

Figure 3

934

935

936 **Figure 3. Epsin interacts with CD36 via Epsin-ENTH domain which is critical for CD36-**
937 **mediated lipid uptake and foam cell formation.** (**A**) BMDM or peritoneal macrophages isolated
938 from WT and DKO mice were incubated in lipid-deficient medium for 24h followed by the
939 treatment with 100μg/mL oxLDL for 1h, IP and WB analysis of Epsin1 and CD36 (n=3, **WT vs
940 DKO, P<0.01). (**B**) CD36 plasmids and full length (FLAG-Epsin1^{WT}) or domain-deletion
941 constructs (FLAG-Epsin1$^{\Delta ENTH}$ or FLAG-Epsin1$^{\Delta UIM}$) in the pcDNA3 vector were transfected into
942 HEK 293T cells for 48 h and then treated with 100μg/mL oxLDL for 1h, followed by
943 immunoprecipitation (IP) and WB analysis using antibodies against FLAG tags and CD36 (n=3,
944 **Epsin1^{WT} vs vector group, P<0.01; $^{\#\#}$Epsin1$^{\Delta UIM}$ vs vector group, P<0.01). (**C**) Peritoneal
945 macrophages isolated from WT mice were incubated in lipid-deficient medium for 24h followed
946 by treatment with 5 μM MG132 for 3h. Cells were subsequently treated with 100 μg/mL oxLDL
947 for 1h followed by IP and WB for ubiquitin and CD36. (**D**) FLAG-Epsin1^{WT}, FLAG-Epsin1$^{\Delta ENTH}$,
948 and FLAG-Epsin1$^{\Delta UIM}$ constructs were transfected into DKO macrophages for 48 h and treated
949 with 100μg/mL oxLDL for 1 h, followed by staining with F4/80 (red), BODIPY (green) and DAPI
950 (blue). Scale bar= 200μm. (**E**) Statistics for (D and Figure S6), n=6, **Epsin1 ^{WT} vs vector group,
951 P<0.01; $^{\#\#}$Epsin1$^{\Delta UIM}$ vs vector group, P<0.01. Data from A-D are presented as mean ± SD and
952 were analyzed using either unpaired Student's t-test (two groups) or one-way ANOVA (multiple
953 comparisons).

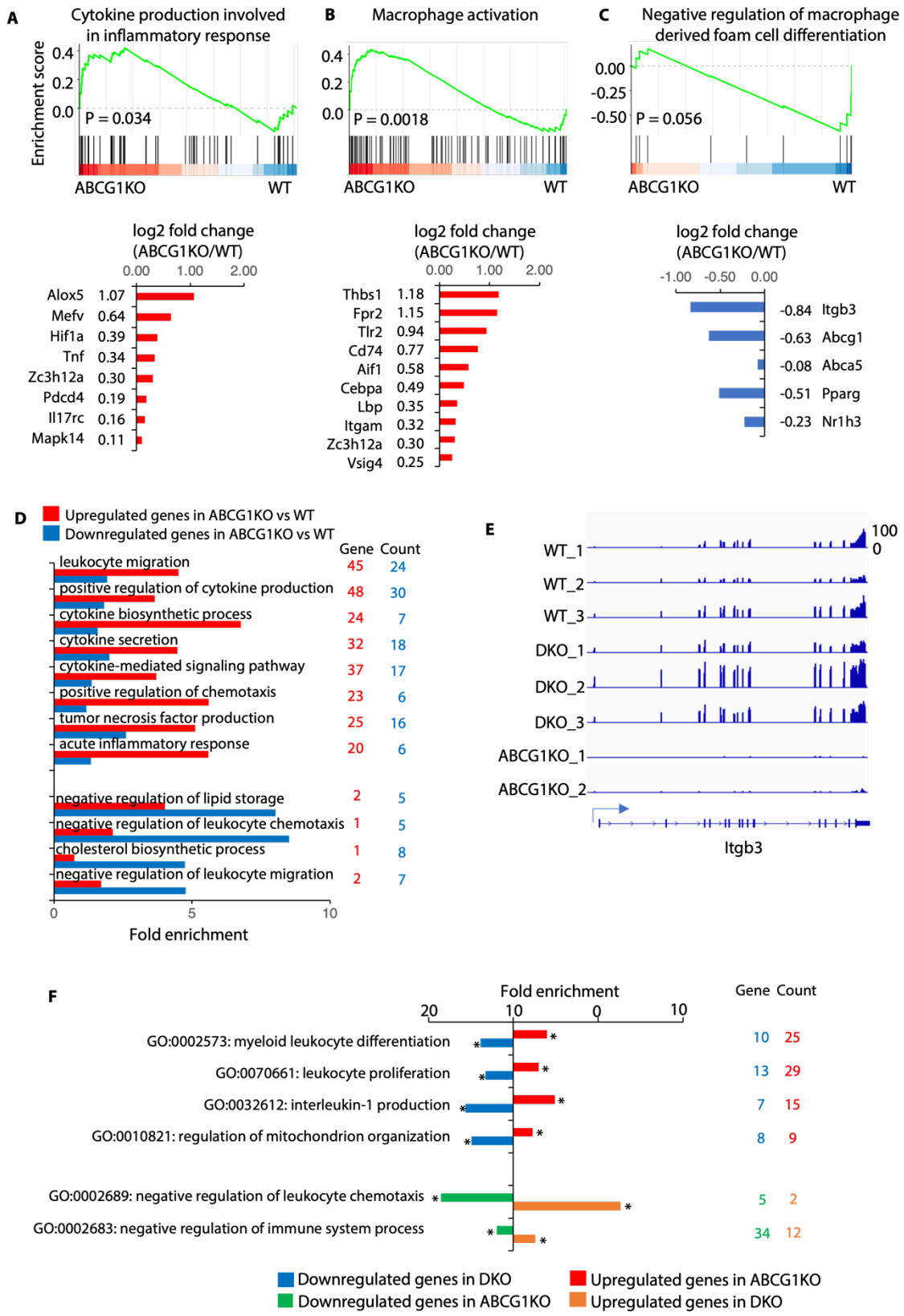
A
Cytokine production involved in inflammatory response
Enrichment score
P = 0.034
ABCG1KO
WT
B
Macrophage activation
P = 0.0018
C
Negative regulation of macrophage derived foam cell differentiation
P = 0.056
log2 fold change (ABCG1KO/WT)
Alox5 1.07
Mefv 0.64
Hif1a 0.39
Tnf 0.34
Zc3h12a 0.30
Pdcd4 0.19
Il17rc 0.16
Mapk14 0.11
Thbs1 1.18
Fpr2 1.15
Tlr2 0.94
Cd74 0.77
Aif1 0.58
Cebpa 0.49
Lbp 0.35
Itgam 0.32
Zc3h12a 0.30
Vsig4 0.25
-0.84 Itgb3
-0.63 Abcg1
-0.08 Abca5
-0.51 Pparg
-0.23 Nr1h3
D
Upregulated genes in ABCG1KO vs WT
Downregulated genes in ABCG1KO vs WT
Gene Count
leukocyte migration 45 24
positive regulation of cytokine production 48 30
cytokine biosynthetic process 24 7
cytokine secretion 32 18
cytokine-mediated signaling pathway 37 17
positive regulation of chemotaxis 23 6
tumor necrosis factor production 25 16
acute inflammatory response 20 6
negative regulation of lipid storage 2 5
negative regulation of leukocyte chemotaxis 1 5
cholesterol biosynthetic process 1 8
negative regulation of leukocyte migration 2 7
Fold enrichment
E
WT_1
WT_2
WT_3
DKO_1
DKO_2
DKO_3
ABCG1KO_1
ABCG1KO_2
Itgb3
F
Fold enrichment
Gene Count
GO:0002573: myeloid leukocyte differentiation 10 25
GO:0070661: leukocyte proliferation 13 29
GO:0032612: interleukin-1 production 7 15
GO:0010821: regulation of mitochondrion organization 8 9
GO:0002689: negative regulation of leukocyte chemotaxis 5 2
GO:0002683: negative regulation of immune system process 34 12
Downregulated genes in DKO
Downregulated genes in ABCG1KO
Upregulated genes in ABCG1KO
Upregulated genes in DKO

Figure 4

954

955 **Figure 4. RNA-seq analyses of WT, DKO and ABCG1 knockout (ABCG1KO) macrophages**
956 **indicate inverse regulation of lipid metabolism and inflammatory response.** (**A-C**) The Gene
957 Set Enrichment Analysis (GSEA) (top panels) indicates the tendency of individual pathways to be
958 up or down regulated in ABCG1KO macrophages compared to wild type. Genes associated with
959 cytokine production involved in the inflammatory response (A), macrophage activation (B), and
960 negatively regulating macrophage derived foam cell differentiation (C) are analyzed. The Barplots
961 (bottom panels) showing log2 fold changes of expression of altered genes. (**D**) GO enrichment
962 analysis for up- and down- regulated genes in ABCG1KO relative to WT. (**E**) Genome browser
963 tracks to show expression of Itgb3 in individual samples. (**F**) The GO enrichment analysis revealed
964 pathways reversely regulated in ABCG1 knock out and Epsin deficient macrophages, compared
965 to wild type. *P<0.05.

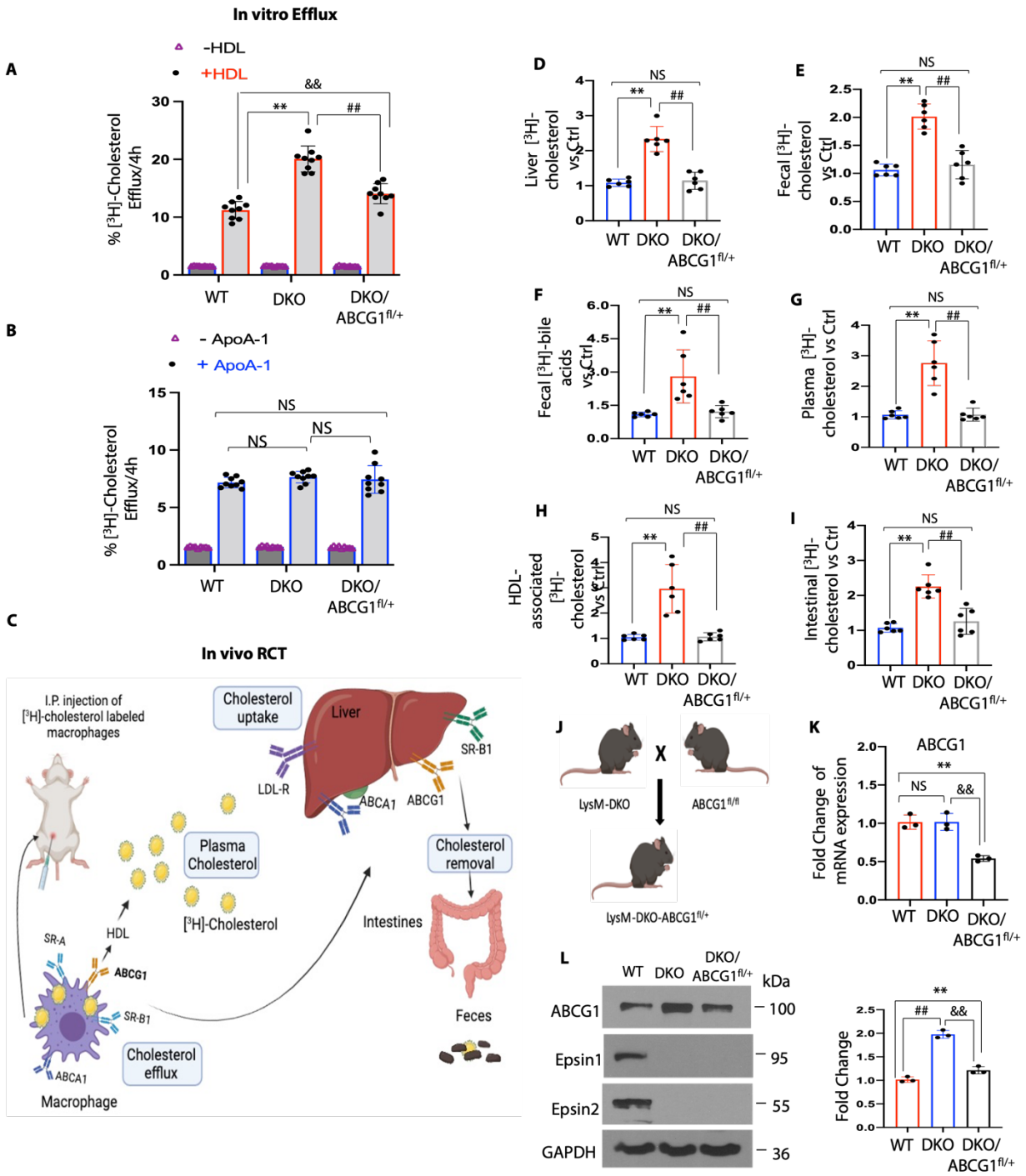

Figure 5

966

967

968 **Figure 5. Epsins deficiency in macrophages shows increased cholesterol efflux *in vitro* and**
969 **reverse cholesterol transport (RCT) *in vivo*.** (**A-B**) Peritoneal macrophages were isolated from
970 WT, DKO) and DKO/ABCG1$^{fl/+}$ mice. *In vitro* [^{3}H]-cholesterol labeled WT, DKO or
971 DKO/ABCG1$^{fl/+}$ macrophages were incubated in the presence or absence of HDL (25μg/mL) and
972 ApoA-1 (10μg/mL) in the presence of 3μmol/L LXR agonist T0901317 (n=9). **WT vs DKO,
973 P<0.01; $^{\#\#}$DKO vs DKO/ABCG1$^{fl/+}$, P<0.01; $^{\&\&}$WT vs DKO/ABCG1$^{fl/+}$, P<0.01. (**C**) Schematic of
974 [^{3}H]-cholesterol loaded macrophage-RCT pathway. WT, DKO or DKO/ABCG1$^{fl/+}$ macrophages
975 were treated with 4μCi/mL [^{3}H]-cholesterol and 50μg/mL ac-LDL for 48h followed by the
976 injection of radiolabeled foam cells to C57BL/6/WT mice. After 48h, blood, liver and feces were
977 collected and measured using a scintillation counter. (**D-I**) Distribution of [^{3}H]-radioactivity counts
978 in serum, HDL, liver feces and intestinal contents were determined by scintillation counter (n=6).
979 **WT vs DKO, P<0.01; $^{\#\#}$DKO vs DKO/ABCG1$^{fl/+}$, P<0.01. (**J**) LysM-DKO mice were crossed
980 with ABCG1$^{fl/fl}$ mice to generate LysM-DKO-ABCG1$^{fl/+}$ mice. (**K-L**) Peritoneal macrophages
981 isolated from WT, LysM-DKO and LysM-DKO/ABCG1$^{fl/+}$ mice (n=6) were analyzed by qRT-
982 PCR (K) and WB (L) (n≥3). **WT vs DKO/ABCG1$^{fl/+}$ group, P<0.01; $^{\#\#}$WT vs DKO group,
983 P<0.01; $^{\&\&}$DKO vs DKO/ABCG1$^{fl/+}$ group, P<0.01. Data from A-L are presented as mean ± SD
984 and were analyzed using one-way ANOVA (multiple comparisons).

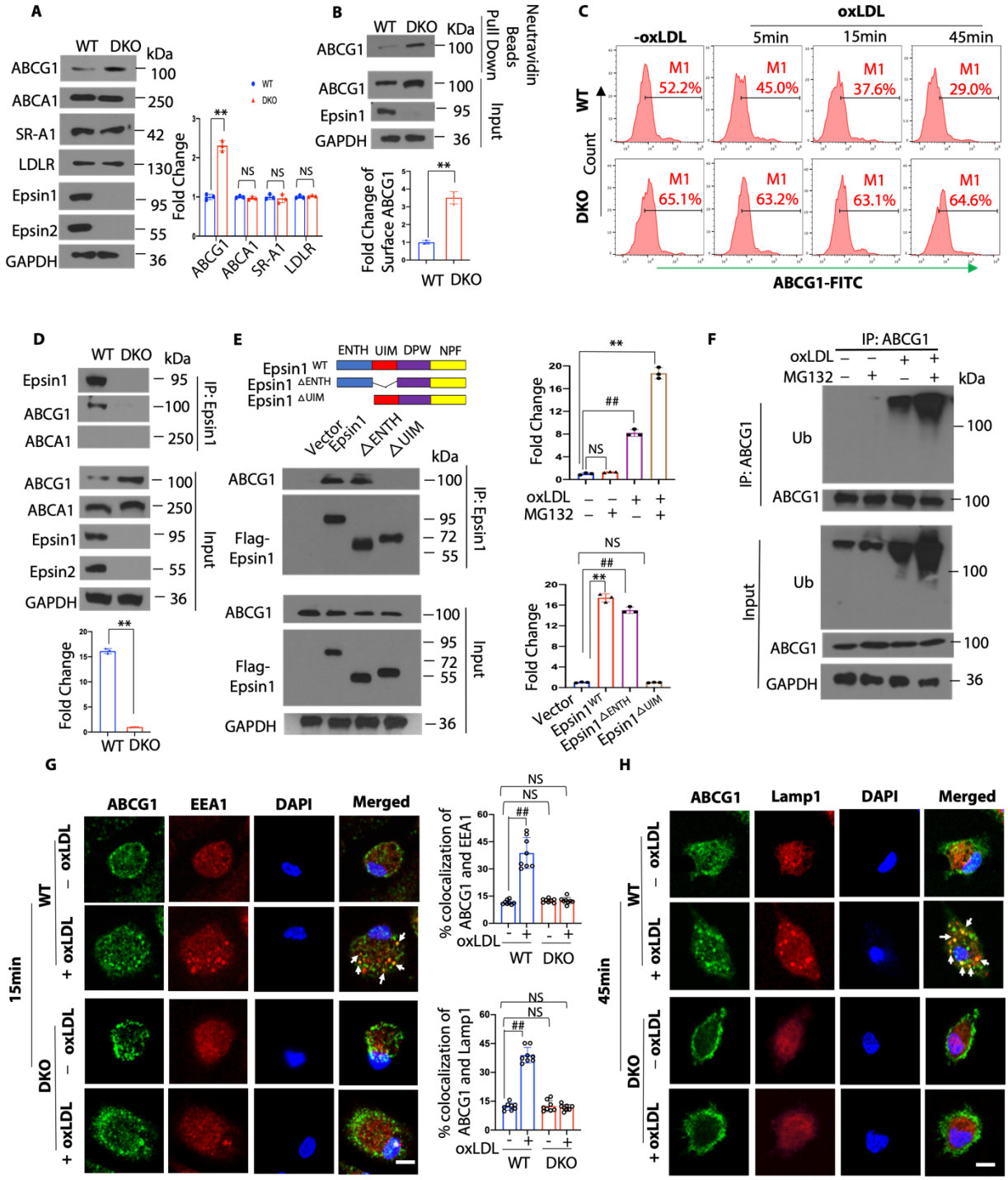

Figure 6

Figure 6. Epsins bind to ABCG1 and facilitate the internalization and degradation of ABCG1 via lysosomes. (**A**) Macrophages from WT (n=3) and DKO (n=3) mice were lysed for WB analysis

988 (**WT vs DKO, P<0.01). (**B**) Macrophages from WT (n=3) and DKO (n=3) mice were pretreated
989 with a liver X receptor (LXR) activator and followed by a cell surface biotinylation assay to
990 evaluate the cell surface ABCG1 levels (**WT vs DKO, P<0.01). (**C**) LXR activated WT and
991 DKO macrophages were incubated in lipid-deficient medium for 24h and treated with or without
992 100μg/mL oxLDL for 5, 15 and 45 min followed by staining with anti-ABCG1 and analyzed by
993 flow cytometry. (**D**) LXR pretreated macrophages isolated from WT and DKO mice were treated
994 with 100μg/mL oxLDL for 1h followed by IP and WB for Epsin1 and ABCG1 or ABCA1 (n=3,
995 **WT vs DKO, P<0.01). (**E**) ABCG1 plasmids and full length (FLAG-Epsin1^{WT}) or domain-
996 deletion constructs (FLAG-Epsin1$^{\Delta ENTH}$ or FLAG-Epsin1$^{\Delta UIM}$) in the pcDNA3 vector were
997 transfected into HEK 293T cells for 24 h in the presence of LXR agonist. Cells were then treated
998 with 100μg/mL oxLDL for 1h, followed by IP and WB analysis using antibodies against FLAG
999 tags and ABCG1 (n=3, **Epsin1 ^{WT} vs vector group, P<0.01; $^{\#\#}$ Epsin1$^{\Delta ENTH}$ vs vector group,
1000 P<0.01). (**F**) Peritoneal macrophages isolated from WT mice were cultured in serum-free media
1001 for 24h followed by treatment with 5 μM MG132 for 3h. Cells were then treated with 100μg/mL
1002 oxLDL for 1h followed by IP and WB for ubiquitin and ABCG1. (**G-H**) WT and DKO
1003 macrophages were incubated in lipid-deficient medium for 24h followed by incubation with or
1004 without 100μg/mL oxLDL for 15min (G) or 45min (H) at 37^{0}C. Macrophages were stained with
1005 ABCG1 (green), early endosome marker EEA1 (red) or lysosome marker Lamp1 (red) and DAPI
1006 (blue), then assessed by confocal microscopy. White arrows indicate the endocytic vesicles, scale
1007 bar=5μm, $^{\#\#}$-oxLDL vs +oxLDL group (n=8), P<0.01. Data from A-H are presented as mean ± SD
1008 and were analyzed using either an unpaired Student's t-test (two groups) or one-way ANOVA
1009 (multiple comparisons).
1010

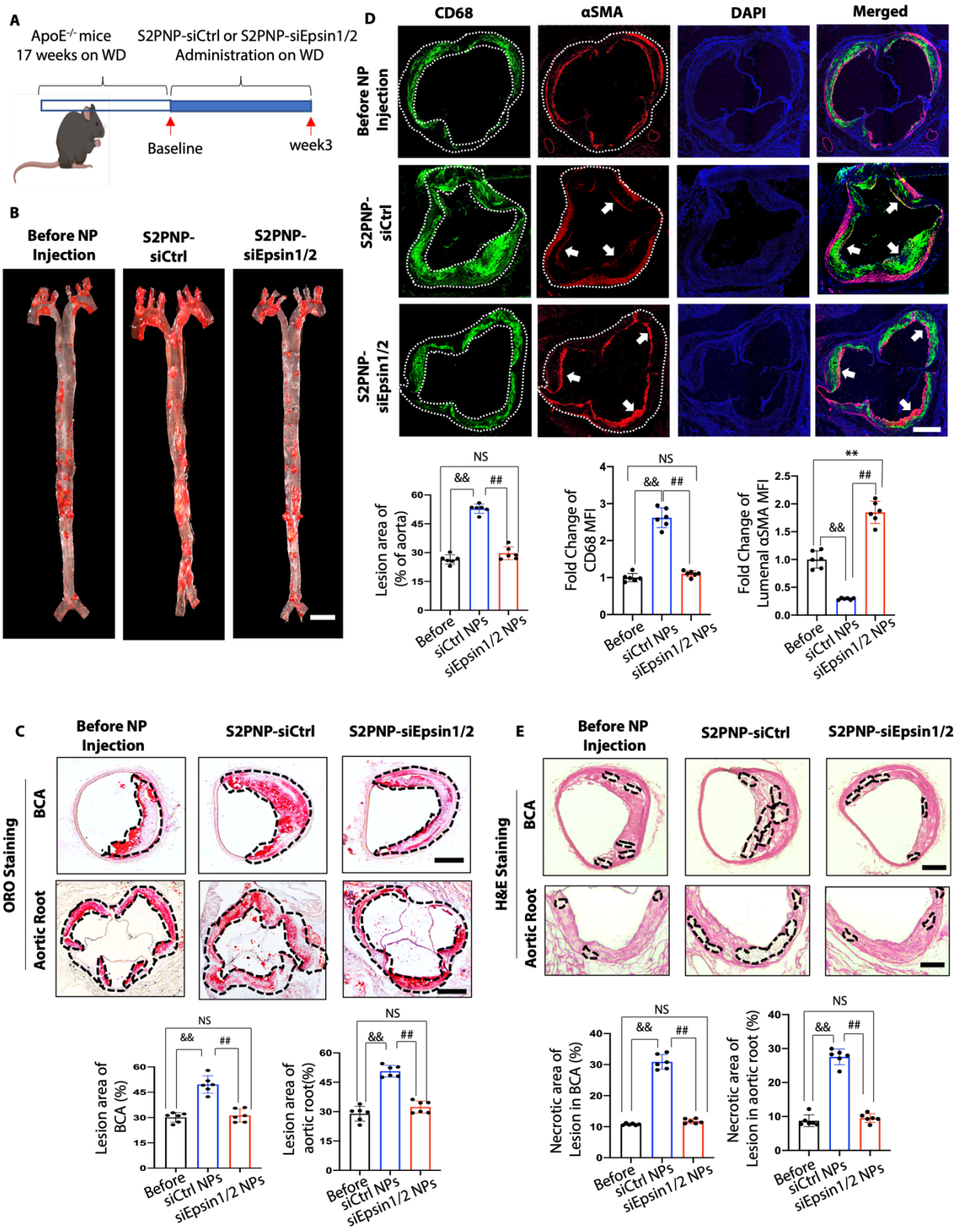

Figure 7

1011

1012 **Figure 7. S2PNP-siEpsin1/2 delivery inhibits atheroma progression, decreases necrotic core**
1013 **content, and increases smooth muscle cell content in advanced stage of atherosclerosis.** (**A**)
1014 ApoE$^{-/-}$ mice fed a Western Diet (WD) for 17 weeks followed by treatment of S2PNP-siCtrl or
1015 S2PNP-siEpsin1/2 for 3 weeks (2 doses per week). (**B**) *En face* ORO staining of aortas from
1016 baseline, control siRNA NP-treated ApoE$^{-/-}$ or Epsin1/2 siRNA NP treated ApoE$^{-/-}$ mice fed a WD.
1017 lesion areas were analyzed with NIH ImageJ, scale bar=5mm. (**C**) ORO staining of
1018 brachiocephalic artery (BCA) and aortic root sections of above three groups. Lesional area (black
1019 dash line outlined) were analyzed by NIH ImageJ. (**D**) Aortic roots from S2PNP-siCtrl-treated
1020 ApoE$^{-/-}$ or S2PNP-siEpsin1/2 treated ApoE$^{-/-}$ mice were stained with the macrophage marker CD68
1021 (dashed white line outlined) and αSMA (white arrow). (**E**) H&E staining of BCA and aortic root
1022 sections of the above three groups. Necrotic areas (black dash line outlined) were analyzed by NIH
1023 ImageJ. Data from B-E (n=6) are presented as mean ± SD and were analyzed using one-way
1024 ANOVA. $^{\&\&}$S2PNP-siCtrl vs baseline, P<0.01; $^{\#\#}$S2PNP-siCtrl vs S2PNP-siEpsin1/2 group,
1025 P<0.01, scale bar: B=5mm; C, D, E=500μm.

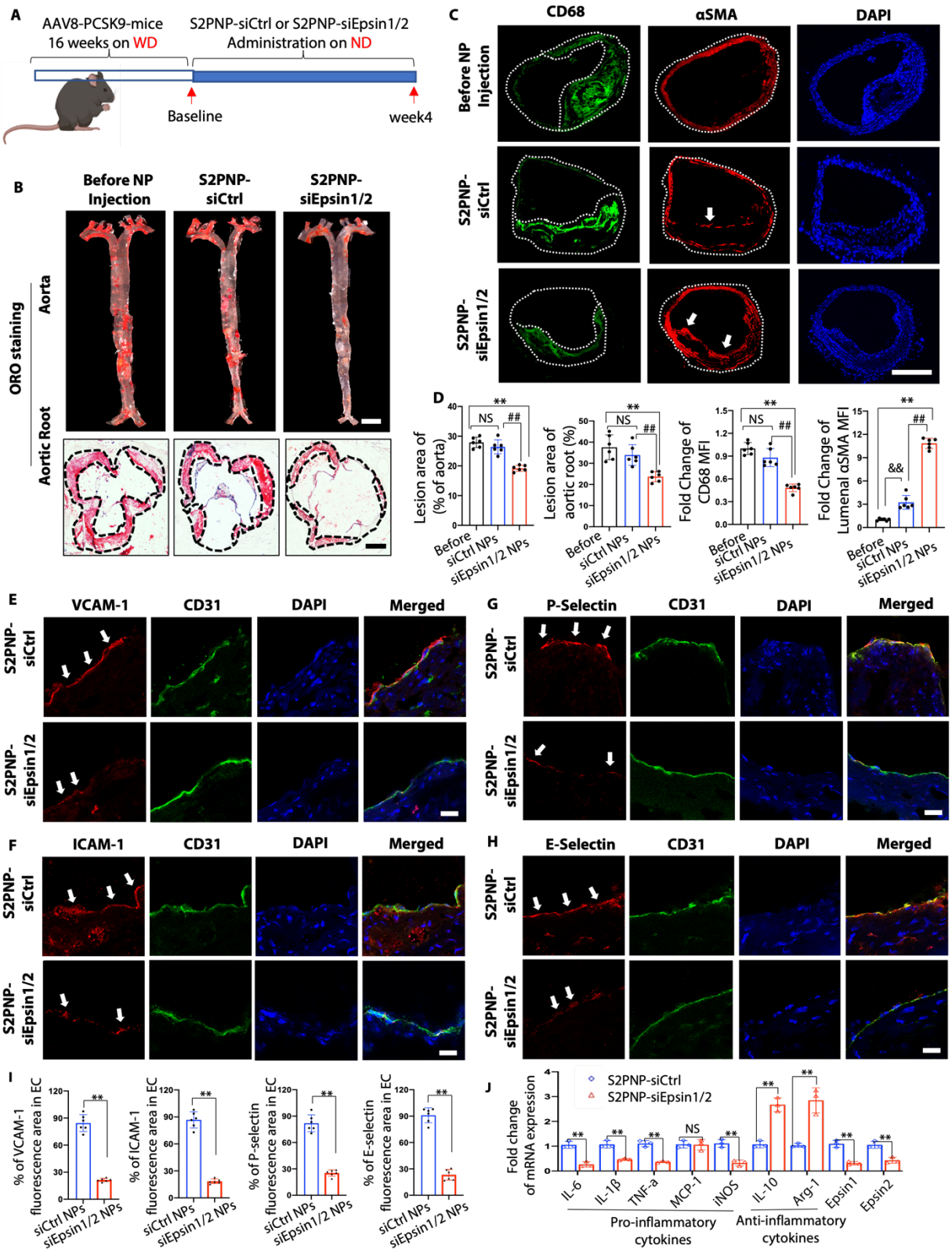

Figure 8

1026

1027 **Figure 8. S2PNP-siEpsin1/2 promotes the resolution of atheroma, reduces inflammation, and**
1028 **stabilizes atherosclerotic plaques.** (**A**) C57BL/6 WT mice were injected twice with PCSK9-
1029 AAV8 (D377Y) virus and fed a WD for 16 weeks and followed by normal diet feeding with the
1030 treatment of S2PNP-siCtrl or S2PNP-siEpsin1/2 for 4 weeks (2 doses per week). (**B**) *En face* ORO
1031 staining of aortas from above mice. Lesion area was analyzed using NIH ImageJ, scale bar=5mm.
1032 (**C**) Immunostaining of CD68 (green) and αSMA (red) in the above groups. White arrows indicate
1033 the luminal αSMA. For (B) and (C), n=6, scale bar: B (aorta)=5mm, B (aortic root)=500μm,
1034 C=500μm. (**D**) Statistics for ORO staining (B) and IF staining (C), **S2PNP-siEpsin1/2 vs
1035 baseline, P<0.01, ##S2PNP-siCtrl vs S2PNP-siEpsin1/2 group, P<0.01. (**E-H**) Co-staining of CD31
1036 (endothelial cell marker, green) with vascular cell adhesion molecule-1 (VCAM-1, red, E),
1037 intercellular adhesion molecule-1 (ICAM-1, red, F), P-selectin (red, G) or E-selectin (red, H) and
1038 DAPI on the luminal surface of aortic root sections. White arrows indicate CD31/ICAM-1,
1039 CD31/VCAM-1, CD31/E-selectin or CD31/P-selectin colocalization. Scale bars=20μm. (**I**)
1040 Statistical analysis of E-H, n=6, **S2PNP-siCtrl vs S2PNP-siEpsin1/2 group, P<0.01. (**J**) Isolated
1041 macrophages from PCSK9-mice were treated with S2PNP-siCtrl or S2PNP-siEpsin1/2 for 24h,
1042 RNA was isolated, and qRT-PCR was performed (n=3, **S2PNP-siCtrl vs S2PNP-siEpsin1/2
1043 group, P<0.01). B-J are presented as mean ± SD and were analyzed using one-way ANOVA (B
1044 and C) and the unpaired Student's t-test (E-J).

1045

Online Supplemental Materials

Targeting Epsins by nanotherapy regulates lipid metabolism and promotes ABCG1-mediated cholesterol efflux to fortify atheroma regression

Kui Cui[1]†, Xinlei Gao[2]†, Beibei Wang[1]†, Hao Wu[1], Yunzhou Dong[1], Yuling Xiao[3], Xingya Jiang[3], Marina V. Malovichko[4], Kathryn Li[1], Dan Shan[1], Qianman Peng[1], Yaowei Lu[1], Bo Zhu[1], Rongbin Zheng[2], Scott Wong[1], Douglas B. Cowan[1], MacRae Linton[5], Sanjay Srivastava[4], Jinjun Shi[3], Kaifu Chen[2*], Hong Chen[1*]

†These authors contributed equally to this work.

*Corresponding authors. Email: hong.chen@childrens.harvard.edu

kaifu.chen@childrens.harvard.edu

The supplemental materials include:

Materials and Methods

Figure S1. Cell populations were annotated based on marker gene expression.

Figure S2. Cell proportion changes for each cell type in WT and DKO.

Figure S3. RNA-seq analysis of WT and DKO macrophages reveals that Epsins regulate lipid cholesterol metabolism and efflux pathways.

Figure S4. Gating strategy and clathrin-mediated CD36 internalization.

Figure S5. The loss of Epsins reduced oxLDL uptake by macrophages.

1067 Figure S6. Transfection of full-length Epsin1 and constructs with the ENTH and UIM domains
1068 deleted into WT macrophages did not affect lipid uptake.

1069 Figure S7. Differentially expressed genes between WT and ABCG1 knockout (ABCG1KO)
1070 macrophages.

1071 Figure S8. Schematic of the quantification for radiolabeled cholesterol.

1072 Figure S9. Gene expression levels of indicated gene in WT and DKO macrophage.

1073 Figure S10. Gating strategy and clathrin mediated-ABCG1 endocytosis.

1074 Figure S11. The expression of ABCG1 decreased with atherosclerotic progress in humans and
1075 mice.

1076 Figure S12. Characterization and silencing efficacy of S2P-conjugated siEpsin1/2 NPs.

1077 Figure S13. S2PNP-siEpsin1/2 treated macrophages show reduced foam cell formation.

1078 Figure S14. S2PNP-siEpsin1/2 inhibits lesion formation and macrophage accumulation in early
1079 stage of atherosclerosis.

1080 Figure S15. Silencing lesional macrophage Epsin1/2 by S2PNP-siEpsin1/2 NP-treatment
1081 stabilized plaques in a progression model of atherosclerosis.

1082 Figure S16. Delivery of S2PNP-siEpsin1/2 does not change cholesterol and triglyceride levels of
1083 $ApoE^{-/-}$ mice fed a WD.

1084 Figure S17. Silencing macrophage Epsin1/2 by S2PNP-siEpsin1/2 NPs reduces lesion size in a
1085 regression model of atherosclerosis.

1086 Figure S18. Summary schematic diagram of the study.

1087 Table S1. List of reagents and animal models.

1088 Data file S1. Differentially expressed genes between cell clusters identified in all the cells in aorta.

1089 Data file S2. Differentially expressed genes between macrophage subclusters.

1090 Data file S3. Differentially expressed genes in DKO compared to wild type.

1091 Data file S4. Gene Ontology enrichment analysis for DEGs shared by DKO and CD36KO.

1092 Data file S5. Gene differential expression analysis between ABCG1KO and wild type
1093 macrophages.

1094 Data file S6. Gene Ontology enrichment analysis for DEGs in ABCG1KO compared to wild type.

1095 Data file S7. Gene Ontology enrichment analysis for pathways reversely regulated by ABCG1KO
1096 and DKO.

1097 Data file S8. Uncropped Western Blot.

1098 Data file S9. Primary data of statistical analysis.

1099

1100 **MATERIALS and METHODS**

1101 **Isolation of primary mouse macrophage and macrophage culture**

1102 The isolation of peritoneal macrophages was performed as described previously [82]. Briefly,
1103 mice were intraperitoneally injected with 1mL of 4% thioglycolate (TG), and 3 days post-injection,
1104 mice were sacrificed, and peritoneal cells were harvested with 7mL of sterile PBS by lavage of
1105 peritoneal cavity. Cells were spun down (1000xg, 5 minutes), washed with PBS, resuspended, and
1106 plated in RPMI (containing 10% FBS and 1% Pen-Strep) at 37 °C in humidified air containing 5%
1107 CO_2 atmosphere. After 3 hours, non-macrophages were washed with PBS. For bone marrow-
1108 derived macrophages, mice were sacrificed, and both femurs and tibias were dissected and flushed
1109 with sterile 1X PBS, followed by passing through a 70μM cell strainer. Cells were spun down
1110 (1000xg, 5 minutes), washed with PBS, and seeded in RPMI (containing 10% FBS and 1% Pen-
1111 Strep) with macrophage colony stimulating factor (M-CSF, 10ng/mL) to differentiate into
1112 macrophages for 5 days. After which, the macrophages were harvested and used in experiments.
1113 Both bone marrow-derived and isolated peritoneal primary macrophages were used to confirm
1114 knock out of Epsin1 and Epsin2. Isolated peritoneal macrophages were mainly used for western
1115 blots, flow cytometry and immunoprecipitations due to higher yields.

1116 **RNA isolation, quantitative real-time PCR and RNA sequencing**

1117 Total RNA was extracted from primary macrophages with Qiagen RNeasy Mini Kit based on
1118 manufacturer's instruction including the optional step to eliminate genomic DNA. The extracted
1119 RNA was either used for qRT-PCR or RNA sequencing according to the experimental designs.

1120 For qRT-PCR, mRNA was reverse transcribed to cDNA with the iScript cDNA Synthesis Kit
1121 (Bio-Rad Laboratories, Inc., Hercules, CA, United States). 2 μL of the product was subjected to

1122 qRT-PCR in StepOnePlus Real-Time PCR System (Applied Biosystems) using SYBR Green PCR
1123 Master Mix reagent as the detector. PCR amplification was performed in triplicate on 96-well
1124 optical reaction plates and replicated in at least three independent experiments. The ΔΔCt method
1125 was used to analyze qPCR data. The Ct of β-actin cDNA was used to normalize all samples.
1126 Primers are listed in Supplemental Table S1. For RNA sequencing, extracted RNA from primary
1127 macrophages with Qiagen RNeasy Mini Kit based on manufacturer's instruction were sent to BGI
1128 Genomics Company (San Jose, USA) for RNA sequencing.

1129 **RNA sequencing data processing and differential expression analysis**

1130 The raw reads of RNA sequencing data were mapped to the mouse genome (version mm10)
1131 using STAR (version 2.7.9a) [83] or TopHat (version v2.1.1) [84]. The read count was calculated for
1132 each gene by htseq-count (version 0.11.2) [85] and further normalized to TPM (transcripts per
1133 million) and FPKM (fragments per kilobase of transcript per million fragments mapped). For
1134 differential expression analysis of Epsin deficient and wild type macrophage dataset, the read
1135 count matrix produced by htseq-count was imported into the R package DESeq2 (version 1.30.1)
1136 [86]. For the ABCG1 knock out dataset, we first performed a batch effect removal on the log10
1137 transformed TPM expression matrix using ComBat in the R package sva (version 3.38.0) [87]. Then,
1138 the R package limma was used to do differential expression analysis for the batch effect-removed
1139 expression matrix. Genes with fold change larger than 1.2-fold and p-value less than 0.05 were
1140 identified as differentially expressed genes (DEGs). Principal component analysis (PCA) was
1141 conducted by the plotPCA function of DESeq2. Heatmap of gene expression values was generated
1142 using the R package heatmap (version 1.0.12). Gene Ontology (GO) functional enrichment
1143 analysis was performed by the R package clusterProfiler (version 3.18.1) [88].

1144 For the comparison of DEGs between DKO and CD36 knockout macrophages in mice, we

1145 utilized the published bulk RNA-seq data from Chen et. al. [59], with the accession number
1146 GSE139439, downloaded from NCBI GEO database [89]. The overlapping DEGs co-regulated in
1147 DKO and CD36 knockout macrophages were analyzed by the R package VennDiagram (version
1148 1.6.20) [90]. The statistical significance of overlapping genes was calculated by Fisher exact test. All
1149 the data for bulk RNA-seq are available in Data files (S3-S7).

1150 **Cell culture and plasmids transfection**

1151 The HEK 293T cell line (ATCC no. CRL-11268) were used for plasmid transfection to map
1152 the binding sites of Epsin to CD36 or ABCG1. Flag-tagged Epsin1^{WT}, Epsin1$^{\Delta UIM}$, Epsin1$^{\Delta ENTH}$
1153 truncation constructs, and pcDNA vector were prepared previously in our lab[25]. CD36 (lot:52025)
1154 and ABCG1 (lot:53952) plasmids were purchased from AddGene. HEK 293T cells were cultured
1155 in DMEM (10% FBS and 1% Pen-Strep) at 37°C in humidified air containing 5% CO_2 atmosphere
1156 and transfected using Lipofectamine 2000 as instructed by the manufacturer. Transfection of Epsin
1157 domains to macrophage: Isolated WT and DKO peritoneal macrophages were cultured in RPMI
1158 media (containing 10% lipid-depleted serum and 1% Pen-Strep). Epsin1^{WT}, Epsin1$^{\Delta UIM}$,
1159 Epsin1$^{\Delta ENTH}$ truncation constructs, and pcDNA vector were transfected to macrophages using
1160 lipofectamine LTX transfection reagent or using Nucleofector II apparatus (Amaxa, Germany)
1161 with mouse macrophage nucleofector kit (Lot: VPA-1009, Lonza) as instructed by the manufacturer.

1162 **Immunoprecipitation (IP) and western blotting (WB)**

1163 For total protein levels, primary macrophages were washed with ice cold PBS, lysed in RIPA
1164 buffer (50 mM Tris HCl, 150 mM NaCl, 1.0% NP-40, 0.5% Sodium Deoxycholate, 1.0 mM
1165 EDTA, 0.1% SDS and 0.01% sodium azide at a pH of 7.4.), added 4X Laemmli buffer (1:3 dilution
1166 in lysis buffer) was added and WB was perfomed for the proteins indicated in this study. For IP,

1167 cells were washed with ice cold PBS, lysed with lysis buffer (1% Triton X-100, 5mM Na_3VO_4,
1168 10mM N-ethylmaleimide, and protease inhibitor cocktail), spun down (12000xg, 5 min at 4°C) to
1169 remove the debris. Cell lysates were pre-cleared with appropriate species of IgG and protein A/G
1170 Sepharose beads for 1h at 4°C with rotation followed by incubation with A/G Sepharose beads and
1171 indicated antibodies for 12 hours at 4°C with rotation. For negative controls, equal concentrations
1172 of mouse IgG were added instead of specific antibodies. Precipitated proteins were washed with
1173 ice cold lysis buffer for 3 time and eluted from protein A/G beads using 2X Laemmli buffer (1:1
1174 in lysis buffer) followed by WB as described previously [26]. WB were repeated for at least 3 times
1175 with different mice and bands were quantified using NIH ImageJ software. The protein expression
1176 levels were normalized to GAPDH levels. For IPs in macrophages involving oxLDL treatment,
1177 cells were pre-treated with 1 μM MG132 in serum-free media for 4 hours, followed by the
1178 treatment with or without oxLDL (100μg/ml) for 30 minutes at 37°C and processed for
1179 immunoprecipitation. For the transfection of Epsin1 constructs and CD36 or ABCG1 constructs,
1180 transfected HEK 293T cells were cultured in lipid-depleted DMEM media for 24 hours followed
1181 by stimulation with 100μg/mL oxLDL for 30 minutes at 37°C and performed for
1182 immunoprecipitation.

1183 **Atherosclerosis analysis**

1184 Mice were anesthetized with isoflurane. Blood was collected from the right atrium followed
1185 by left ventricle perfusion with cold PBS. Whole aortas, brachiocephalic artery (BCA) and hearts
1186 of the mice were isolated. Whole aortas were dissected symmetrically, pinned to parafilm and
1187 fixed in 4% PFA to allow the *en face* analysis. Heart and BCA were embedded in OCT mounting
1188 medium and immediately frozen. The aortic sinus and BCA in the heart were sectioned at 10
1189 microns (at least 9 sections of each sample were collected). The internal elastic lamina and luminal

1190 boundary of the lesion was manually traced and the lesion sizes of the *en face* aortas and aortic
1191 roots were quantified by NIH ImageJ software. The methods for Oil Red O (ORO) staining,
1192 immunofluorescent (IF) staining, Hematoxylin and Eosin (H&E) staining, and Van Gieson's
1193 staining are described in supplemental materials [26].

1194 ORO staining and IF staining of primary macrophages or cryosections were performed as
1195 described below. Oil Red O imaging was taken by a Zeiss Axio Scope.A1, AxioCam ICc5, and
1196 analyzed by ZEN-Lite 2012 software. Imaging of *en face* aortas was performed using a Nikon
1197 SMZ1500 stereomicroscope, SPOT Insight 2Mp Firewire digital camera, and SPOT Software 5.1.
1198 Imaging of IF staining was taken by Zeiss confocal microscope and quantification areas were
1199 performed by manually tracing the aortas, BCA, and aortic root lesion areas with NIH ImageJ
1200 software. Statistical analysis of samples including Oil Red O, Van Gieson's, H&E, and IF staining
1201 were performed by blinding in which each animal was assigned a number and data was collected
1202 based on the assigned number with genotype and experimental condition unknown to the data
1203 collector.

1204 **Oil Red O staining**

1205 For cryostat sections: cryostat sections 10 microns were fixed in 4% paraformaldehyde. Slides
1206 were washed with PBS (3 times, 5 min each time), and rinsed with 100% propylene glycol
1207 followed by staining with freshly prepared 0.5% Oil Red O solution for 10 minutes at 60°C. Slides
1208 were then put in 85% propylene glycol for 2 min, followed by 3 washes in water. Slides were next
1209 incubated with hematoxylin for 1-2 min, rinsed 3 times in water, and mounted with aqueous
1210 mounting medium. For foam cells: coverslips were washed with PBS, fixed in 4%
1211 paraformaldehyde for 10 min and stained with freshly prepared 0.5% Oil Red O solution for 10
1212 min at 65°C. Slides were then washed in PBS (3 times, 5min each time), incubated with

1213 hematoxylin for 1min, washed with PBS 3 times, and mounted on coverslips with aqueous
1214 mounting medium. Imaging was processed with a Zeiss LSM880 confocal microscope and
1215 analyzed with ZEN-Lite 2012 software and NIH ImageJ software. Quantification of lesion was
1216 performed as described above. Quantification of foam cells was performed as described below.

1217 **Hematoxylin and Eosin staining**

1218 Frozen aortic root and BCA sections: slides were fixed in 10% buffered formalin for 15 min
1219 and washed in water. Next, slides were stained with 0.1% hematoxylin for 3min followed by
1220 ddH_2O washes, 95% ethyl alcohol and water. Slides were then dipped in 0.5% Eosin for 3 min,
1221 quickly rinsed with ddH_2O, dipped in 95% and 100% ethanol, incubated in 50:50 Xylenes:100%
1222 ethanol and incubated in 100% Xylenes. Slides were mounted using Permount with coverslips.

1223 **Van Gieson's staining**

1224 Sections were fixed in 10% buffered formalin for 15 min and washed in water. Slides were
1225 stained with hematoxylin for 10 min, washed in ddH_2O, stained 1-3 min in Van Gieson's solution,
1226 dehydrated in 95% alcohol and 100% alcohol two times. Then, slides were cleared in xylene for
1227 two times and mounted with Permount. Staining results were presented as: Elastic fibers and
1228 nuclei–Black, Collagen fibers–Red and Other tissue elements–Yellow. Lesion area was traced
1229 using NIH ImageJ software. The percentage of necrotic area was determined by necrotic areas
1230 within the lesion. Collagen content was determined by the percentage of lesion areas.

1231 **Immunofluorescence staining**

1232 Human samples: human healthy and atherosclerotic aorta paraffin sections were deparaffinized
1233 in xylene for 15min, immersed in graded ethanol (100%, 100%, 95%, 90%, 80%, and 70%, each
1234 for 3 min), washed with running tap water and processed antigen retrieval with 10mM Sodium

1235 Citrate, pH 6.0, with 0.05% Tween 20 at 90°C for 10 min. Samples were blocked in PBS with 3%
1236 donkey serum, 3% BSA, and 0.3% Triton X-100 and incubated with primary antibodies ABCG1
1237 or CD68 (1:70 dilution) at 4°C overnight. The sections were washed three times and respective
1238 secondary antibodies conjugated to fluorescent labels (Alexa Flour 594, 488, or 647; 1:200 to
1239 1:500) were added for 2 h at room temperature. The sections were mounted with mounting medium
1240 containing DAPI (1:100).

1241 Mouse aortic root and BCA cryosections: Sections were fixed by 4% paraformaldehyde for 30
1242 min at room temperature and blocked in PBS solution containing 3% donkey and/or goat serum,
1243 3% BSA, and 0.3% Triton X-100 for 1hour. Samples were then incubated with primary antibody
1244 at 4°C overnight, followed by incubation with the respective secondary antibodies conjugated to
1245 fluorescent labels (Alexa Flour 594, 488, or 647; 1:200 to 1:500) for 2 h at room temperature. The
1246 sections were mounted with mounting medium containing DAPI (1:100).

1247 Staining of peritoneal macrophages: macrophages plated on the 18-mm coverslips were
1248 washed with PBS, fixed by 4% paraformaldehyde for 15 min at room temperature and blocked in
1249 PBS solution containing 3% donkey and/or goat serum, 3% BSA, and 0.3% Triton X-100 for 1hour.
1250 Coverslips were then incubated with primary antibody (CD36, ABCG1, EEA1, Rab11, or Lamp1;
1251 1:100-1:300) at 4°C overnight, followed by incubation with the respective secondary antibodies
1252 conjugated to fluorescent labels (Alexa Flour 594, 488, or 647; 1:200 to 1:500) for 1 hour at room
1253 temperature. The sections were mounted with mounting medium containing DAPI (1:100).
1254 BODIPY™ 493/503 staining of macrophages was performed following F4/80-fluorescent
1255 conjugated antibody incubation for 2 hours at room temperature [91]. Slides were washed with PBS,
1256 stained with DAPI and mounted. Immunofluorescent images were captured using a Zeiss LSM880
1257 confocal microscope and analyzed with ZEN-Lite 2012 software and HIH ImageJ software.

1258 Samples stained without the primary antibody were obtained using the same settings as negative
1259 controls. Mean fluorescence intensity (MFI) of antibody staining was determined using NIH
1260 ImageJ software with n=3 or more.

1261 **Flow cytometry assay**

1262 Flow cytometry of elicited primary macrophages: peritoneal macrophages from WT and DKO
1263 mice were isolated as described above and plated in 6 well plates in lipid-deficient medium for 24
1264 hours followed by the treatment with or without 100μg/mL oxLDL in the presence or absence of
1265 clathrin siRNA at 37^0C for different time based on the experiment designs. Macrophages were
1266 washed with 1XPBS, dissociated with 1mL non-enzymatic cell dissociation buffer, centrifuged
1267 (300x*g*, 5 minutes), and resuspended in 100μL FACS buffer (1X PBS, 2% FBS, 2mM EDTA)
1268 containing the following: FcR Blocking Reagent, fluorochrome conjugated anti-F4/80, primary
1269 antibodies against CD36 or ABCG1. Cells were incubated with the primary antibodies (1:100) on
1270 ice for 30min, washed with 100μL FACS buffer, spun down and resuspended with 100μL FACS
1271 buffer containing the fluorescent secondary antibodies (1:100). After 30 min, cells were washed
1272 with FACS buffer, fixed with 4% paraformaldehyde (PFA), and resuspended in FACS buffer for
1273 analysis. Single color and no color controls were prepared using elicited macrophages, which were
1274 treated the same as experimental groups. Expression of cell markers was analyzed using a FlowJo
1275 version 10 software. Gating strategies were performed as described in Supplemental Figures S4
1276 and S10. Flow cytometry of DiI-oxLDL treated macrophages: peritoneal macrophages elicited
1277 from WT and DKO mice were incubated in lipid-deficient medium for 24h followed by the
1278 treatment of DiI-oxLDL for 2h at 37^0C and macrophages were washed with 1XPBS, dissociated
1279 with 1mL non-enzymatic cell dissociation buffer, centrifuged (300xg, 5 minutes), resuspended in
1280 100μL FACS buffer (1X PBS, 2% FBS, 2mM EDTA) containing the following: FcR Blocking

1281 Reagent, fluorochrome conjugated anti-F4/80 antibody staining, fixed and assessed the uptake of
1282 lipoproteins by flow cytometry as described above.

1283 **Foam cell formation**

1284 TG (4%) induced peritoneal macrophages were isolated and plated on 18mm glass coverslips.
1285 Cells were cultured in RPM media (containing 10% lipid-depleted serum and 1% PennStrep) for
1286 24 hours and then treated with 10-100 μg/mL oxLDL for 24 hours [26]. Cells were fixed in 4% PFA
1287 for 10 minutes at room temperature and washed with PBS. For Oil Red O staining, coverslips were
1288 stained with Oil Red O, washed with PBS, counterstained with hematoxylin, washed with PBS,
1289 and then mounted on slides. For Bodipy staining, coverslips were immunofluorescently stained
1290 BodipyTM 493/503 and phalloidin-iFluor 555 reagent for 1 hour at 37°C, counterstaining with
1291 DAPI, and mounting on slides. Negative controls were not treated with oxLDL. Foam cells were
1292 determined as the number of lipid positive cells (Oil Red O positive or Bodipy positive) as a
1293 percentage of total cells. At least 6 fields per cover slip and 6 mice per genotype were used for
1294 quantification.

1295 **Cell surface biotinylation**

1296 Cell surface biotinylation was performed as described previously [26]. Isolated peritoneal
1297 macrophages in the plate were washed with cold PBS, suspended at a concentration of $25x10^6$
1298 cells/mL and treated with 2mM EZ-Link Sulfo-NHS-LC-Biotin reagent on ice for 30 minutes
1299 followed by 3 washes with 100mM Glycine to remove excess biotin and then 3 washes with cold
1300 PBS (5min each time). Cells were lysed and pulled down by streptavidin bead: cell lysates were
1301 incubated with neutravidin beads for at least 12 hours at 4°C with rotation, and proteins were eluted
1302 from beads using 4X Laemmli buffer diluted 1:3 in lysis buffer. Cell surface biotinylated proteins

1303 were analyzed by western blotting and quantified using NIH Image J software.

1304 **Plasma collection, triglyceride, and cholesterol analysis**

1305 For each mouse, 1mL syringe were rinsed with 1mL 0.5M EDTA to coat the inside of the
1306 syringe with EDTA to prevent clotting during blood collection. Blood was collected from the right
1307 atrium of the mouse heart after sacrifice with isoflurane and added to each 1.7mL tube containing
1308 50µL 0.5M EDTA. Blood was centrifuged at 2000xg for 10 minutes at 4°C. Plasma was transferred
1309 to a new tube and stored at -20°C. Plasma cholesterol and triglyceride levels were determined as
1310 described below.

1311 Total cholesterol, high-density lipoprotein (HDL) cholesterol and triglycerides in mouse serum
1312 were determined on Ace Axcel® Clinical Chemistry System (Alfa Wassermann, West Caldwell,
1313 NJ). Non-HDL cholesterol is calculated as Total Cholesterol – HDL and gives a measure of the
1314 cholesterol carried by all of the atherogenic lipoproteins.

1315 Quantification of total cholesterol, HDL and triglycerides in macrophages. Lipids were
1316 extracted from macrophages with hexane:isopropanol (3:2, v:v) as described in Robinet et al [92].
1317 Solvents were removed by drying with nitrogen gas. Extracts were resolubilized in 5% bovine
1318 serum solution by bath sonication (10 minutes at 37°C), freeze/thaw treatment (1 hour at -80°C)
1319 and followed by probe sonication for 10 seconds. Reconstituted samples were analyzed on Ace
1320 Axcel® Clinical Chemistry System for total cholesterol, HDL and triglycerides as described above
1321 for measurements in mouse serum. Obtained values were normalized to total protein measured in
1322 the cell lysates by Bradford Protein Assay (Bio-Rad).

1323 **Macrophage cholesterol efflux assay**

1324 Thioglycolate induced peritoneal macrophages from WT, DKO and DKO/ABCG1$^{fl/+}$ mice
1325 were plated in RPMI medium for 2-4 hours. Non-adherent cells were removed by washing with

1326 PBS and cells were incubated with radiolabeled medium supplemented with 4 μCi/mL of [^{3}H]-
1327 cholesterol (Perkin-Elmer, Waltham, MA, USA), 5% FBS,1% P/S and 50μg/mL acetyl-LDL for
1328 24 hours. Macrophages were washed twice with warm PBS and incubated with serum-free RPMI
1329 1640 medium supplemented with 0.2% BSA, 2μg/mL acyl-CoA cholesterol acyltransferase
1330 (ACAT) inhibitor and 4μmol/L LXR agonist T0901317 for 18 hours equilibration [81]. After this
1331 equilibration period, cells were washed twice with warm PBS and incubated in serum free RPMI
1332 medium supplemented with or without cholesterol acceptors (10 μg/mL ApoA-1 or 25 μg/mL
1333 HDL) and 2μg/mL ACAT inhibitor for 4 hours [93]. At the end of the incubation, the efflux media
1334 was collected and filtered through a 0.45-μm filter to remove the detached cells. Then, transfer the
1335 efflux medium was transferred to a scintillation vial. The macrophages in the plates were added to
1336 500 μL of 0.2N NaOH and incubated on shaker at 4 °C overnight. Cell extract from each well was
1337 transferred to a scintillation vial. 4 mL of scintillation liquid were added to each scintillation vial
1338 and radioactivity was measured by liquid-scintillation counting [94]**.** The cholesterol efflux to
1339 acceptors was expressed as a percentage of total cholesterol using the following formula: %
1340 cholesterol efflux = (medium [^{3}H]-radioactivity [cpm]) / [(medium [^{3}H]-radioactivity [cpm] +
1341 [^{3}H]-radioactivity from cell extract [cpm])] x 100, where cpm = counts per minute.

1342 **Reverse cholesterol transport (RCT) assay**

1343 In vivo RCT experiment is based on the method detailed by Joan Carles Escolà-Gil et al [94].
1344 Briefly, macrophages were radiolabeled with [^{3}H]-cholesterol (5 μCi/mL) in 10% lipoprotein-
1345 depleted serum, 1% P/S and 50μg/mL acetyl-LDL RPMI media for 48h. Foam cells were washed
1346 with serum-free media supplemented with 0.2% BSA and equilibrated for 4h (37 °C, 5 % CO_2).
1347 Then, [^{3}H]-cholesterol-labeled macrophages were detached, spun down and resuspended in PBS.
1348 The injection dose was 0.5 mL per mouse (4x10^6 cpm/mL) administered intraperitoneally into

1349 C57BL/6 WT mice fed on normal diet as indicated in Figure 5C. Mice were then individually
1350 housed in metabolic cages and feces in the cage floor were collected for 2 days. At 48h, mice were
1351 sacrificed and blood, liver, intestinal contents were collected in Figure S8. Serum [^{3}H]-cholesterol
1352 was measured by liquid scintillation counting. [^{3}H]-HDL cholesterol was determined after
1353 precipitation of ApoB-containing lipoproteins with 0.44mM phosphotungstic acid and 20mM
1354 $MgCl_2$. Liver, fecal and intestinal lipids were extracted with hexane- isopropanol (3:2, v:v) and
1355 partitioned against Na_2SO_4. The lipid layer was collected and dried for 48h using nitrogen gas in a
1356 fume hood, and [^{3}H]-cholesterol radioactivity was measured by liquid scintillation counting (4mL
1357 scintillation fluid for 4 min). The [^{3}H]-radioactivity observed in fecal biliary acids was determined
1358 in the remaining aqueous phase of fecal material extracts. The amount of [^{3}H]-radioactivity was
1359 expressed as a percentage of the total injected dose, which was taken as 100%.

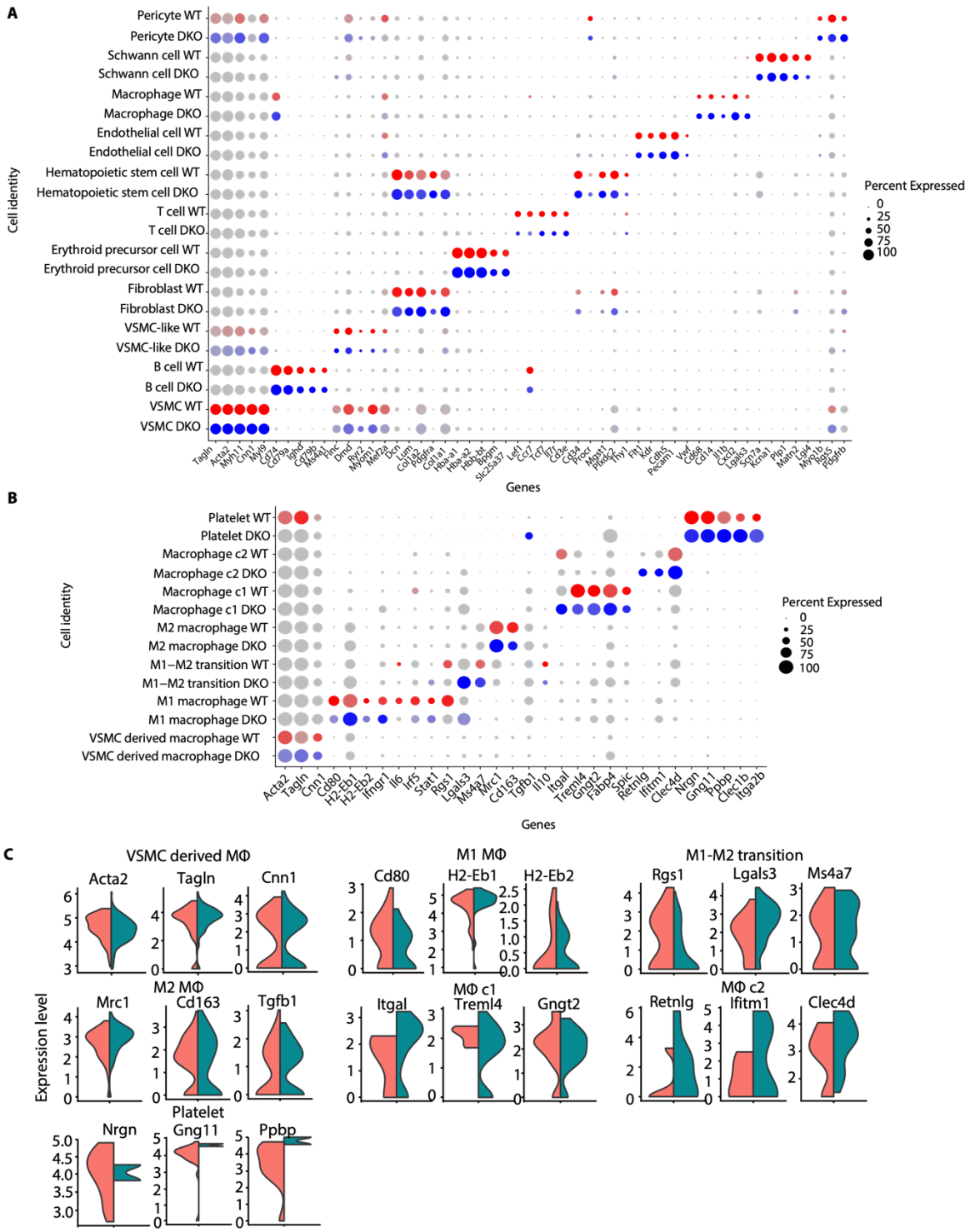
A
Pericyte WT
Pericyte DKO
Schwann cell WT
Schwann cell DKO
Macrophage WT
Macrophage DKO
Endothelial cell WT
Endothelial cell DKO
Hematopoietic stem cell WT
Hematopoietic stem cell DKO
T cell WT
T cell DKO
Erythroid precursor cell WT
Erythroid precursor cell DKO
Fibroblast WT
Fibroblast DKO
VSMC-like WT
VSMC-like DKO
B cell WT
B cell DKO
VSMC WT
VSMC DKO
Cell identity
Genes
Percent Expressed
0
25
50
75
100
B
Platelet WT
Platelet DKO
Macrophage c2 WT
Macrophage c2 DKO
Macrophage c1 WT
Macrophage c1 DKO
M2 macrophage WT
M2 macrophage DKO
M1–M2 transition WT
M1–M2 transition DKO
M1 macrophage WT
M1 macrophage DKO
VSMC derived macrophage WT
VSMC derived macrophage DKO
Cell identity
Genes
Percent Expressed
0
25
50
75
100
C
VSMC derived MΦ
Acta2
Tagln
Cnn1
M1 MΦ
Cd80
H2-Eb1
H2-Eb2
M1-M2 transition
Rgs1
Lgals3
Ms4a7
M2 MΦ
Mrc1
Cd163
Tgfb1
MΦ c1
Itgal
Tremlt4
Gngt2
MΦ c2
Retnlg
Ifitm1
Clec4d
Platelet
Nrgn
Gng11
Ppbp
Expression level

Figure S1

1362 **Figure S1. Cell populations were annotated based on marker gene expression.** (**A**) Dot plot
1363 of known marker genes for each cell cluster in Figure 1A. Marker gene expression are colored by
1364 red and blue for WT and DKO, respectively. Size of nodes represent percentage of cells expressing
1365 a certain gene. (**B**) Dot plot of known marker genes for each macrophage subclusters. (**C**) Violin
1366 plots showing the representative marker gene expression in each macrophage subclusters in WT
1367 and DKO.
1368

1369 **SUPPLEMENTAL FIGURES AND LEGENDS**

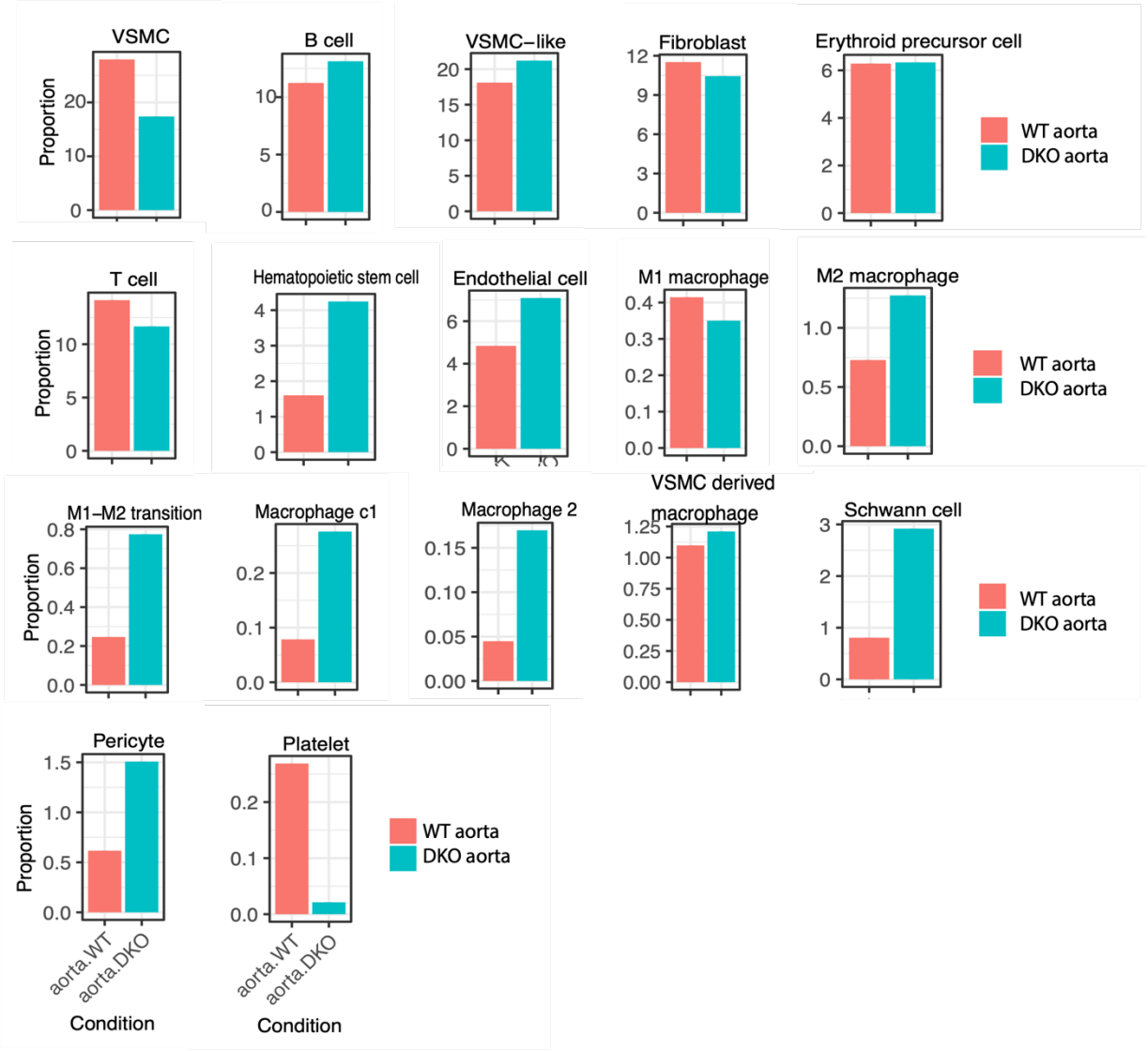

1370

1371 **Figure S2. Cell proportion changes for each cell type in WT and DKO.** The bar plots showing

1372 the cell proportion of M1 macrophage was decreased, while those of M2 macrophage and M1-M2

1373 transition cells were increased in DKO compared to WT.

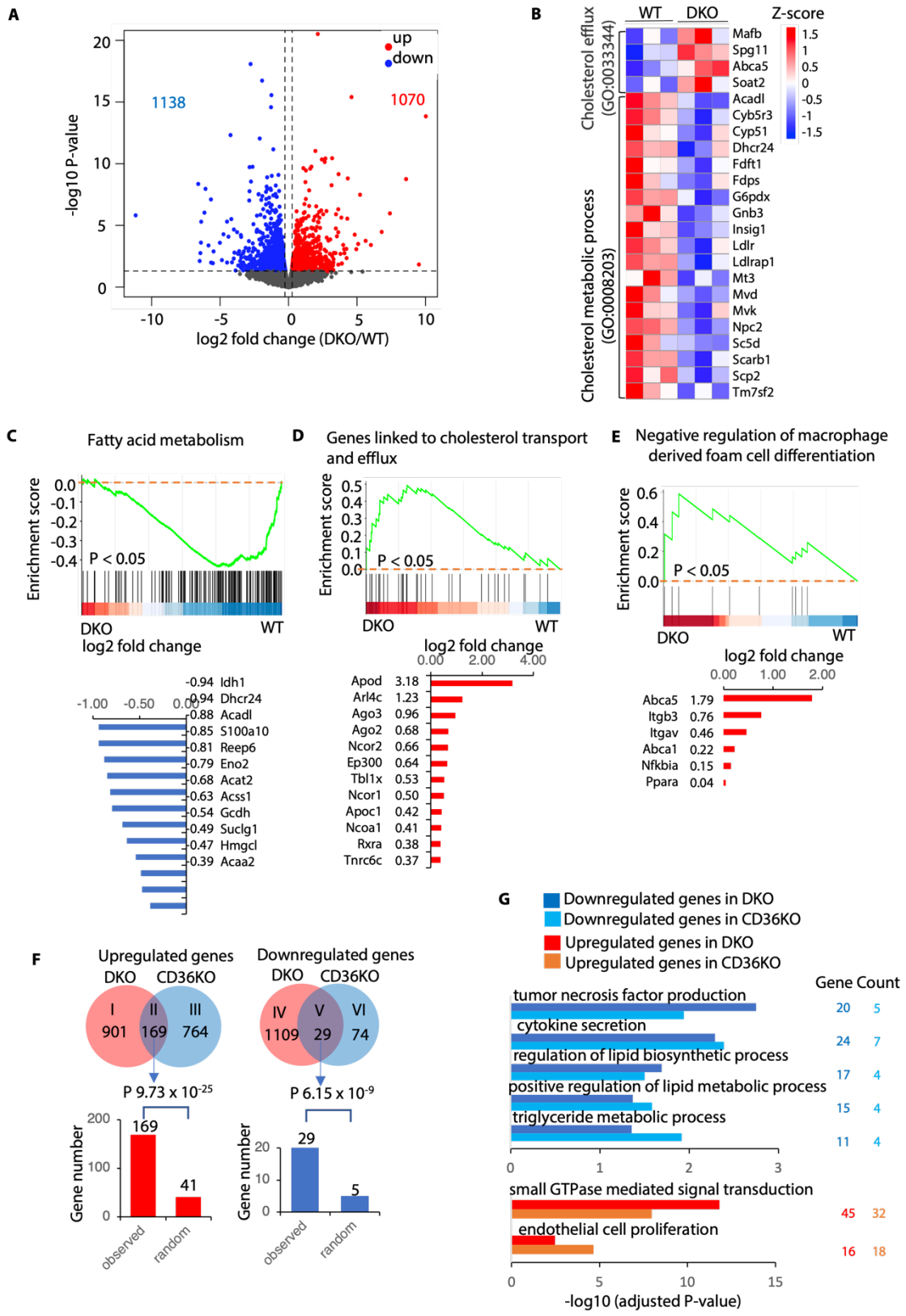

Figure S3

1374

1375 **Figure S3. RNA-seq analysis of WT and DKO macrophages reveals that Epsins regulate lipid**
1376 **cholesterol metabolism and efflux pathways**. (**A**) A volcano plot showing differential gene
1377 expression in Epsin deficient (DKO) and wild type (WT) macrophages. Red and blue indicate up-
1378 and down-regulated genes, respectively. (**B**) A heatmap showing the expression of genes involved
1379 in the cholesterol metabolic process (GO:0008203) and cholesterol efflux (GO:0033344). (**C-E**)
1380 GSEA demonstrated the tendency of individual pathways to be up- or down- regulated in Epsin
1381 deficient macrophages compared to wild type (top panels). The bar plots (bottom panels) showing
1382 log2 fold change of altered genes in these pathways. (**F**) Venn diagrams (top panels) showing the
1383 number of overlapping up- and down-regulated genes in DKO and CD36 knockout (CD36KO)
1384 samples. Bar plots (bottom panels) showing the observed numbers of overlapped genes versus
1385 numbers expected by random chance. The P-value was calculated using two tail Fisher exact test.
1386 (**G**) The Gene Ontology (GO) enrichment analysis for shared down regulated (top) and up
1387 regulated genes (bottom) between DKO and CD36KO macrophages. Benjamini corrected P-
1388 values are indicated on the x-axis.
1389

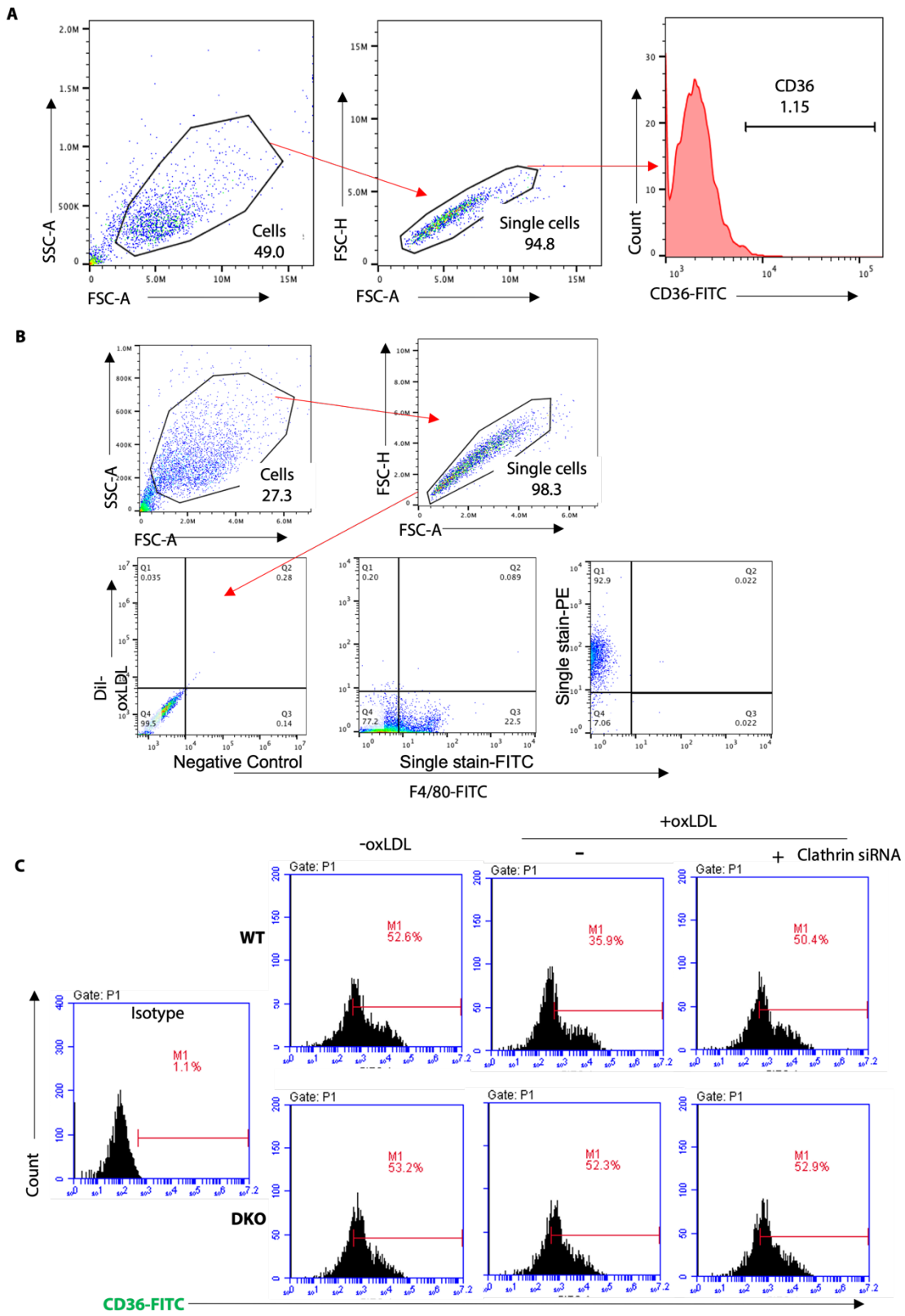

Figure S4

1390

1391 **Figure S4. Gating strategy and clathrin-mediated CD36 internalization.** (**A**) Macrophages
1392 isolated from WT (n=6) and DKO (n=6) mice were incubated in lipid-deficient medium for 24h
1393 followed by treatment with oxLDL for 2h, then staining with CD36-Alex488 and cytometric
1394 analyses. (**B**) Macrophages isolated from WT (n=6) and DKO (n=6) mice were incubated in lipid-
1395 deficient medium for 24h followed by the treatment of 10 μg/mL Dil-oxLDL for 2h at 37^0C and
1396 assessed the uptake of lipoproteins by flow cytometry. The major macrophage population was
1397 selected in forward vs side scatter plots and single cell determination was performed by FSC-H vs
1398 FSC-A. CD36 (A) or DiI-oxLDL (B) positive macrophages were presented in Figure 2C and 2H,
1399 respectively. (**C**) WT and DKO macrophages were incubated in lipid-deficient medium and
1400 transfected with clathrin siRNA for 24h followed by treatment with or without 100μg/mL oxLDL
1401 for 15 mins at 37^0C. Flow cytometry for surface level of CD36.
1402

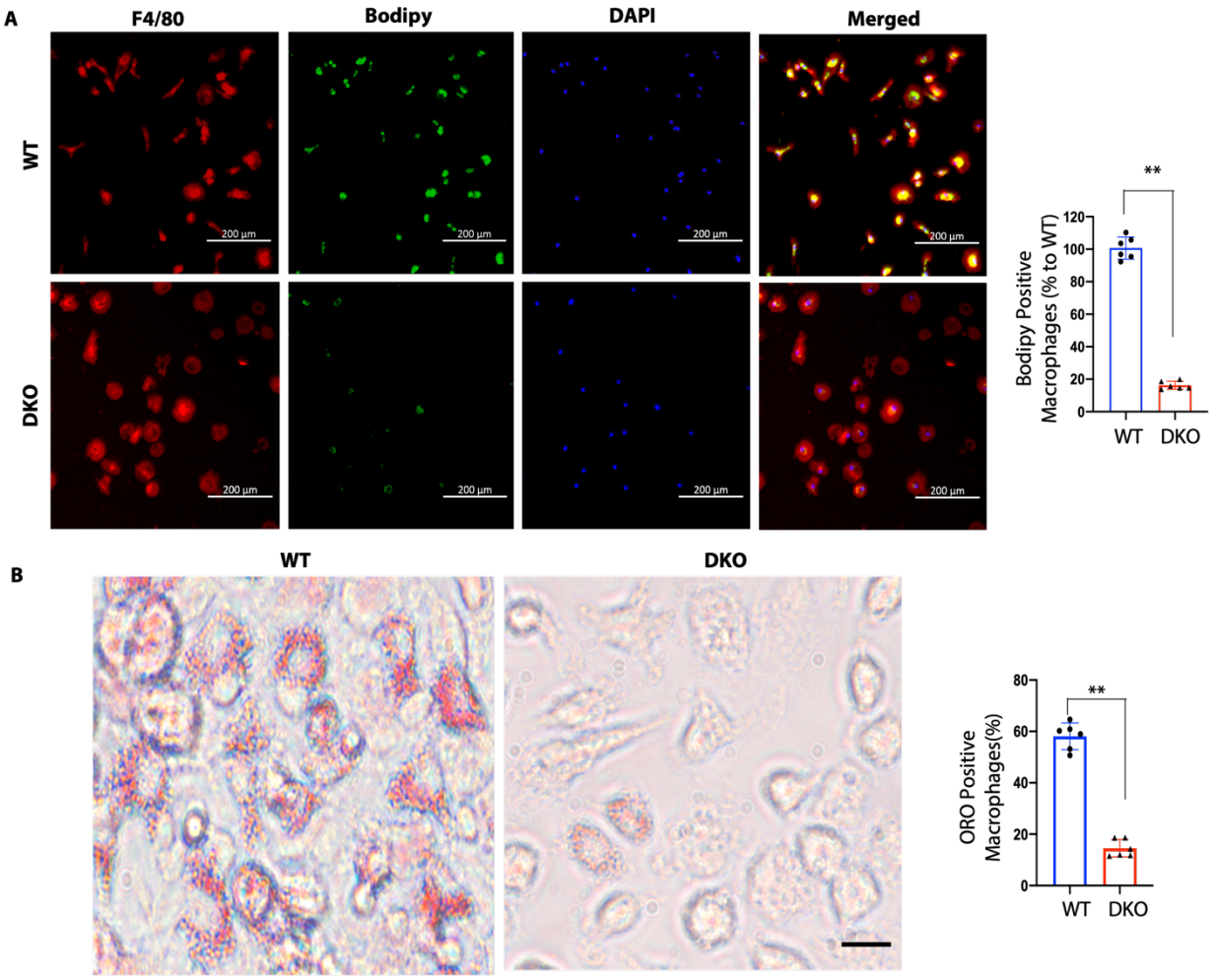

Figure S5

Figure S5. The loss of Epsins reduced oxLDL uptake by macrophages. (**A**) Isolated peritoneal macrophages from WT (n=6) and DKO (n=6) mice were pre-incubated with 25μg/mL oxLDL for 24h in lipid-deficient medium and stained with BODIPY (lipids, green), F4/80 (macrophage, red), and DAPI (blue), **WT vs DKO group, n=6, P<0.01, scale bar=200μm. (**B**) ORO staining of peritoneal macrophages, which were pre-incubated with 25μg/mL oxLDL for 24h in lipid-deficient medium, **WT vs DKO group, n=6, P<0.01, scale bar=20μm. Data are presented as mean ± SD and were analyzed using an unpaired Student's t-test.

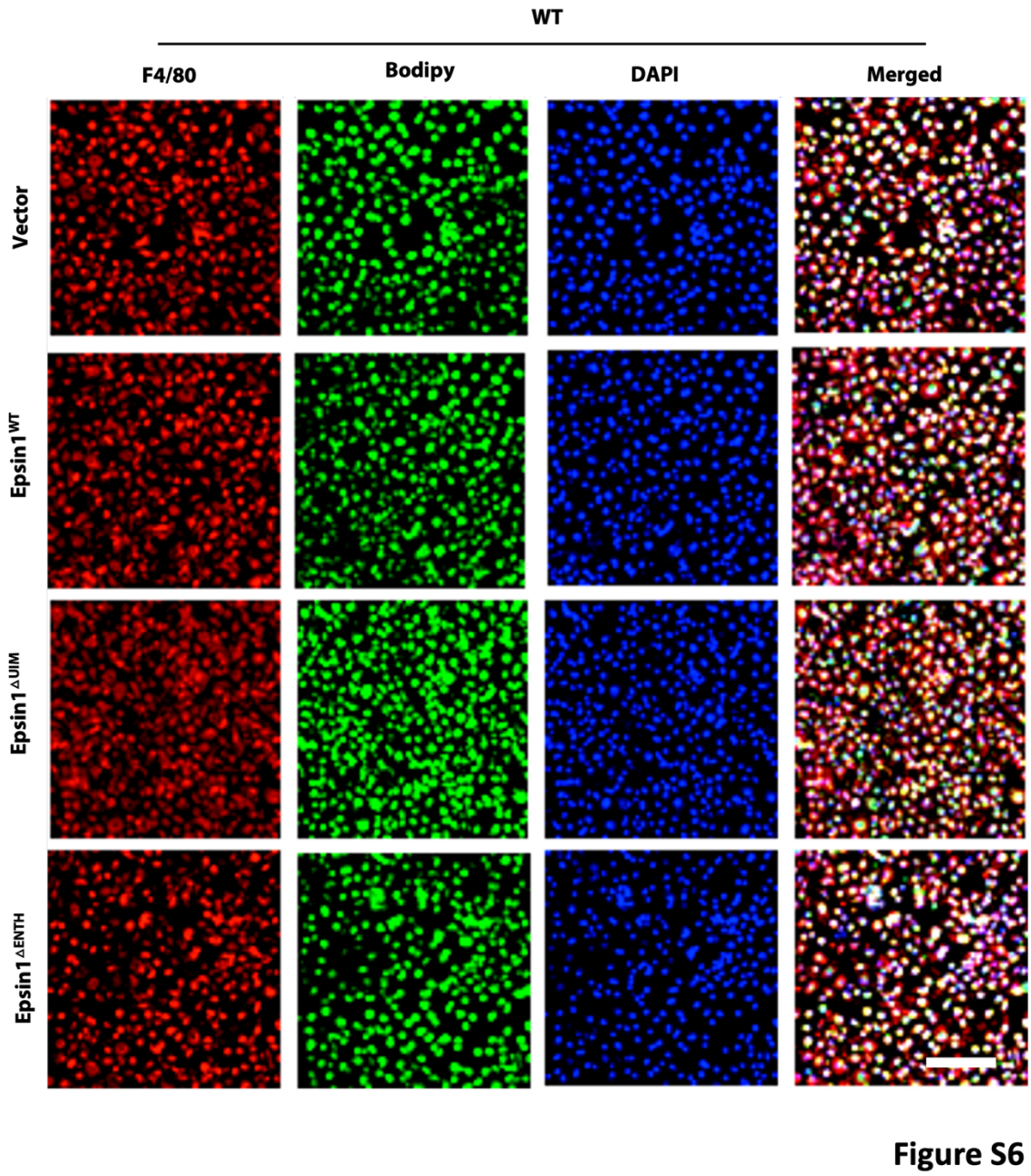

1411

1412 **Figure S6. Transfection of full-length Epsin1 and constructs with the ENTH and UIM**
1413 **domains deleted into WT macrophages did not affect lipid uptake.** Constructs of FLAG-
1414 Epsin1 WT, ΔENTH, and ΔUIM were transfected into ApoE$^{-/-}$/WT macrophages for 48h and
1415 treated with 100 μg/mL oxLDL for 1h, followed by staining with F4/80 (red), BODIPY (green)
1416 and DAPI (blue). Scale bars=200μm. Statistical analyses are presented in Figure 3E.

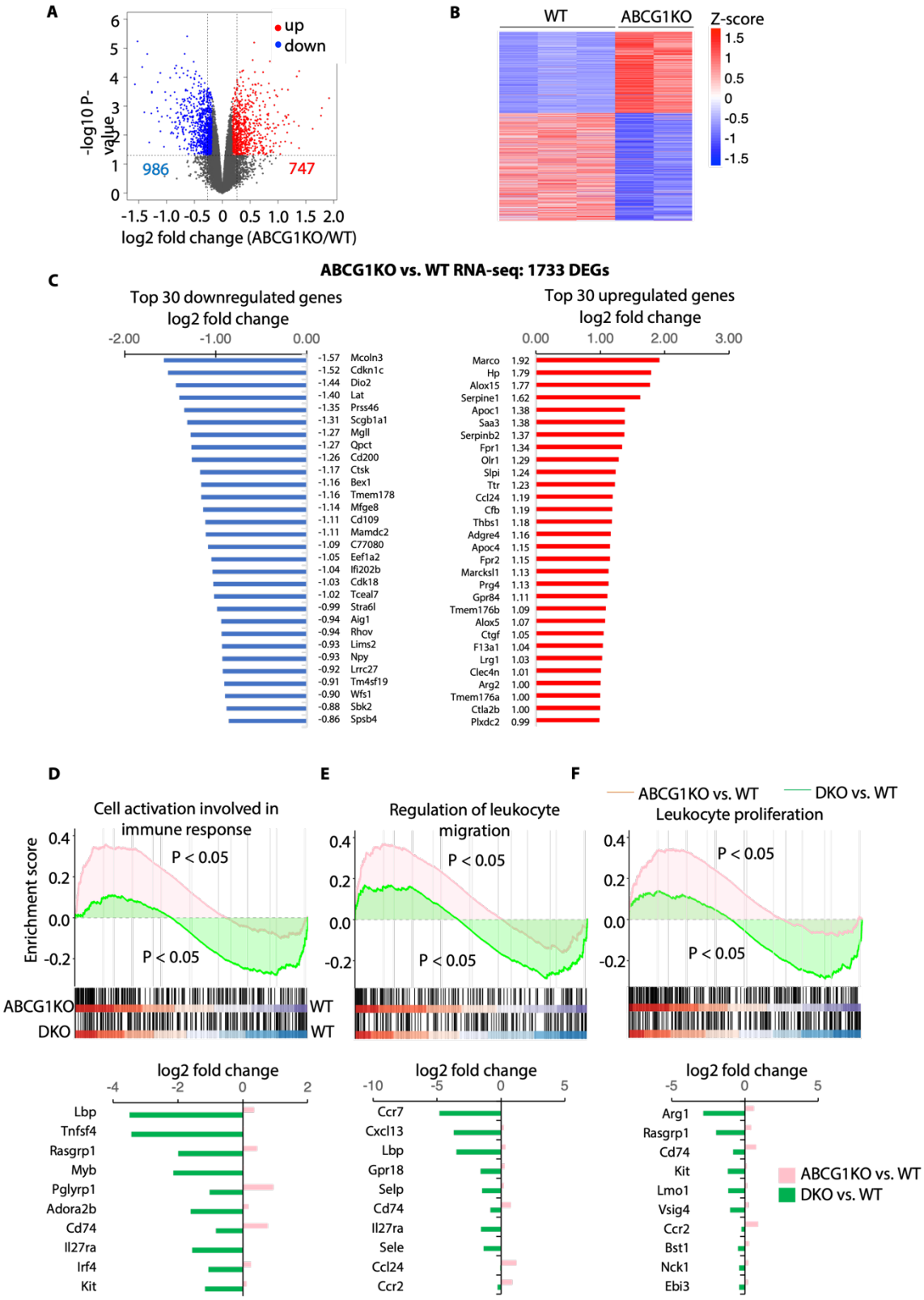

Figure S7

1417

1418 **Figure S7. Differentially expressed genes between WT and ABCG1 knockout (ABCG1KO)**
1419 **macrophages.** (**A**) A volcano plot showing differential gene expression in ABCG1KO and WT
1420 macrophages. Red and blue indicate up- and down-regulated genes, respectively. (**B**) A heatmap
1421 exhibiting the expression values of up- and down-regulated genes in each sample. (**C**) Bar plots
1422 showing log2 fold changes of the top 30 up- and down-regulated genes between ABCG1KO and
1423 WT macrophages. Up- (red) and down-regulated (blue) genes are indicated. (**D**-**F**) GSEA (top
1424 panels) indicated the tendency of individual pathways to be up- or down-regulated in response to
1425 DKO or ABCG1KO compared to WT cells. Genes associated with cell activation involved in
1426 immune response (GO:0002263) (D), regulation of leukocyte migration (GO:0002685) (E), and
1427 leukocyte proliferation (GO:0070661) (F) were analyzed. The bar plots (bottom panels) showing
1428 log2 fold change of altered genes in these pathways.
1429

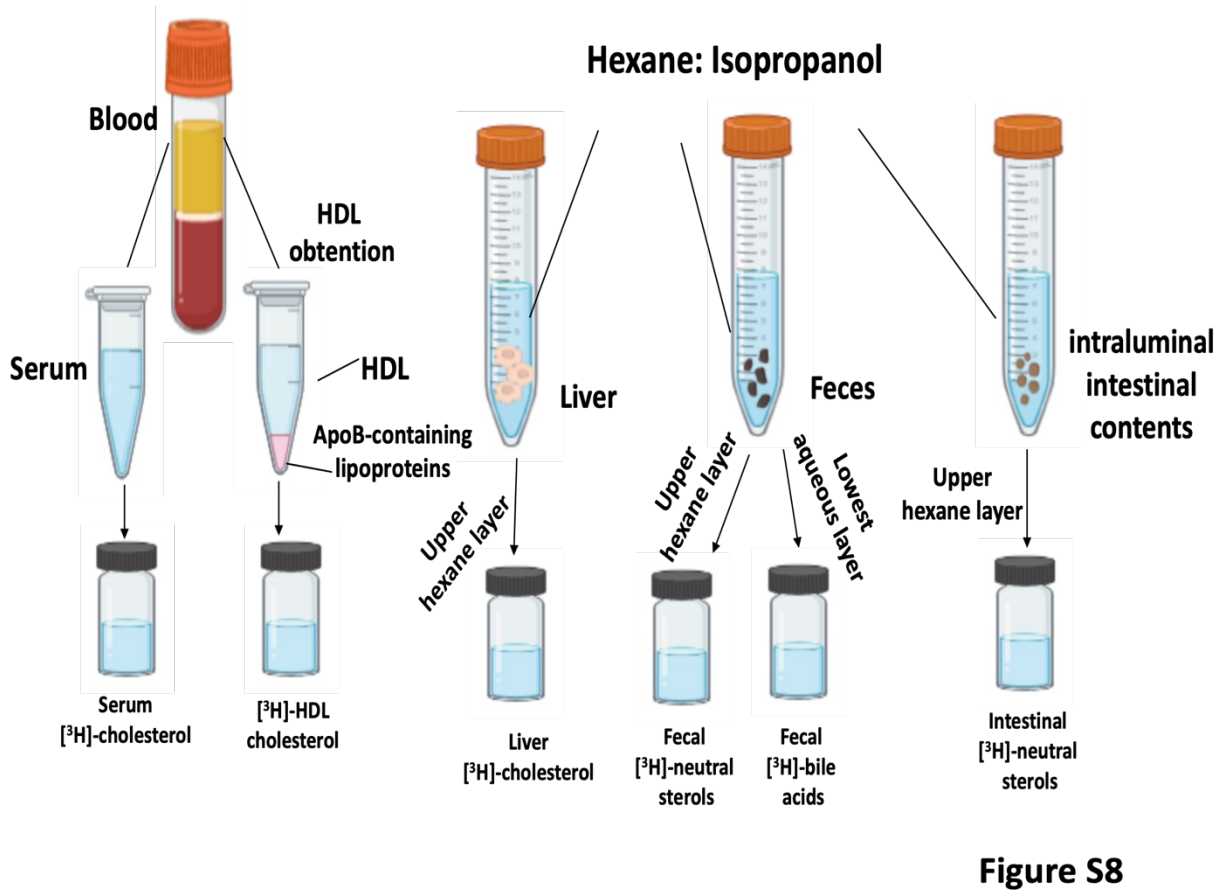

1430

1431 **Figure S8. Schematic of the quantification for radiolabeled cholesterol.** [^{3}H]-cholesterol was
1432 measured in serum and HDL after precipitating ApoB-containing lipoproteins. Liver, feces and
1433 intestinal lipids were extracted with hexane–isopropanol and partitioned against Na_2SO_4. Liver
1434 [^{3}H]-radioactivity was determined in the upper layer, which contains the [^{3}H]-cholesterol. In the
1435 feces extract, the amount of [^{3}H]-radioactivity was determined in the upper layer (neutral sterols)
1436 and the lowest layer (bile acids). In the intestinal contents, [^{3}H]-radioactivity was determined in
1437 the upper layer.

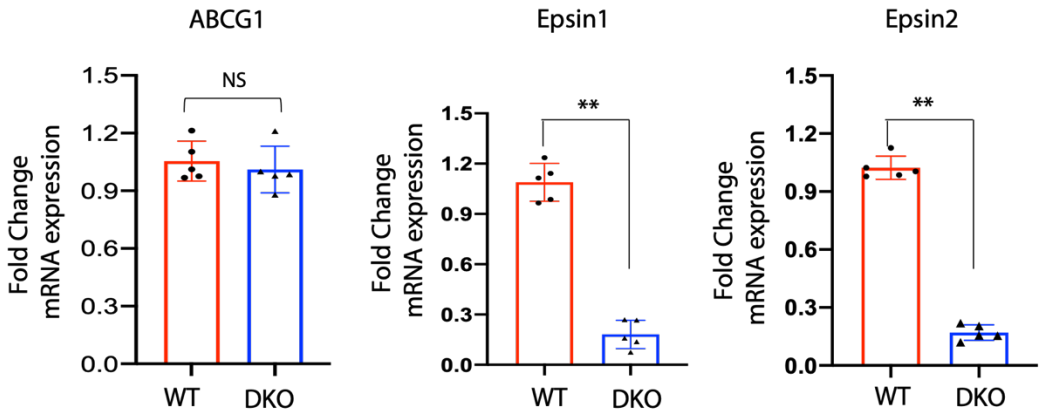

Figure S9

Figure S9. Gene expression levels of indicated genes in WT and DKO macrophage. Peritoneal macrophages were isolated from WT (n=5) and DKO (n=5) mice. Total RNA was extracted and mRNA levels of ABCG1, Epsin1, and Epsin2 were measured (NS=no significant difference, ** WT vs DKO group, n=5, P<0.01). Data are presented as mean ± SD and analyzed using an unpaired Student's t-test.

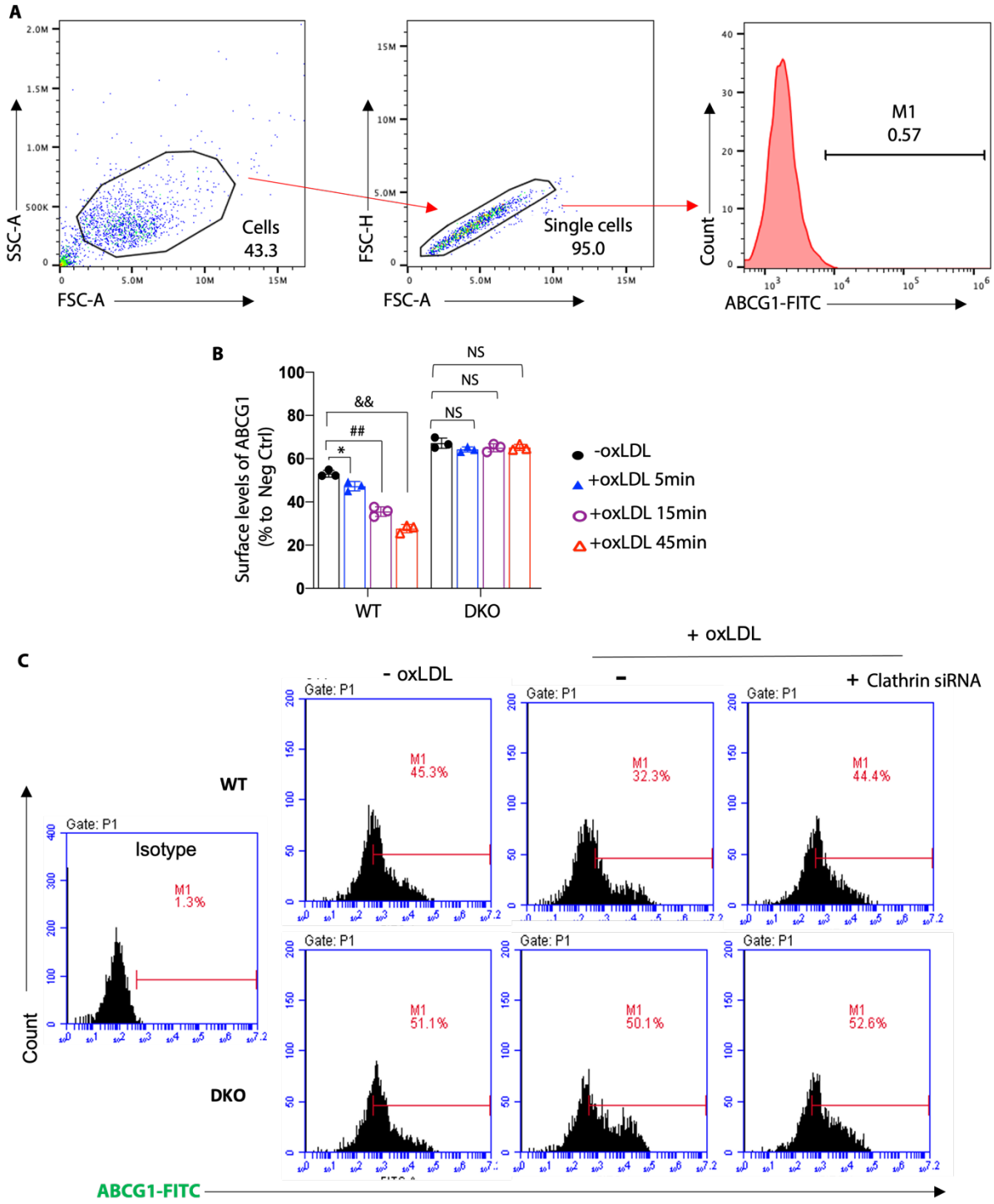

Figure S10

1444

1445

1446 **Figure S10. Gating strategy and clathrin mediated-ABCG1 endocytosis.** (**A**) Macrophages
1447 isolated from WT and DKO mice were incubated in lipid-deficient medium and treated with LXR
1448 agonist for 24h followed by treatment with or without 100 μg/mL oxLDL for 5min, 15min, and
1449 45min, and then stained with ABCG1. Surface levels of ABCG1 were assessed by flow cytometry.
1450 The major macrophage population was selected in forward versus side scatter plots and single cell
1451 determination was performed by FSC-H vs FSC-A. Isotype controls were gated in the histogram
1452 as M1 for the negative control of experimental groups for Figure 6C. (**B**) Statistical analysis is
1453 presented for Figure 6C. At least three independent experiments were performed for statistical
1454 analysis (*-oxLDL vs +oxLDL 5min, $P<0.05$; ##-oxLDL vs +oxLDL 15min, $P<0.01$; &&-oxLDL
1455 vs +oxLDL 45min, $P<0.01$). Data are presented as mean ± SD and analyzed using one-way
1456 ANOVA. **(C)** WT and DKO macrophages were incubated in lipid-deficient medium and
1457 transfected with clathrin siRNA for 24h followed by treatment with or without 100μg/mL oxLDL
1458 for 15 mins at 37^0C. Flow cytometry for surface level of ABCG1.
1459

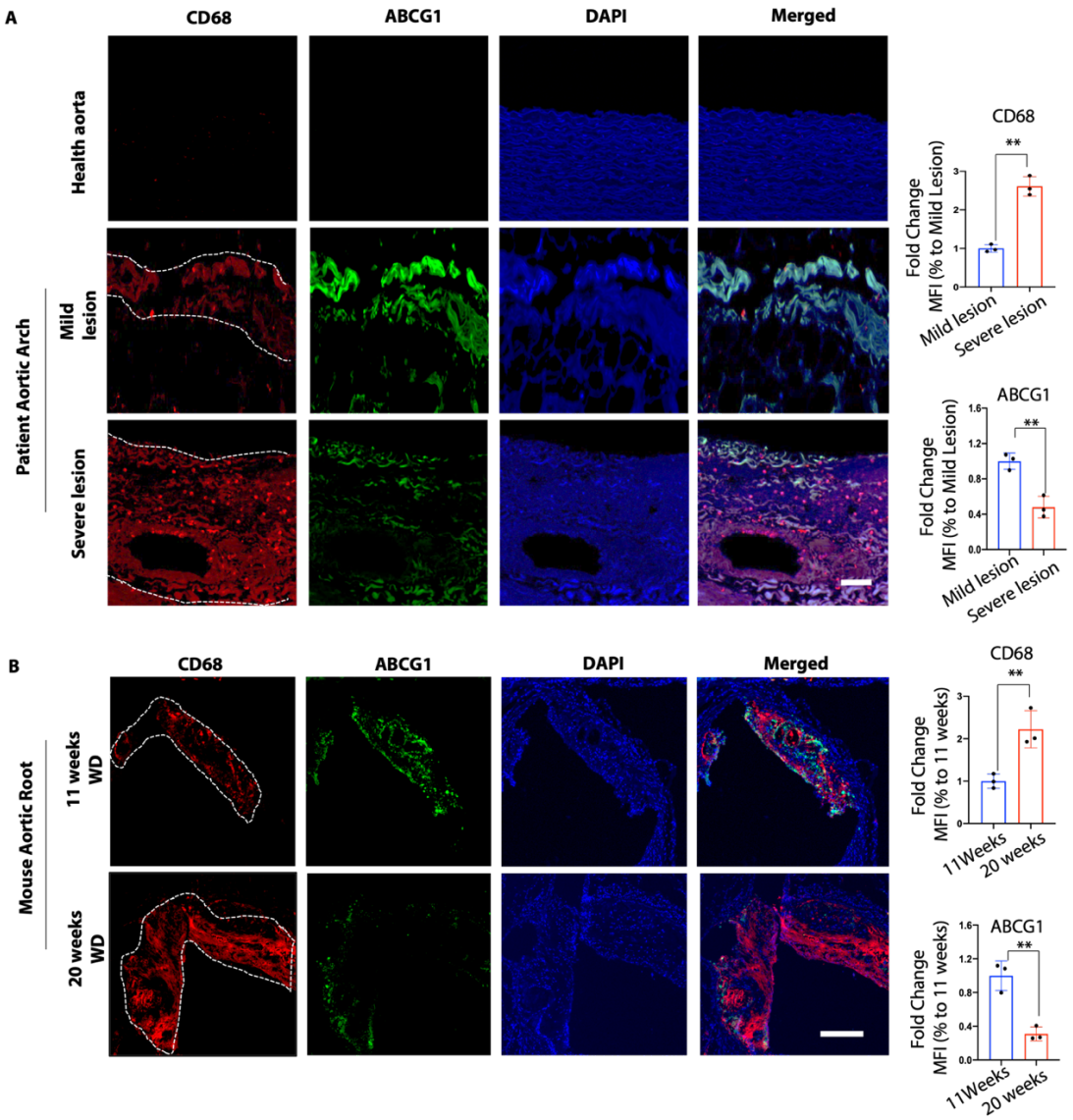

Figure S11

Figure S11. The expression of ABCG1 decreased with progression of atherosclerotic lesions in humans and mice. (**A-B**) Immunostaining of CD68 (red), ABCG1(green) and DAPI (blue) of human patient aortic arch sections (A, n=3) and mouse aortic root sections (B, n=3) in early and advanced stage of atherosclerosis （white dashed line outlined in CD68). Mean fluorescence intensity (MFI), **Mild vs Severe lesion, P<0.01, scale bar, A=50μm, B=200μm. Data are presented as mean ± SD and were analyzed using an unpaired Student's t-test.

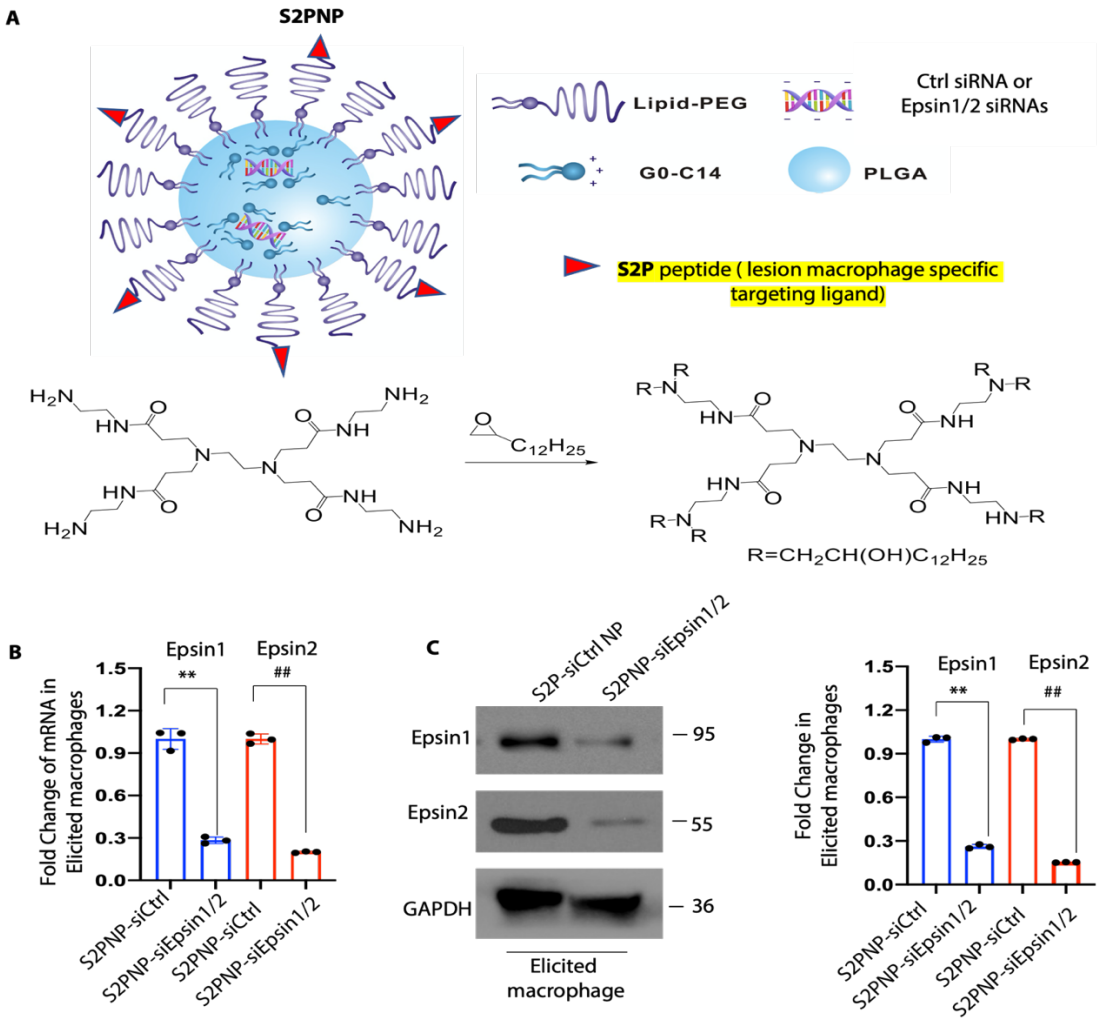

Figure S12. Characterization and silencing efficacy of S2P-conjugated siEpsin1/2 NPs. (**A**) Schematic of the targeted hybrid siRNA NP platform composed of a lipid-PEG shell with a lesion macrophage specific targeting ligand, S2P peptide, and a PLGA core. (**B-C**) Macrophages from WT mice were treated with S2PNP-siCtrl or S2PNP-siEpsin1/2 for 24h, RNA and proteins were isolated, qRT-PCR (B) and western blot (C) was performed to check the expression of Epsin 1 and 2 levels (n=3), **S2PNP-siCtrl vs S2PNP-siEpsin1/2 for Epsin1 expression, $P<0.01$; ##S2PNP-siCtrl vs S2PNP-siEpsin1/2 for Epsin2 expression, $P<0.01$. Data are presented as mean ± SD and analyzed using an unpaired Student's t-test.

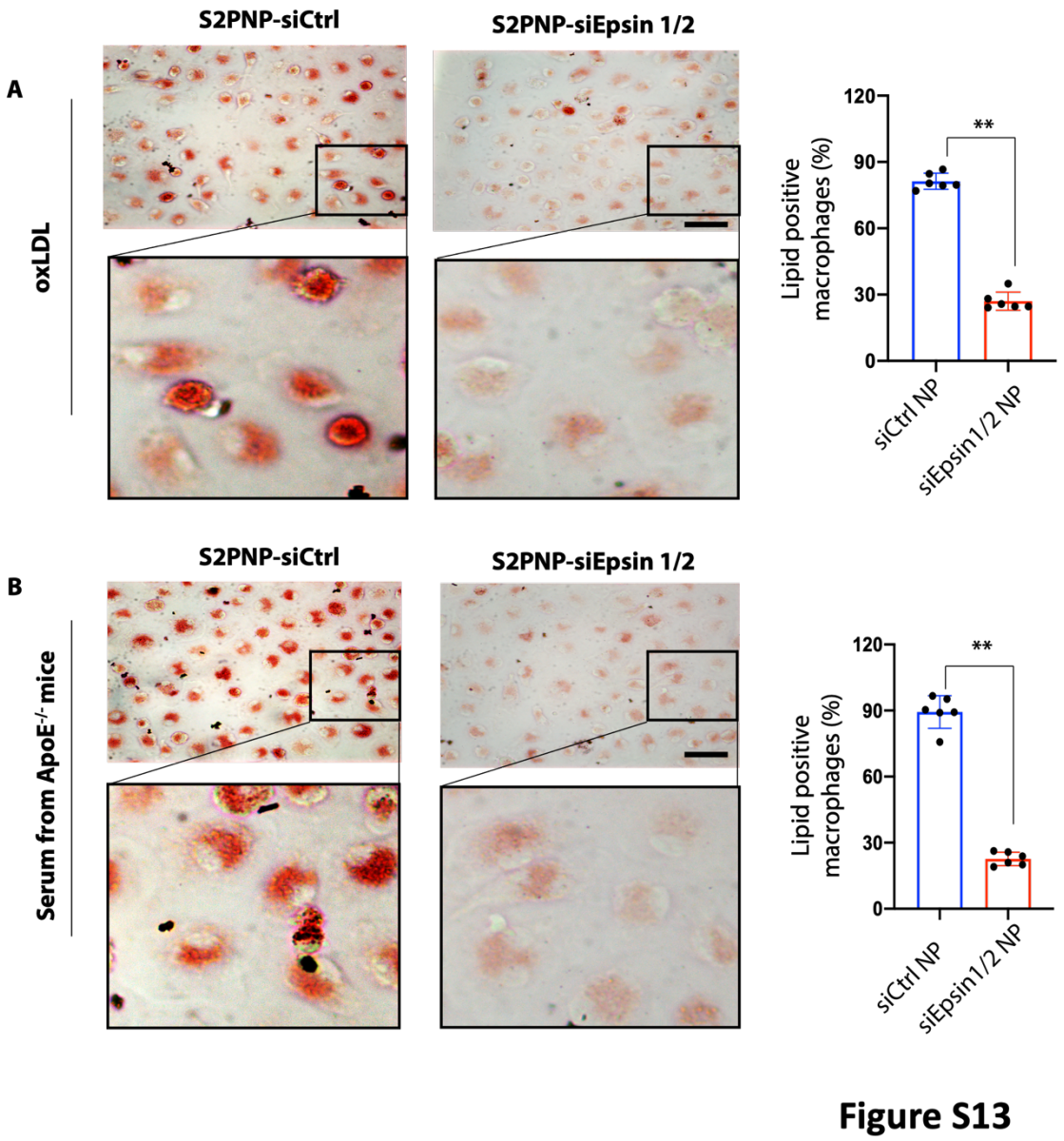

Figure S13. S2PNP-siEpsin1/2 treated macrophages show reduced foam cell formation. (**A-B**) Macrophages isolated from ApoE$^{-/-}$ mice were incubated in lipid-deficient medium and treated with S2PNP-siCtrl or S2PNP-siEpsin1/2 for 48h, follow with treatment of 100 μg/mL oxLDL (A) or serum (B) collected from ApoE$^{-/-}$ mice fed a WD for 8 weeks. ORO staining was performed (** S2PNP-siCtrl vs S2PNP-siEpsin1/2 group, n=6, P<0.01, scale bar=50μm). Data are presented as mean ± SD and analyzed using an unpaired Student's t-test.

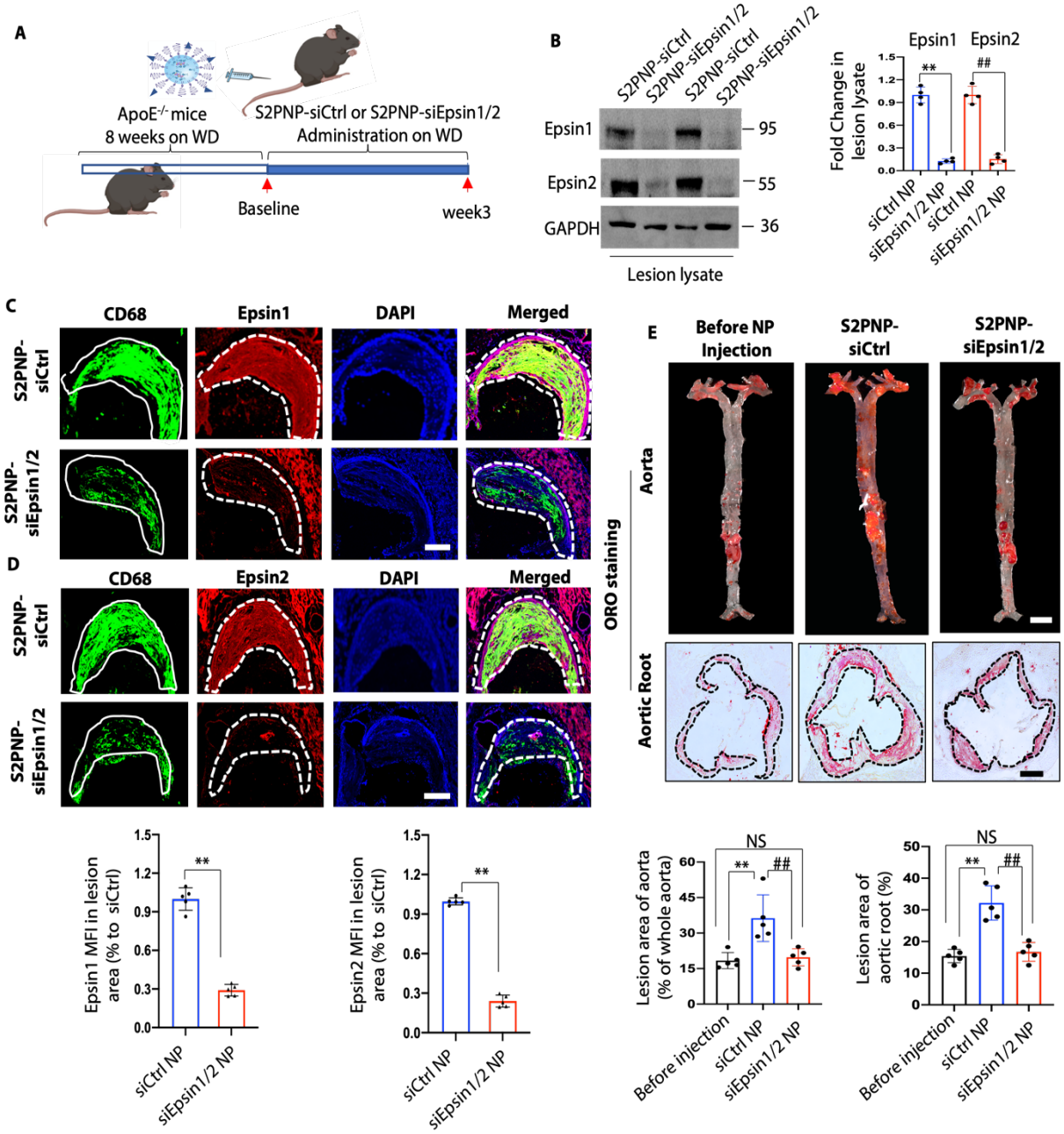

Figure S14

1483

1484

1485 **Figure S14. S2PNP-siEpsin1/2 inhibits lesion formation and macrophage accumulation in**
1486 **early stage of atherosclerosis.** (**A**) ApoE$^{-/-}$ mice were fed a WD for 8 weeks followed by treatment
1487 with S2PNP-siCtrl or S2PNP-siEpsin1/2 for 3 weeks (2 doses per week). (**B**) WB of Epsin 1 and
1488 2 after treatment with S2PNP-siCtrl or S2PNP-siEpsin1/2 NPs using lesional lysates from the
1489 aortas (n=4 times, **S2PNP-siCtrl vs S2PNP-siEpsin1/2 for Epsin1, P<0.01; ##S2PNP-siCtrl vs
1490 S2PNP-siEpsin1/2 for Epsin2, P<0.01). (**C-D**) Aortic roots from S2PNP-siCtrl treated ApoE$^{-/-}$ or
1491 S2PNP-siEpsin1/2 siRNA treated ApoE$^{-/-}$ mice were stained with the macrophage marker CD68
1492 (solid white line) and Epsin1 or Epsin2 (dashed white line), Epsin 1 and 2 mean fluorescence
1493 intensity (MFI) were analyzed (n=5, **S2PNP-siCtrl vs S2PNP-siEpsin1/2 for Epsin1, P<0.01,
1494 scale bars=500 μm). Data from B-D are presented as mean ± SD and analyzed using an unpaired
1495 Student's t-test. (**E**) *En face* ORO staining of aortas (upper panel) and aortic root sections (lower
1496 panel) of hearts from baseline, S2PNP-siCtrl or S2PNP-siEpsin1/2 treated ApoE$^{-/-}$ mice fed a WD.
1497 Lesion area was analyzed using one-way ANOVA (n=5, **S2PNP-siCtrl vs baseline, P<0.01,
1498 ##S2PNP-siCtrl vs S2PNP-siEpsin1/2 group P<0.01, Scale bar; aorta=5mm, aortic root=500μm).
1499 Data from E are presented as mean ± SD and were analyzed using one-way ANOVA.

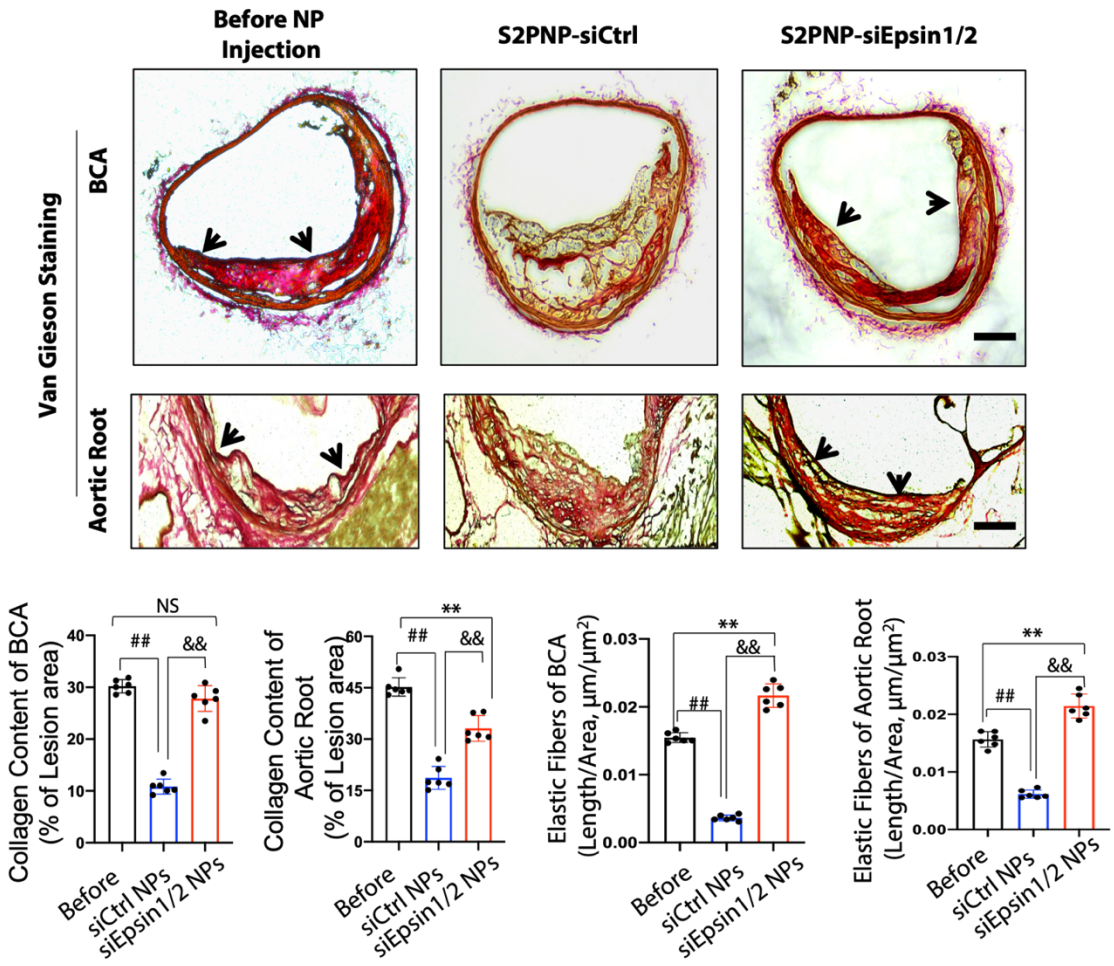

Figure S15

Figure S15. Silencing lesional macrophage Epsin1/2 by S2PNP-siEpsin1/2 NP-treatment stabilized plaques in a progression model of atherosclerosis. ApoE$^{-/-}$ mice fed a WD for 17 weeks followed by treatment with S2PNP-siCtrl or S2PNP-siEpsin1/2 for 3 weeks (two doses per week). Van Gieson's staining of brachiocephalic artery (BCA) (upper panel) and aortic root (lower panel) sections from baseline, S2PNP-siCtrl-, or S2PNP-siEpsin1/2-treated ApoE$^{-/-}$ mice was performed (arrows indicate the elastic fibers, n=6, **baseline vs S2PNP-siEpsin1/2 group, P<0.01; ##baseline vs S2PNP-siCtrl group, P<0.01; &&S2PNP-siCtrl vs S2PNP-siEpsin1/2 group, P<0.01, scale bar=250 μm). Data are presented as mean ± SD and were analyzed using one-way ANOVA.

1509

1510

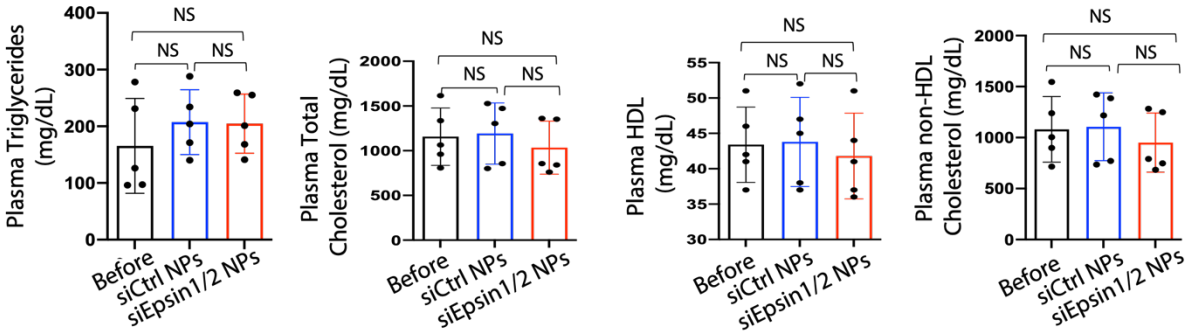

Figure S16

1511

1512 **Figure S16. Delivery of S2PNP-siEpsin1/2 does not change cholesterol and triglyceride levels**

1513 **of ApoE$^{-/-}$ mice fed a WD.** Plasma from ApoE$^{-/-}$ mice fed a WD for 17 weeks (before NP injection),

1514 followed by an additional 3 weeks of treatment with S2PNP-siCtrl or S2PNP-siEspsin1/2, showed

1515 no alteration in triglyceride, cholesterol, HDL and non-HDL (LDL/VLDL) cholesterol levels (n=5;

1516 NS, no significant difference). Data are presented as mean ± SD and were analyzed using a one-

1517 way ANOVA.

1518

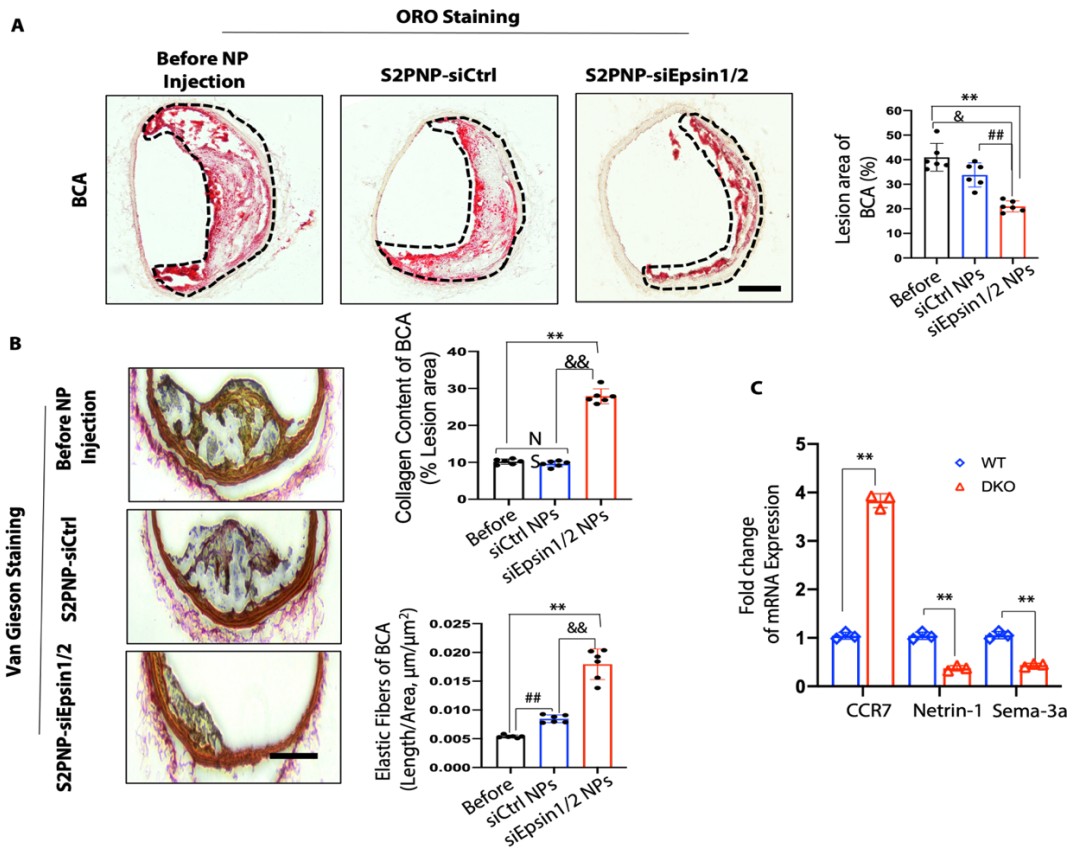

Figure S17

Figure S17. Silencing macrophage Epsin1/2 by S2PNP-siEpsin1/2 NPs reduces lesion size in a regression model of atherosclerosis. (**A**) ORO staining of BCA sections in baseline, S2PNP-siCtrl or S2PNP-siEpsin1/2 treated PCSK9-mice was performed and lesions were indicated (dash lines) (n=6, **Baseline vs S2PNP-siEpsin1/2 group, P<0.01; &Baseline vs S2PNP-siCtrl group, P<0.05; ##S2PNP-siEpsin1/2 vs S2PNP-siCtrl group, P<0.01; scale bar=500μm). (**B**) Van Gieson's staining of BCA sections from above three groups was performed (n=6, **Baseline vs S2PNP-siEpsin1/2 group, P<0.01; ##Baseline vs S2PNP-siCtrl group, P<0.01; &&S2PNP-siEpsin1/2 vs S2PNP-siCtrl, P<0.01; scale bar=500μm). Data in A and B are presented as mean ± SD and analyzed using one-way ANOVA. (**C**) qRT-PCR analysis to confirm expression of the indicated genes (n=3, **DKO vs WT group, P<0.01). Data are presented as mean ± SD and analyzed using an unpaired Student's t-test.

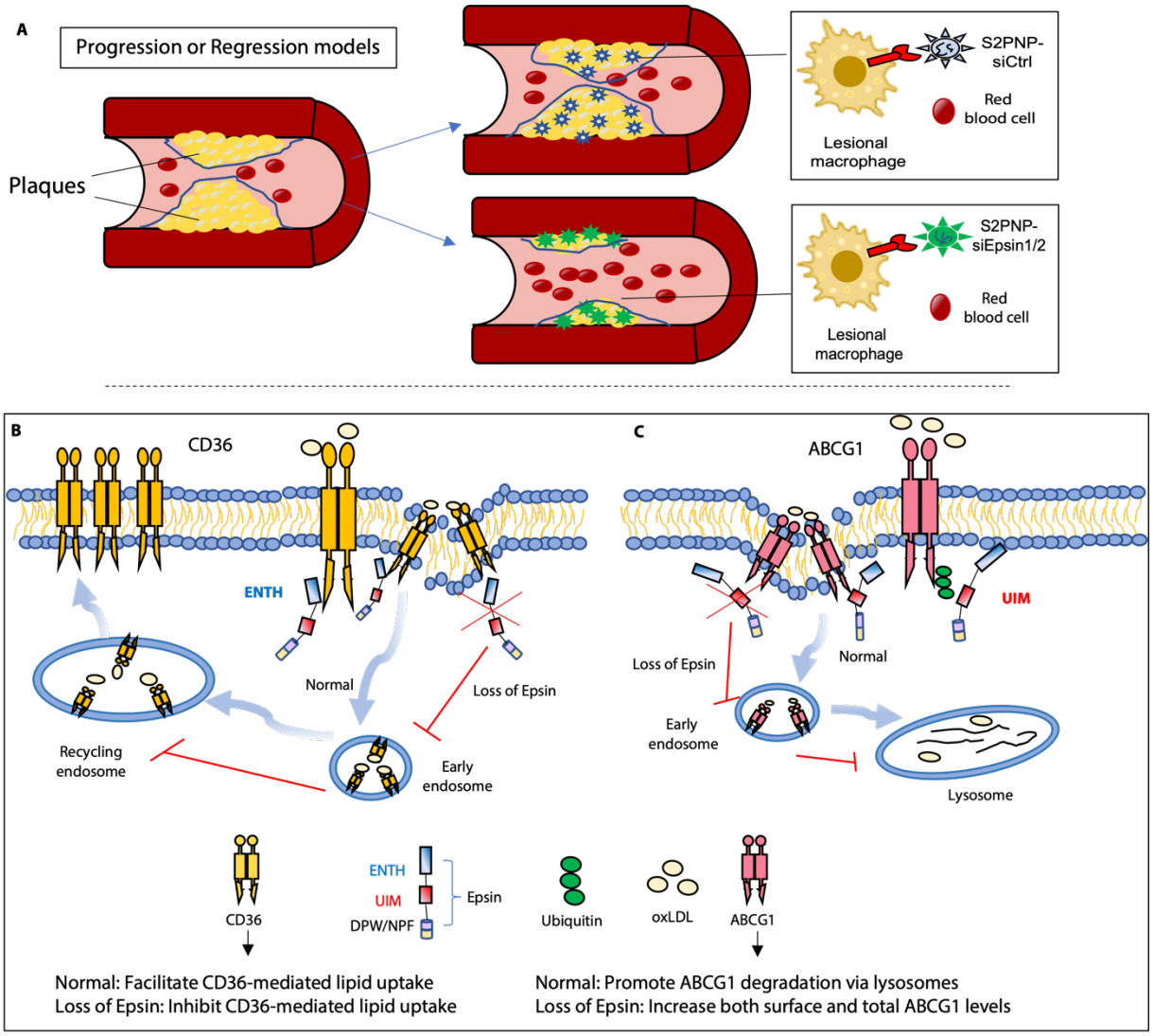

Figure S18

Figure S18. Summary schematic diagram of the study. (**A**) In the progression model of atherosclerosis, the plaque size and lesions increase in the artery on western diet feeding. The delivery of S2PNP-siEpsin1/2 significantly slowed the progression of atherosclerosis compared to S2PNP-siCtrl group. In the regression model of atherosclerosis, plaque size and lesion area were dramatically reduced with the intravenously injection of S2PNP-siEpsin1/2. (**B-C**). Under the stimuli of oxLDL, Epsin binds to CD36 and ABCG1 through Epsin ENTH and Epsin UIM domains, respectively. In B, Epsin facilitates CD36-mideated lipid uptake via recycling

1539 endosomes. The loss of Epsin impairs the internalization of CD36, which results in reduced lipid
1540 uptake. While in C, Epsin promotes endocytic degradation of ABCG1via lysosomes, which leads
1541 to reduced total and surface level of ABCG1.
1542

1543 **Table S1. List of reagents and animal models**

REAGENT or RESOURCE	SOURCE	Note
Primary Antibodies		
Rabbit polyclonal anti-Epsin1	Home made	N/A
Rabbit polyclonal anti-Epsin2	Abcam	Cat# ab74942
Rabbit polyclonal anti-Epsin2	Home made	N/A
Rat monoclonal Anti-mouse /SR-B3CD36	R & D System	Cat# MAB2519,
Rabbit monoclonal anti-CD36	Invitrogen	Cat# VL3153825
Mouse monoclonal anti-GAPDH	Santa Cruz Biotechnology	Cat# F118, sc166545
Mouse monoclonal anti-ubiquitin	Cytoskeleton, Inc	Cat# AUB01
Rabbit polyclonal anti-ABCA1	Novus Biologicals	NB400-105SS
Rabbit polyclonal anti-ABCG1	Novus Biologicals	NB400-132B,
Rabbit monoclonal anti-ABCG1	Invitrogen	Cat# VK3126422
Goat polyclonal anti mouse LDLR	R & D System	Cat# AF2255
Rat monoclonal Anti-mouse SRA1	R & D System	Cat# MAB1797
Monoclonal anti-Flag	Sigma-Aldrich	Cat# F3165
Rat monoclonal anti-F4/80	Santa Cruz Biotechnology	Cat# sc59171
F4/80 monoclonal antibody, APC	ThermoFisher Scientific	Cat# MF48005
Anti-mouse F4/80-Alexa Fluro 488	Invitrogen/eBioscience	Cat# 2126068
Goat polyclonal anti-EEA1	Santa Cruz Biotechnology	Cat# B1813, sc6415
Mouse monoclonal anti-Rab11	Santa Cruz Biotechnology	Cat# H0919, sc166912
Mouse monoclonal anti-Lamp1	Santa Cruz Biotechnology	Cat#F1609, sc18821
Rabbit polyclonal anti-CD68	Santa Cruz Biotechnology	Cat# sc9139
Anti-Actin, α-Smooth Muscle - Cy3™ antibody, Mouse monoclonal α-SMA	Sigma-Aldrich	Cat# C6198

Rat-anti Mouse CD31	BD Pharmingen	Cat# 550274
Goat monoclonal P-selectin	Santa Cruz Biotechnology	Cat# G1411, sc6943
Mouse monoclonal E-selectin	Santa Cruz Biotechnology	Cat# sc137054
Goat polyclonal ICAM-1	Santa Cruz Biotechnology	Cat# sc1511
Mouse monoclonal VCAM-1	Santa Cruz Biotechnology	Cat# sc13160
Alexa Fluor Conjugated Second Antibodies		
Goat anti-rabbit 647	Invitrogen	Cat# A-21244
Goat anti-rat 647	Invitrogen	Cat# A-21247
Donkey anti-mouse 594	Invitrogen	Cat# A-21203
Donkey anti-rabbit 594	Invitrogen	Cat# A-21207
Donkey anti-rat 594	Invitrogen	Cat# A-21209
Donkey anti-rat 488	Invitrogen	Cat# A-21208
Donkey anti-mouse 488	Invitrogen	Cat# A-21202
Donkey anti-rabbit 488	Invitrogen	Cat# A-21206
Biological Samples		
Atherosclerosis patient's arch samples	Maine Medical Center (MRC)BioBank, Maine	N/A
Normal population's arch samples	Maine Medical Center (MRC)BioBank, Maine	N/A
Mouse aortic roots and hearts	This study	N/A
Mouse serum	This study	N/A
Reagents, Peptides, and Recombinant Proteins		
Oil Red O (ORO)	AMRESCO	Cat# 0684-100G
Hematoxylin and Eosin stain kit	Vector Laboratories	Cat# H-3502
Oxidized LDL (ox-LDL)	Athens Research and Technology	Cat#12-16-120412-ox
Acetylated LDL (Ac-LDL)	Invitrogen	Cat#2300941

Low Density Lipoprotein from Human Plasma, oxidized, DiI conjugate (DiI-OxLDL)	ThermoFisher Scientific	Cat# L34358
TopFluor Cholesterol	Avanti Polar Lipids,Inc	Cat# 810255p
MG132	Sigma-Aldrich	Cat# M7449
N-Ethylmaleimide (NEM)	Alfa Aesar	Cat# 40526
Brewer Thioglycollate Medium	Sigma-Aldrich	Cat#124k0115
Bodipy 493/503	Invitrogen	Cat# D3922
SlowFade mount with DAPI	Invitrogen	Cat# 1896320
M-CSF mouse	Prospec	Cat# cyt-439-b
Protein inhibitor cocktail	TargetMol	Cat# C0001
Phalloidin-iFluor 594 reagent	Abcam	Cat# ab176751
Liver x receptor agonist (LXR T0901317)	Apexbio Tech LLC	Cat#A2249
Mouse seroblock FCR	Bio-Rad	Cat# BuF041B
Phosphotungstic acid hydrate	ACROS	Cat#A0417659
[1,2-^{3}H]-Cholesterol	PerkinElmer	Cat# NET139001MC
Liquid scintillation fluid OPTI-Flour	PerkinElmer	Cat# 47-20081
Apoprotein A-I (ApoA1)	Sigma-Aldrich	Cat# A0722
High density lipoprotein (HDL)	Sigma-Aldrich	Cat# L8039
Hexane	ThermoFisher Scientific	Cat# 610070040
Isopropanol, molecular biology grade	ThermoFisher Scientific	Cat# T036181000CS
Cholesterol acyltransferase (ACAT) inhibitor	Sigma-Aldrich	Cat# S9318-5mg
Lipofectamine 2000 transfection reagent	Invitrogen	Cat#11668027
Lipofectamine LTX	Invitrogen	Cat# A12621
ImageiT™ signal enhancer	Invitrogen	Cat# 136933
Qiagen RNeasy Mini Kit	Qiagen	Cat# 74106
RNase-free DNAse 1	New England Biolabs	Cat# M0303S
SuperScript III First-	ThermoFisher Scientific	Cat# 18080400

Strand Synthesis SuperMix		
SYPR Green PCR Master Mix reagent	GeneCopoeia	Cat# QP001-01
Aqueous Mounting Medium	R & D Systems	Cat# CTS011
Protein A/G plus agarose	Santa Cruz Biotechnology	Cat# Sc-2003
EZ-Link Sulfo-NHS-LC-Biotin	ThermoFisher Scientific	Cat# 21335
Neutravidin Beads	ThermoFisher Scientific	Cat# 29200
S2P-peptide (CRTLTVRKC)	GLS Biochem Systems Inc	Cat# 625358
DSPE-PEG-Mal (MW, 3.4 kDa)	Nanocs Inc.	Cat# PG2-DSML-3k
Cationic ethylenediamine core-poly(amidoamine) (PAMAM) dendrimer generation 0 (G0)	Sigma-Aldrich	Cat# 412368
Ester-terminated PLGA	DURECT Corporation	Cat# B6013-2
Amaxa™ Mouse macrophage nucleofector kit	Lonza	Cat# VPA-1009
Collagenase type I	Gibco by Life technologies	Cat# 1866783
Collagenase type IV	Gibco by Life technologies	Cat# 2383671
Liberase	Roche	Cat# 05401127001
Chromium Next GEM Single Cell 3' Reagent Kits v3.1	10X Genomics	
GEM Single Cell 3'GEM Kit v3.1	10X Genomics	PN-1000123
GEM Single Cell 3'Library Kit v3.1	10X Genomics	PN-1000157
GEM Single Cell 3'Gel Bead Kit v3.1	10X Genomics	PN-1000122
Dynabeads™ MyOne™ SILANE	10X Genomics	PN-2000048
GEM Chip G Single Cell Kit, 48rxns	10X Genomics	PN-1000120
Single Index Kit T Set A, 96 rxns	10X Genomics	PN-1000213
SPRIselect Reagent	Beckman Coulter Inc.	Cat# B23317
Recombinant DNA		
pcDNA	Kai Song et al, 2021	N/A

Flag-Epsin1^{WT}	Yunzhou Dong et al, 2020	N/A
Flag-Epsin1$^{\Delta UIM}$	Yunzhou Dong et al, 2020	N/A
Flag-Epsin1$^{\Delta ENTH}$	Yunzhou Dong et al, 2021	N/A
CD36-bio-His: CMV plasmid	Addgene	Cat# 52025
ABCG1-pCSdest: SP6 plasmid	Addgene	Cat# 53952
Commercial Assays		
BAC-protein concentration measurement kit	Thermo Fisher Scientific	Cat# 23225
SuperSignal™ West Pico Chemiluminescent Substrate	Thermo Fisher Scientific	Cat#: 34080
Experimental Models: Organisms/Strains		
ApoE$^{-/-}$ atherosclerosis mouse model	Jackson Laboratory	Cat# 008525
Epsin mutant mouse model	This study	N/A
LysM-Cre deleter mice	This study	Cat# 004781
ABCG1^{fl} mouse model	This study	Cat# 027954
Experimental Models: Cell Lines		
HEK-293T	ATCC	CRL-3216
Virus Strain		
rAAV8-D377Y-mPCSK9	Boston Children's Hospital Viral Core Facility	N/A
Deposited Data		
N/A		
Oligonucleotides		
Epsin1:	This study	N/A
Forward: 5'-CTACCAACGTCCATTGCGGT-3' Reverse: 5'-GCAGCGATGAGGTCGACATT-3'		
Epsin2:	This study	N/A

Forward: 5'-TCTATCAGACGGCAGATGAAAAAC-3' Reverse: 5'-GTCATTGGAGGTGGCCTCC-3'		
IL-6	This study	N/A
Forward: 5'-AGTCCGGAGAGGAGACTTCA-3' Reverse: 5'-TTCCACGATTTCCCAGAG-3'		
IL-1beta	This study	N/A
Forward: 5'-GAAGAAGAGCCCATCCTCTG-3' Reverse: 5'-TCATCTCGGAGCCTGTAGTG-3'		
TNF-alpha	This study	N/A
Forward: 5'-ATGAGAAGTTCCCAAATGGC-3' Reverse: 5'-CTCCACTTGGTGGTTTGCTA-3'		
MCP-1	This study	N/A
Forward: 5'-GAAGGAATGGGTCCAGACAT-3' Reverse: 5'-ACGGGTCAACTTCACATTCA-3'		
iNOS	This study	N/A
Forward: 5'-CCCTTCCGAAGTTTCTGGCAGC-3' Reverse: 5'-GGCTGTCAGAGCCTCGTGGCTTTGG-3'		
IL-10	This study	N/A
Forward: 5'-CCCAGAAATCAAGGAGCATT-3' Reverse:5'-TCACTCTTCACCTGCTCCAC-3'		
Arg1	This study	N/A
Forward: 5'-CAGTGGCTTTAACCTTGGCT-3' Reverse: 5'-GTCAGTCCCTGGCTTATGGT-3'		
ABCG1	This study	N/A
Forward: 5'-CCGATGTCCCCTTTCAGATCA-3' Reverse: 5'-AGCAGCGAACAGCACAAAAC-3'		
ABCA1	This study	N/A
Forward: 5'-GTGGGCTCCTCCCTGTTTTT-3' Reverse: 5'-TCTGAGAAACACTGTCCTCCTTTT-3'		
CD36	This study	N/A
Forward: 5'-GCTGTCAGGCGTCAGGATAA-3' Reverse: 5'-CACATTTCAGAAGGCAGCAACT-3'		

CCR7	This study	N/A
Forward: 5'- CATGGACCCAGGTGTGCTT-3' Reverse: 5'- CATGAGAGGCAGGAACCAGG-3'		
Netrin-1	This study	N/A
Forward: 5- GGAGGAACCGGAAGACTGTG-3' Reverse: 5- GTCCTCGGCATTACCCAACA-3'		
Sema 3a	This study	N/A
Forward: 5'- ACGCACCATGGCACCG-3' Reverse: 5'- GTGCTAGGCCAGTATATCTCTCTG-3'		
Beta-actin	This study	N/A
Forward: 5'- TTACTGCTCTGGCTCCTAGCA-3' Reverse: 5'-CCACCGATCCACACAGAGTAC-3'		
Mouse Epsin1 siRNA sequence	This study	N/A
GAACUGGAGGCACGUCUACAAUU		
Mouse Epsin2 siRNA sequence	This study	N/A
GCAGUGCCGUGAGAACAUCUUUU		
Mouse control luciferase siRNA sequence	This study	N/A
CUUACGCUGAGUACUUCGA dT dT		
Mouse clathrin (Picalm) siRNA sequence	ambion	Cat#AM16708
GGAGAUAUUCCAGAUCUUUtt		
Software and Algorithms		
Image J	NIH website: https://imagej.nih.gov/ ij/	N/A
GraphPad Prism	GraphPad software company: https://www.graphpad. com/sci entific- software/prism/	N/A

BioRender	BioRender http://app.biorender.com	N/A
Zeiss Zen lite	https://www.zeiss.com/microscopy/us/products/microscope-software/zen-lite.html	N/A

1544